Plasmonic Properties of Metallic Nanoparticles : Beyond the Dipolar Resonance

Artur Movsesyan

Thèse
de doctorat
de l'UTT

Artur MOVSESYAN

Plasmonic Properties of Metallic Nanoparticles: Beyond the Dipolar Resonance

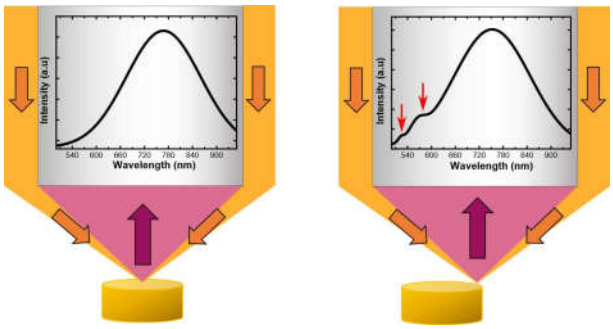

Champ disciplinaire :
Sciences pour l'Ingénieur

2018TROY0051 **Année 2018**

utt
UNIVERSITÉ DE TECHNOLOGIE
TROYES

THESE

pour l'obtention du grade de

DOCTEUR
de l'UNIVERSITE DE TECHNOLOGIE DE TROYES

EN SCIENCES POUR L'INGENIEUR

Spécialité : MATERIAUX, MECANIQUE, OPTIQUE, NANOTECHNOLOGIE

présentée et soutenue par

Artur MOVSESYAN

le 14 décembre 2018

Plasmonic Properties of Metallic Nanoparticles: Beyond the Dipolar Resonance

JURY

Mme F. DE FORNEL	DIRECTRICE DE RECHERCHE - CNRS	Présidente
M. E. COTTANCIN	PROFESSEUR DES UNIVERSITES	Rapporteur
M. G. LÉVÊQUE	MAITRE DE CONFERENCES - HDR	Rapporteur
M. M. FINAZZI	PROFESSORE ORDINARIO	Examinateur
M. P.-M. ADAM	PROFESSEUR DES UNIVERSITES	Directeur de thèse
Mme A.-L. BAUDRION - BEAL	MAITRE DE CONFERENCES	Directrice de thèse

Contents

Acknowledgment

At the end of the trajectory of my PhD study I would like to thank all people who supported and help me during these three years.

First of all, I wish to express my sincere gratitude to my supervisors. To Anne-Laure BAUDRION, I am thankful for your continuous guidance, support and endless help in administrative questions ("you are still the guarantee of my flat"). Your solid knowledge in Microscopy and its instrumentation helps me a lot to gain valuable skills for performing the experiments. Moreover, I would like to thank for checking and correcting my messy-mind manuscripts. To Pierre-Michel ADAM, I appreciate boundless our discussions starting from the deep understanding of plasmonic modes and finishing the discussions about “The Game of Thrones” or Armenian-born famous people like Kardashian or Aznavour. To both supervisors, Thanks for discussion of my ideas, support of my initiatives, proofreading of the presentations, manuscripts and this thesis. I also grateful for working on and polishing the sharp corners of my hard character. Hopefully, I will use properly your pieces of advice for future. I am happy for these years that we spent in a friendly atmosphere. If it would be the second opportunity to do PhD, doubtless I would choose you again as supervisors.

I acknowledge to my supervisor during the master studies Alexandre BOUHELIER, who believed in me and helped to be here where I am now.

I would like to express my gratitude to Renaud BACHELOT for helping me to participate in Conferences and paying for a publication.

I thank my thesis jury members Prof. Emmanuel COTTANCIN, Prof. Gaëtan LÉVÊQUE, Prof. Frédérique DE FORNEL, and Prof. Marco FINNAZI for their time and intellectual contribution.

I would also like to thank all my colleagues and members of L2N for welcoming me in this friendly family, who collaborated with me and gave me advice during the time of my PhD. Big thanks to our lab engineers Sergei KOSTCHEEV, Jérémie BÉAL and Régis DETURCHE for their help and training sessions. I also thank my Lebanese colleague-friends Lina and Nancy for good and funny moments. I also grateful to my friend and officemate David for the help during the first year of my PhD. Particularly,

I am deeply thankful to my officemates and friends Gwenaëlle and Aurelie. I cannot forget how they helped when my foot was broken at the end of my PhD. Furthermore, they are my secret teachers of French. I am grateful to my friends Nacef and Gustavo, for being with me during good and not so much good days. I would like to thank my friend and football teammate Youssef who help me during the time of my broken foot.

I am thankful to Monika Fleischer and Dai Zhang for very friendly and warm welcome in the Tübingen university during my short-term scientific mission. I am grateful to the members of the groups of Monika and Dai very much for the introducing the lab and further help.

I express my gratitude to Emmanuel COTTANCIN for providing an opportunity to do experiments in the laboratory of ILM (Institut Lumière Matière).

I am thankful to all my friends, whom I do not mention here. Finally, I am grateful to my soulmate and fiancée Alina, who is supporting, motivating me every day. Surely, I am grateful to my mam, dad and sister for supporting and helping me how long I remember me.

General Introduction

In this digital age, a rapid transport and high capacities of information ask for high miniaturization and large scale integration of functional devices. Nowadays electronic devices have reached their critical dimensions of 10 nm (coming soon from Intel Corporation), because they are approaching their fundamental speed and bandwidth limit in everyday increasing consumer demand [1, 2]. Instead of electrons a promising solution is the usage of light as a information carrier, since photonic components can be much faster than their electronic analogs. For instance, optical fibers are commonly used for transmitting information with very high speed and bandwidth, with reported 255 Tbps [3]. Nevertheless, there are difficulties to scale down the technology due to the diffraction barrier limiting the dimensions (Abbe limit) to half of the effective wavelength [4–6]. However, the information can be transferred at the speed of light, though the dimensions of the integrated components of photonic devices are still larger compared to electronic devices. The Fig. 1 shows a graph of operating speed of devices versus their critical dimensions for different technologies. Hence, a compromise solution between high transfer speed by photonics components and size of electronic devices could be found in so-called plasmonics.

Plasmonics is the area at the intersection of science and technology in which the interaction of light with matter (metals, metal-like materials) is mediated by surface electromagnetic excitations at a dielectric-metal interface [8]. The term plasmonics was coined by H. A. Atwatter in 2001 [9]. Besides the promising use of plasmonics in the information technology it is practicing successfully in other applications such as renewable energy, sensing and etc. [10–16]. Plasmonic structures are the key point of the enormous number of applications based on their optical properties. Various optical characterization techniques have been developed in order to determines plasmon resonances. However, to get the same results with the same optical characterization done by other researchers remains a challenge. For example Fig. 2 shows the comparison of the resonances position of identical gold nanocylinders published by different researchers. We compare the peak positions of the 20 nm height nanocylinders. The Fig. 2a shows LSPR peak position for the diameters 38.5 nm at 2.27eV (546 nm), 51

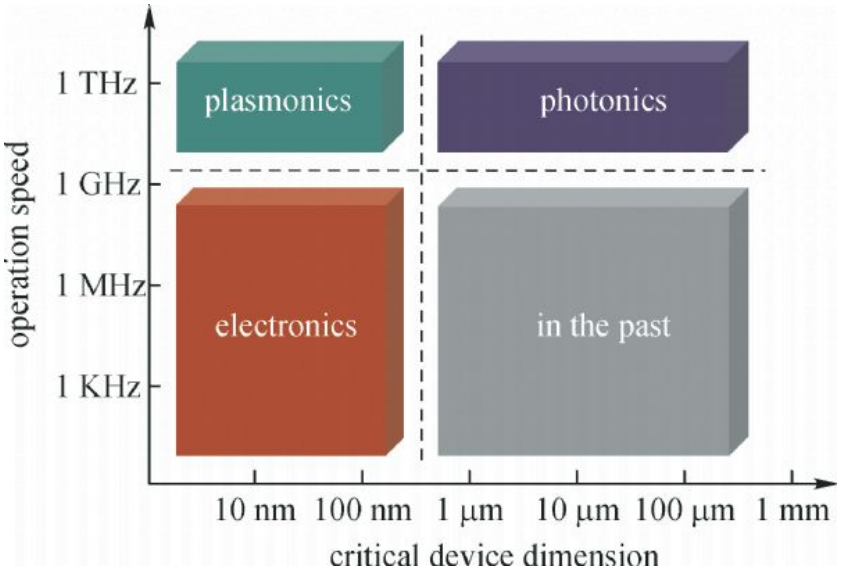

FIGURE 1: Typical operation speed and critical device dimensions of different chip-scale device technologies [7]

nm at 2.15eV (576 nm), 77 nm at 2eV (620 nm), 140 nm at 1.63eV (760 nm) and for 193 nm at 1.4eV (885 nm), while the peak positions on the Fig. 2b for the same diameters are respectively at 578 nm, 585 nm, 633 nm, 735 nm and 811 nm (table is below). The essential question is “Why" is there a peak position shift?

TABLE 1: LSPR peak positions in different articles

Diameter (nm)	38.5	51	77	140	193	Paper
Peak position (nm)	546	576	620	760	885	[17]
	578	585	633	735	811	[18]

The main idea of this thesis work is to scope the fundamental optical properties of plasmonic nano-objects. We take the lead to explain possible differences of the plasmonic resonances due to different factors and answer the question “Why". The manuscript is separated in two main parts: (i) is the study of the changes of plasmonic resonances caused by instrumentation (like experimental setup and its compounds); (ii) the variations of optical properties of plasmonic nanoparticles based on the plasmonic system changes themselves. The experimental data are supported by simulations and by their complete analysis.

The First chapter gives a brief introduction of the plasmon resonances and their use for applications. The second chapter discusses the plasmonic resonances that a gold nanocylinder may sustain. Moreover, we compare the plasmonic resonances of nanoparticles presenting different shapes. The Third chapter introduces and discusses the main factors inducing a change in the recorded experimental optical spectra because of the optical setup specifications. Furthermore, we demonstrate a method to

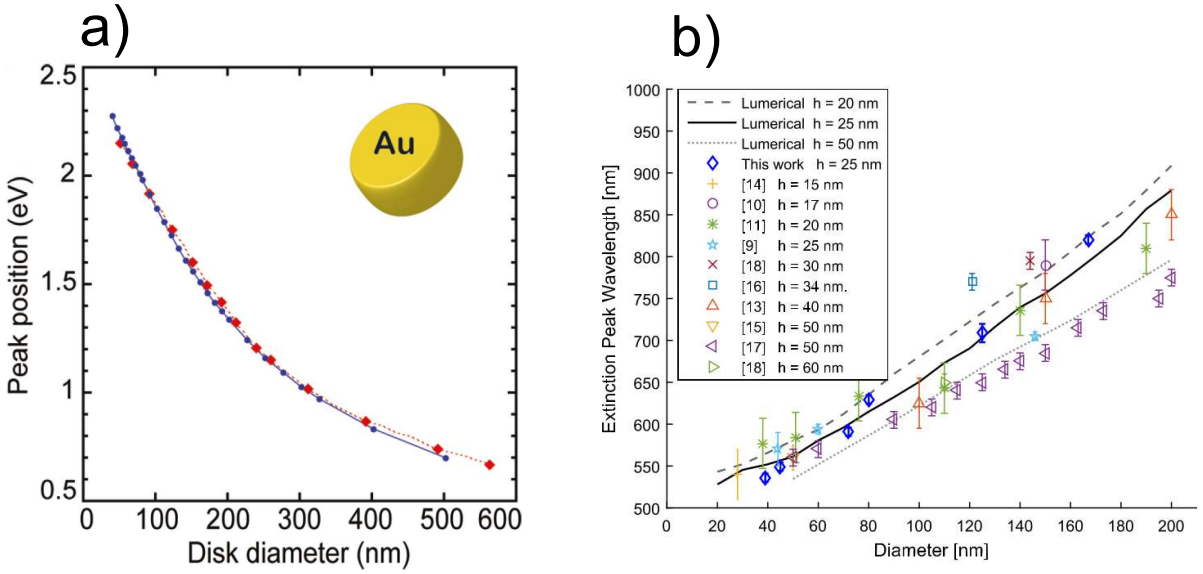

FIGURE 2: (a) Extinction spectra peak positions of gold nanocylinders depending on the diameter. The gold nanocylinders height is 20 nm and the substrate is glass [17].(b) The extinction spectra peak positions of gold nanocylinders deposited on a glass depending on the diameter for different heights [18]. The lines show numerically simulated data. h is the height.

characterize a single metallic nanoparticle using an ensemble of nanoparticles. The Fourth chapter shows that multi-resonant properties of a single nano-object can be retrieved depending on the experimental setup configuration. The fifth chapter is dedicated to the hybridization between different plasmonic modes of the same nanostructure. The radiation pattern of different plasmonic modes are explained. Finally, we propose an application based on our study and some perspectives are given.

1 Introduction to plasmons

The interaction of an external electromagnetic (EM) wave and the conduction band electrons at a metal interface may result in plasmons [8, 19, 20]. It is defined commonly as a quantum of plasma oscillations [21], whose theory was proposed by Pines and Bohm in 1952 [22]. Plasmons often refer to plasmon polaritons which is the coupled state between plasmon and photon. Wood in 1902 published firstly an experimental observation anomalies caused by surface plasmon polaritons [23]. He noticed dark stripes in the spectrum of the diffracted light, when a metallic diffraction grating was illuminated by a polychromatic light. The dark stripes represent the losses of the light in the grating at certain wavelengths, which were not transmitted. This phenomenon is known as Wood-Raleigh anomalies. In 1957 Ritchie predicted that the electron energy losses should describe the collective modes (surface plasmons) of metal thin films [24]. Then, in 1959 Powel and Swan verified experimentally the concept proposed by Ritchie [25, 26].

1.1 Optical properties of metals

The optical properties of metals depend strongly on the frequency of EM wave. The metals are highly reflective for frequencies up to visible and EM cannot propagate through. In Fig. 1.1 is shown the chart of the light frequency versus the wavelength.

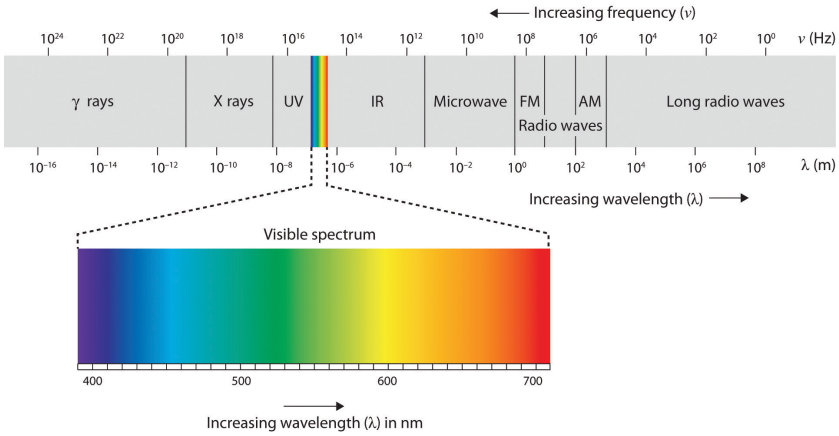

FIGURE 1.1: Light wavelength versus frequency chart [**?**].

At high frequencies (UV-γray) the majority of metals demonstrate dielectric-like character allowing EM field to penetrate through. It depends on their electronic band structure, for example alkali metals (Li, Na, K, Rb, Cs, Fr) are transparent in UV. Though, the noble metals (Au, Ag, Cu) have strong absorption in UV caused by inter-band transitions. These are described by the complex dielectric function called dielectric permittivity - $\epsilon(\omega)$. In other words, $\epsilon(\omega)$ draws the dispersive properties of metals. $\epsilon(\omega)$ is governed by the conduction band electrons and inter-band transitions. The conduction electrons are generally described by the Drude model. Following the Drude model's description, the conduction electrons form an electron gas and move freely through a metal. The illustration of the Drude model is shown in Fig. 1.2. The basic assumptions are that electron-electron and ion-interactions are neglected, and electrons move in straight line in the absence of electric field. Moreover, they achieve thermal equilibrium by collision with lattice. The collisions are interpreted by the kinetic theory. The mean free time (relaxation time) between collisions is τ and the probability of collisions is $1/\tau$.

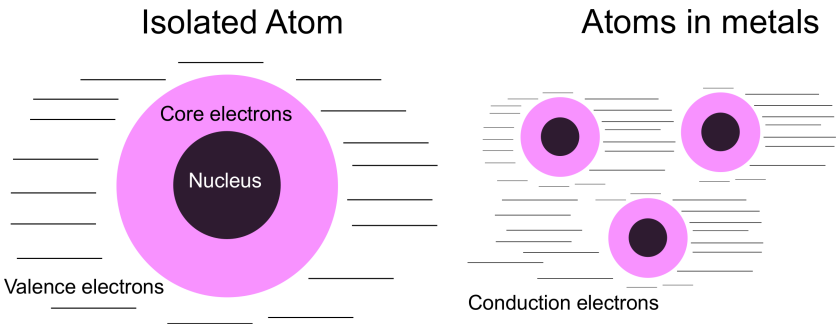

FIGURE 1.2: Drude model representation

When the electric field is applied the valence electrons are displaced by $\vec{r}$ and induce a macroscopic polarization ($\vec{P}$):

$$\vec{P} = -n \cdot e \cdot \vec{r}, \qquad n = \frac{N}{V}, \tag{1.1}$$

where, n is the electron density per unit volume (V), e is the electron charge, N is the number of electrons. Let's link the polarization and the dielectric function. We will start with macroscopic Maxwell's equations.

$$\begin{aligned}
div(\vec{D}) &= \rho_{ext}, && (\vec{D} - \text{Electric field displacement,} \\
& && \rho_{ext} - \text{External charge density}) \\
div(\vec{B}) &= 0, && (\vec{B} - \text{Magnetic field}) \\
r\vec{o}t(\vec{E}) &= -\frac{\partial \vec{\mathcal{B}}}{\partial t} && (\vec{E} - \text{Electric field}) \\
r\vec{o}t(\vec{H}) &= \frac{\partial \vec{D}}{\partial t} + \vec{J}_{ext} && (\vec{H} - \text{Magnetizing field,} \\
& && \vec{J}_{ext} - \text{External current density})
\end{aligned} \tag{1.2}$$

Indeed, the four macroscopic field are linked through the polarization and magnetization. As we are focused on non-magnetic materials the relation takes the following form:

$$\vec{D} = \epsilon_0 \vec{E} + \vec{P}, \tag{1.3}$$

where ϵ_0 is free space permittivity. For linear response of a metal to the electric field changes the polarization depends on electric field linearly.

$$\vec{P} = \epsilon_0 \chi \vec{E}, \tag{1.4}$$

where, χ is the electric susceptibility. It reveals how easily dielectric material polarizes. Importing the equation 1.4 in 1.3 and denote $1 + \chi$ as ϵ_r (relative permittivity) we obtain following equation:

$$\vec{D} = \epsilon_0 \epsilon_r \vec{E}. \tag{1.5}$$

We define $\epsilon_0 \epsilon_r$ as a $\tilde{\epsilon}(\omega)$. Considering the causality principle for dispersive materials, that the response is arising after the field is applied, there is a phase (time delay) difference between the excitation and the response. Hence, we can state the complex nature of the dielectric permittivity. It can be given by:

$$\tilde{\epsilon}(\omega) = \epsilon(\omega)' + i\epsilon(\omega)''. \tag{1.6}$$

The imaginary term describes the absorption or sometimes it is called extinction coefficient.

1.1.1 Dielectric function of metals

The gas motion has been explained successfully by Newton's second law. Therefore, an electron gas displacement can be described by the following formula:

$$\vec{F} = m\frac{d^2\vec{r}}{dt^2}, \quad \vec{F} = e\vec{E}. \tag{1.7}$$

By combining the equation 1.1 and 1.7 we obtain for the oscillating electric field the following:

$$\vec{P}(\vec{r},\omega) = -\frac{ne^2}{m\omega^2}\cdot\vec{E}(\vec{r},\omega), \quad \vec{E} = \vec{E_0}(\vec{r})e^{i\omega t} \tag{1.8}$$

The displacement field formula (equation 1.3) takes following form:

$$\vec{D}(\vec{r},\omega) = \epsilon_0\vec{E}(\vec{r},\omega)\left[1 - \frac{ne^2}{m\omega^2}\epsilon_0\right] \tag{1.9}$$

The term in brackets is the frequency dependent dielectric permittivity (ϵ_r). It depends on the mass of electrons and the number of free electrons. We define the plasma frequency ω_p and it has following form:

$$\omega_p^2 = \frac{ne^2}{m}\epsilon_0, \quad and \quad \epsilon_r = 1 - \frac{\omega_p^2}{\omega^2}. \tag{1.10}$$

So far, we have considered that the electrons are simply displaced in the metal by the external electric field force. However, in Drude model of free electrons the collisions exist and that will damp the oscillations with a rate of $1/\tau$. After some calculus taking into account the collisions (damping factor) the ϵ_r becomes:

$$\epsilon_r = 1 - \frac{\omega_p^2}{\omega^2 + i\gamma\omega}, \quad \gamma = 1/\tau. \tag{1.11}$$

The complex permittivity (ϵ_r) is related to the complex refractive index ($\tilde{n}$).

$$\begin{aligned} \sqrt{\epsilon_r} = \tilde{n} &= n + ik, \\ \epsilon' &= n^2 - k^2, \\ \epsilon'' &= 2nk, \end{aligned} \tag{1.12}$$

where, k is the extinction coefficient and n is the refractive index. When $\omega \leqslant \omega_p$ the metal has reflectivity of 1, but in the case of $\omega \geq \omega_p$ the metal acts as a dielectric with positive dielectric permittivity. We derive a wave equation (1.13) using the solution of

Maxwell's equations and linear algebra, when there is not external charge or current density.

$$\vec{k}(\vec{k}\cdot\vec{E}) - \vec{k}^2\vec{E} = \frac{\epsilon_r\omega^2}{c^2}\vec{E}, \tag{1.13}$$

where k is the wave vector, c is the light speed in free space. Let's go to the case, when $\omega = \omega_p$, then $\epsilon'(\omega_p)$ tends to zero! So, the right side of the equation becomes zero, and the only solution occurs when the first term and the second term are equal. It is possible if the wave is not transverse, hence the electric field and wave vector are collinear. One may conclude plasmon waves are longitudinal. These plasmons calls bulk or volume plasmons. There are two families of plasmons the bulk (or volume) plasmons and the surface plasmons. The plasma frequency is linked to bulk plasmons.

1.2 Surface plasmons

The wave vector can be real or imaginary depending on the frequency of EM wave (equation 1.14). We have discussed the properties of metals when they are reflective or transparent relied on the illumination frequency. Let's discuss another family of plasmons: surface plasmons. Indeed, the wave vector is complex at the surface with real part that corresponds to the propagation and the imaginary part to the attenuation. The wave at the surface is evanescent, hence do not radiate as electric field and magnetic field are not transverse to each other. We know that for evanescent waves the vertical component of wave vector (k_z) is imaginary and parallel component is real (k_x). Using the boundary conditions for two interfaces (the scheme is shown in Fig. 1.3a) the general dispersion relation of surface wave is derived as:

$$k_x^2 = \frac{\epsilon_1\epsilon_2}{\epsilon_1+\epsilon_2}\cdot\frac{\omega^2}{c^2} \tag{1.14}$$

where, ϵ_1 is the dielectric permittivity of the light injection medium. We can transform this relation for metal interface by following:

$$k_x^2 = \frac{\epsilon_r}{1+\epsilon_r}\cdot\frac{\omega^2}{c^2} \tag{1.15}$$

One may find the dispersion curve of surface plasmon polariton (SPP) below (Fig. 1.3b). When $k_x \to 0$, then $\omega \to 0$ and when $k_x \to \infty$ then $\omega \to \omega_p/\sqrt{2}$. One may conclude that SPP can exist when $\omega \leq \omega_p/\sqrt{2}$.

Here we show how in-plane momentum (k_x) varies with frequency. What about the out-of-plane momentum (k_z)? We already have mentioned that k_z is imaginary for surface evanescent waves. Unlike Fresnel' evanescent wave the field is decaying

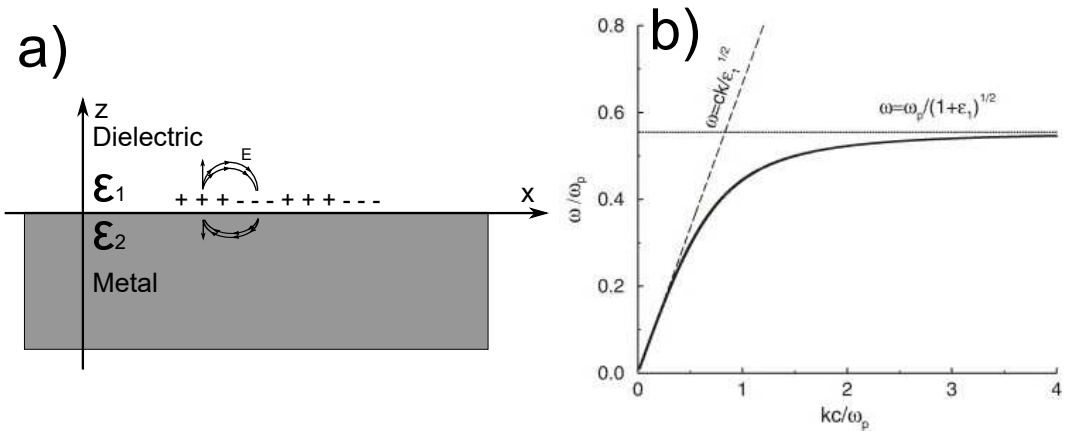

FIGURE 1.3: (a) Schematic of the distribution of the electromagnetic field of SPP at the metal-dielectric interface. (b) Dispersion curve for SPP at interface of Drude metal, when the collisions are negligible (black solid curved). the dash lines show the dispersion of light in the dielectric with dielectric permittivity of ϵ_1. (extracted from Ref. [27])

exponentially on both sides for surface plasmon wave. Note, the charge fluctuations are localized in the z direction within the Thomas-Fermi screening length which is one angstrom. These charge fluctuations associated to the mixed transversal and longitudinal EM field, which dispersers along the surface and the maximum of EM field is at the surface (z=0) position [28, 29]. We deduce that the EM field is very sensitive to the surface properties.

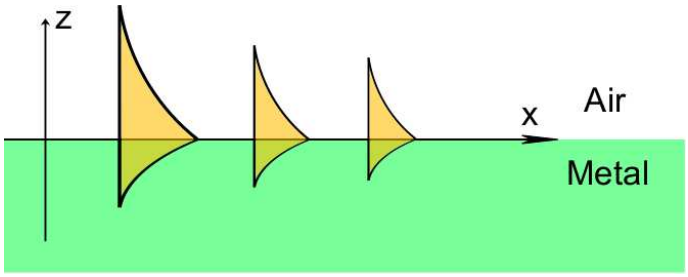

FIGURE 1.4: Schematic of SPP propagation at the metal surface in time. It shows the dissipation of the SPP by traveling some distance.

For metals, the dielectric permittivity is a complex quantity, which implies that the k_x is complex (equation 1.16). Hence, in-plane complex wave vector can be presented as:

$$k_x = k'_x + ik''_x, \quad \text{where} \qquad k'_x = \frac{\omega}{c} \cdot \sqrt{\frac{\epsilon'}{1+\epsilon'}}$$
$$k''_x = \frac{\omega}{c}\left(\frac{\epsilon'}{1+\epsilon'}\right)^{3/2} \cdot \frac{\epsilon''}{2(\epsilon')^2} \tag{1.16}$$

The intensity of plasmon wave traveling along the interface (x-axis) is exponentially decaying by $exp^{-2k''_x \cdot x0}$. The schematic is shown in Fig. 1.4. We define the propagation length of the surface plasmon polariton as:

$$L_{spp} = \frac{1}{2k''_x} \tag{1.17}$$

1.3 Localized Surface Plasmons

According to equation 1.17, the SPP propagation length depends on the imaginary part of the wave vector. For instance, we consider a SPP excited on the silver nanowire of 10 μm length and 100 nm diameter (Fig. 1.5a). SPP is excited by the dipole illumination (broad band source with 500 nm central wavelength) in the near-field. The SPP propagates in the direction showed by the white arrows. This numerical simulation is done in time domain and the figure shows snapshots of certain moments. The SPP excited at the left edge propagates along the nanowire with energy dissipation as it is shown in Fig. 1.5b and 1.5c.

The strong dissipation of the energy during the propagation is due to the intrinsic losses in the silver. When the nanowire is longer than the SPP propagation length, then we see how the SPP disappears after traveling to a certain distance.

The Fig. 1.5d, 1.5e and 1.5f show the SPP propagation snapshots on a 5 μm-length nanowire. The SPP is not completely dissipated before reaching the right edge of the nanowire. One may note that the Fig. 1.5f depicts the energy confinement on the right edge. Indeed, the SPP wave facing a sharp discontinuity like the edge scatters the light from that discontinuity, which has been shown previously [30, 31].

We continue to shrink the length of the nanowire down to 2.5 μm keeping its diameter 100 nm (Fig. 1.5g). The Fig. 1.5h shows the moment, when the wave bounces to the edge of the nanowire and scatters light. For the next instance one may see that the wave losing some part of the energy in scattering is reflected from the right edge and travels back to the left edge.

Then, we go further down to the micron-length nanowire. The Fig. 1.5j-l show the SPP propagation snapshots in time domain in this case. Indeed, the SPP reflects and propagates back to the incipient point (Fig. 1.5l). Actually, when the nanowire is smaller than SPP propagation length, the wave bounces from one to another edge until the final dissipation due to the scattering and intrinsic losses (absorption).

The shrinking of the length of the nanowire increases the electromagnetic wave oscillation numbers from one edge to another edge and becomes a stationary wave. This is a concept of a localized mode. Then what is a resonance? When the system is brought out of the steady state by external force and oscillates harmonically. Indeed, when the

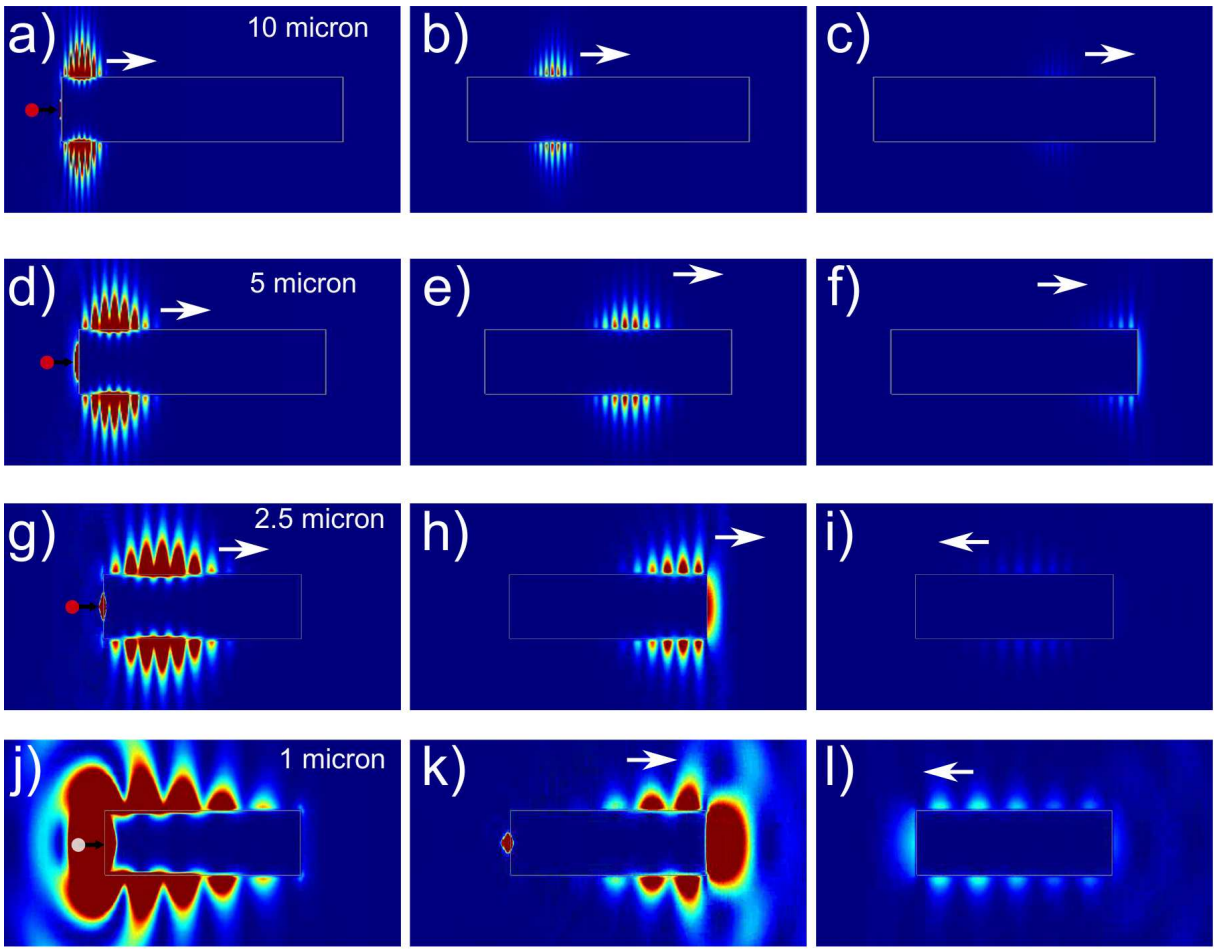

FIGURE 1.5: The snapshots from the numerical simulation in time domain of a SPP propagation on the silver nanowire for certain moments. The SPP is excited by broadband dipole (central wavelength 500 nm) source noted as red or circle at the vicinity of nanowire. The black arrow shows the dipole orientation. The white arrow shows the direction of propagation. The nanorod diameter is 100 nm. (a-c) The length is 10 μm. (b) and (c) show the electric field magnitude for the next instances. (d-f) The simulations for 5 μm, (g-i) 2.5 μm and (j-l) 1 μm lengths.

nanowire or other nanostructure is much smaller than the illumination wavelength, they act as nanoresonators. Hence, their resonances called localized surface plasmon resonances (LSPR).

To summarize, the LSPRs are the particular case of SPP, when the metallic nanoobject is much smaller than the SPP propagation length. The localized surface plasmon resonance, thus, arises when light interacts with conductive nanoparticles (NPs) that are smaller than the incident wavelength. For the nanoparticles of this size, the so-called quasi-static approximation (Rayleigh theory) can be applied. In this case we cannot use the macroscopic dielectric function and its polarizability. The polarizability of spherical nanoparticles is given by:

$$\alpha = 4\pi r^3 \frac{\epsilon(\omega) - \epsilon_m(\omega)}{\epsilon(\omega) + 2\epsilon_m(\omega)} \tag{1.18}$$

where, r is the nanosphere radius, $\epsilon(\omega)$ is the complex dielectric permittivity of the nanosphere and $\epsilon_m(\omega)$ is the dielectric constant of the surrounding medium. One may mark, this equation leads to the Clausius-Mossotti relation. Consequently, the resonant conditions are met when the denominator seeks to zero, $\epsilon(\omega) = -2\epsilon_m(\omega)$. In Fig. 1.6a is plotted the real and the imaginary parts of dielectric function of silver. For small or slow varying imaginary part around the resonance we can simplify the resonant condition as $Re[\epsilon(\omega)] = -2\epsilon_m(\omega)$ [19].

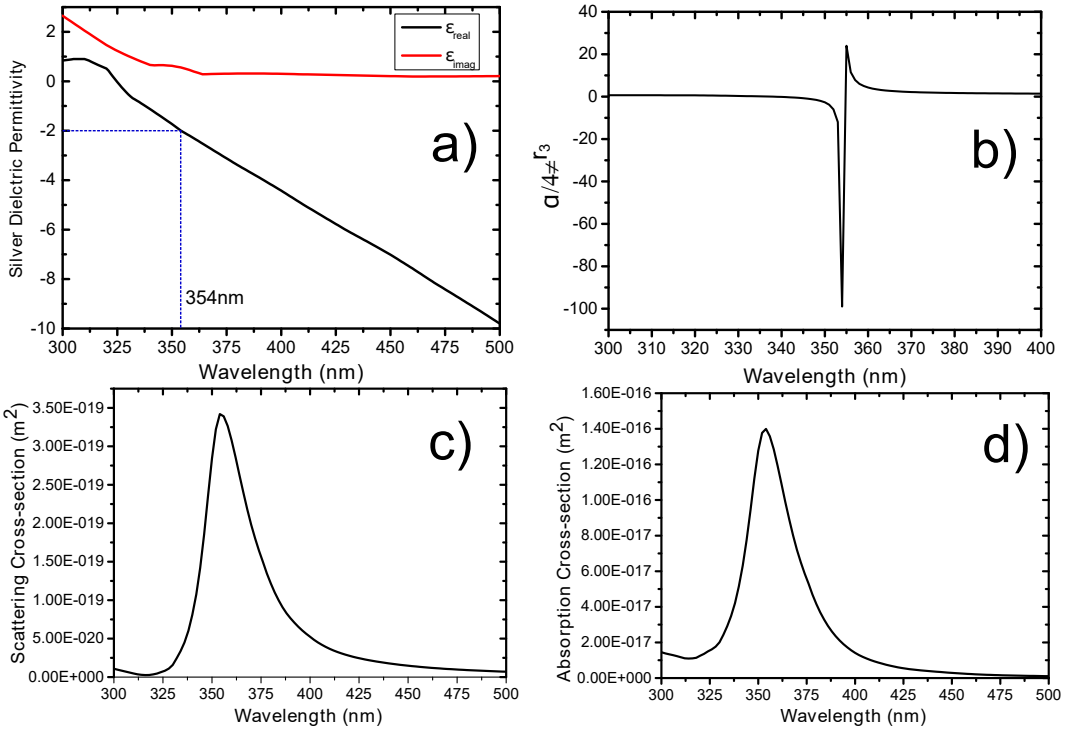

FIGURE 1.6: (a) Dielectric relative permittivity of silver from Johnson and Christy [32]. (b) Polarizablity of a silver sphere normalized by $4\pi/r^3$. The silver is modeled as Drude metal. (c) Scattering and (d) absorption cross-section of 10 nm-diameter silver sphere (Mie Theory).

The resonant condition of silver nanoshpere in air is for the silver dielectric permittivity of -2. This permittivity corresponds to 354 nm. We see that the LSPR depends on the surrounding medium for small nanospheres. If we combine the equation 1.10 (Drude model) and the relation of resonant condition ($Re[\epsilon(\omega)] = -2\epsilon_m(\omega)$), it can explain the LSPR frequency dependence on the refractive index (dielectric constant) of surrounding medium.

$$\omega_{res} = \frac{\omega_p}{\sqrt{1 + 2\epsilon_m(\omega)}} \tag{1.19}$$

The equation 1.19 says that with the increase of the refractive index the resonance frequency is decreased, the resonant wavelength is increased respectively. Moreover,

the resonances are at fixed frequencies depending on the plasmonic material as the dielectric function depends on the wavelengths. In Fig. 1.6b we show the calculated polarizablity of silver nanosphere for a Drude metal, which means we considered only the real part of dielectric permitivitty. We see the highest polarizability is for 354 nm. Usually one measures or calculates the cross-section of scattering or absorption of nanoparticles in order to define the resonance. The absorption and scattering cross-section are given as following:

$$\begin{aligned} C_{sca} &= \frac{k^4}{6\pi}|\alpha|^2 = \frac{8\pi}{3}k^4 r^6 \left|\frac{\epsilon(\omega)-\epsilon_m(\omega)}{\epsilon(\omega)+2\epsilon_m(\omega)}\right|^2 \\ C_{abs} &= kIm[\alpha] = 4\pi k r^3 Im\left[\frac{\epsilon(\omega)-\epsilon_m(\omega)}{\epsilon(\omega)+2\epsilon_m(\omega)}\right] \end{aligned} \tag{1.20}$$

where, k is the wave vector. Considering these equations, the absorption efficiency scaling as r^3 for small nanoparticles dominates over the scattering one (scaling as r^6). The Fig. 1.6c and 1.6d depict the calculated scattering and the absorption cross-sections of 10 nm-diameter silver nanosphere. One may notice that the peak positions match with resonant position (354 nm) determined by polarizability.

We discuss in details the size effect on the absorption and the scattering of metallic nanoparticles in Chapter 2. Note, the extinction cross section is the sum of the scattering and the absorption cross sections, $C_{ext} = C_{sca} + C_{abs}$.

In reality, we do not work with only perfect spheres, then Bohren and Huffman in 1983 gave the polarizability of spheroids previously determined by Rayleigh-Gans theory, which is following [33]:

$$\alpha = 4\pi r_1 r_2 r_3 \frac{\epsilon(\omega)-\epsilon_m(\omega)}{3\epsilon_m(\omega)+3L_i(\epsilon(\omega)-\epsilon_m(\omega))} \tag{1.21}$$

,

where r_1, r_2, r_3 are the semiaxis of the ellipsoid and L_i is the geometrical factor. This geometrical factor for each semiaxis depends on the ratio between its dimension and all three axis dimensions. Moreover, the some of the geometrical factor of three axis should be equal to 1. This parameter is given for the axis which is polarized along the electromagnetic field. The equation 1.21 shows that the LSPR depends on the geometry of the nanostructure.

Grand *et al.* show the calculated LSPR peak positions of the ellipsoids, prolate and oblate spheroids, using quasi-static approximation of different size (Fig. 1.7) [34]. The particles considered in calculations are 50 nm or bigger which is already out of the quasi-static limit. They used the first order corrections, as the expressions for the polarizabilities of spheres and ellipsoids are valid only for very small nanoparticles in the quasi-static approximation. The study shows that small prolate and oblate spheroids

with the same major axis length have similar peak positions, since the geometrical parameter for the polarizability is similar. Herein, we clearly see the shape effect on LSPR peak positions. The peak positions shifts become more evident for bigger sizes due to the combination of shape and size effects on the LSPRs.

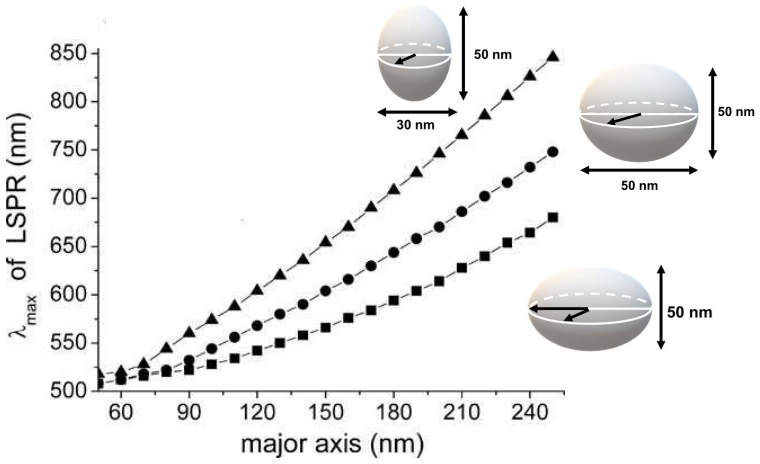

FIGURE 1.7: Quasi-static calculation using first order corrections of the spectral position of LSPR, plotted against the major axis of the gold particle. Squares: oblate particles, major two axises are equal, the third axis is fixed (height) at 50 nm ; circles: prolate particles, the two minor axises with fixed lengths is 50 nm; triangles: ellipsoids, one of the axises length is fixed at 50 nm, the second axis at 30 nm. The figure is adapted from [34].

Indeed, these tremendous properties of metallic nanoparticles have been used since ancient times. The complete theory was given by german scientist Gustave Mie. He demonstrated the Maxwell's equations solution for a spherical nanoparticle in 1908 and developed so-called Mie or Lorenz-Mie theory, where the size parameter is included . He presented the complete theory of scattering and the absorption for spheres out of quasi-static limit.

In Fig. 1.8 we can see the extinction and scattering spectra of different shape and size nanoparticles. The extinction spectra show the light lost during passing through the colloidal solutions.

The flacons in Fig. 1.8i show different colors depending on the sizes of the colloidal nanoparticles. For example, spectrum of the blue flacon shows a peak position of extinction spectrum at 546 nm. The nanoparticles (nanoplates) average diameter is 32 nm and thickness is 12 nm. This spectrum shows that the green, yellow and partly red parts of visible light is lost passing through the solution, therefore we see blue - the rest of the visible light. In this manner we see different colors for different size, as some part of the light spectrum is lost due to absorption and scattering of metallic nanoparticles. For example the nanoplates with a diameter of 78 nm show a peak position at 726 nm on the extinction spectrum and the corresponding flacon colors light blue. The

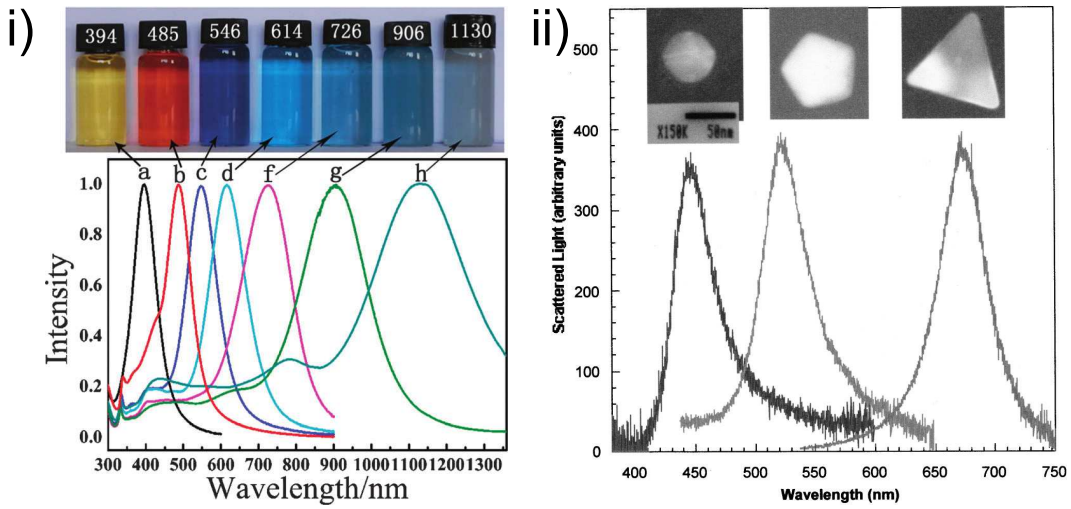

FIGURE 1.8: (i)Images of silver seeds (a) and silver nanoplate (b–h) colloids of different sizes with different colors and corresponding UV-vis-NIR extinction spectra. The numbers at the top are the wavelengths of the LSPR peak position [35]. (ii) The scattering spectra for silver individual nanoparticles [36].

Fig. 1.8ii shows the influence of the shape on the scattering spectrum of individual nanoparticle.

To summarize, the main difference between the surface plasmons and the localized surface plasmons is that LSPRs are at fixed frequencies. These resonances are sensitive to several factors such as size, shape, morphology, surrounding medium, chosen material etc.. These dependencies allow to tune the resonance spectral position by manipulating these factors.

1.4 Plasmonics in applications

The optical properties of metals have a huge potential for applications. The range of application based on the plasmonic properties is very wide such as enhanced spectroscopies, bio and chemical sensing, solar cells, color generation, heat treatment, subwavelength optical imaging and plasmonic lasing.

1.4.1 Color Generation

The plasmonic properties of metallic nanoparticles is used for ages in order to create the colors in mesoscale. The most popular examples are the Lycurgus Cup produced in Roman Empire (4^th century). The glass of this cup contains gold and silver powder.

When the cup is shined from outside (Fig. 1.9a) it looks green due to the scattering caused by LSPR in green range. When the cup is shined from inside (Fig 1.9b) glass

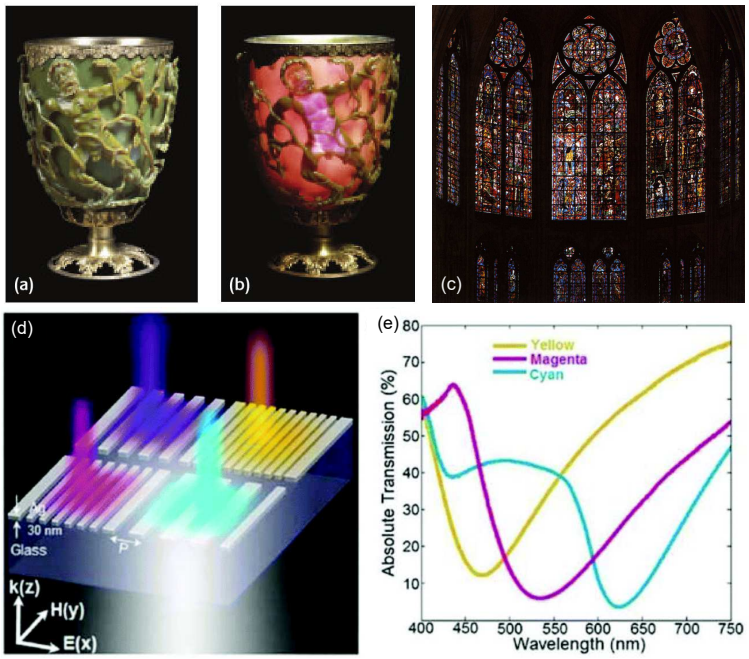

FIGURE 1.9: Lycurgus roman cup (a) in reflected (b) and in transmitted light [37]. (c) Stained glasses on the vitrines of the Cathedral of Troyes. (d) Schematic of the grating color filter of 30 nm thick Ag grating with different periods. (e) Measured transmission spectra corresponding to yellow, magenta and cyan colors for the structure in (d). [38]

appear to be red due to the LSPR causing absorption in the green range. Another example of a color generation caused by the optical properties of metallic nanoparticles is pictured on the Fig. 1.9c. The progress in nanofabrication processes allow to produce nano or microstrucures of different configurations. Gu et al. show a color generation at microscale using nanostructured silver pallets of different size and periods (distance between the pallets) [38]. In Fig 1.9d is shown the schematics of different pallets and on the Fig. 1.9e is drawn the transmission spectra obtained experimentally. We can see the clusters show different colors at nanoscale, which can be used for examples for high resolution screens with very small pixel size.

1.4.2 Bio-Sensing

Multiple papers have been published on a bio-chemical sensing based on plasmonic resonances. Cooper reviewed an example of plasmonic sensor in order to determine the affinity and kinetics of a wide variety of molecular interactions in real time, without the need of molecular labeling (Fig 1.10). This kind of bio-sensor is envisaged to characterize the interactions between receptors that are attached to the biosensor surface and ligands that are in solution above the surface. SPR is changed due to the refractive index changes in the intermediate.

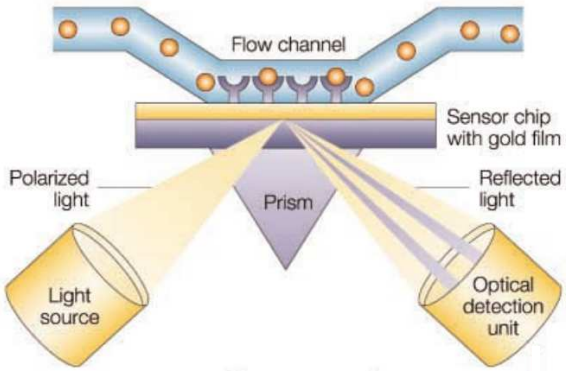

FIGURE 1.10: Experimental setup for an SPR based biosensor. SPR detects changes in the refractive index in the immediate vicinity of the surface layer of a sensor chip. SPR s observed as a sharp shadow in the reflected light from the surface at an angle that is dependent on the mass of material at the surface. (The figure and the caption are adopted from [39])

SPR is observed as a dip in the reflected light spectrum from the surface at an angle that is dependent on the refractive index of solution [40]. The refractive index of the solution defined by mass of "ligands". Besides the SPR, the LSPR changes caused by the refractive index variation can be used in biosensing. The molecules bound in the vicinity of nanoparticles causes a change of the effective refractive index, which leads to a shift of the resonance peak position.

Horrer et al. showed experimentally and numerically a nice example of a sensor based on LSPR. They used an array of MIM (metal-insulator-metal) structures for the sensing. In Fig. 1.11a is shown the single element schematic of the array.

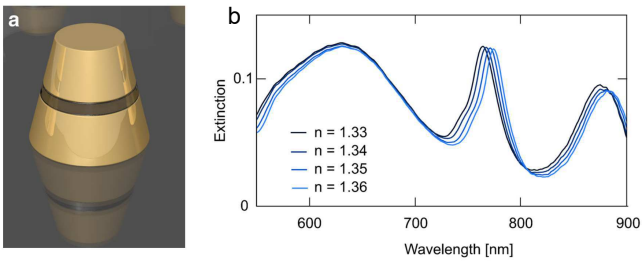

FIGURE 1.11: (a) Schematic of the vertical gold–SiO_2–gold dimer. (b)Sensitivity measurements in water–glycerin solutions with different mixing ratios to vary the refractive index.[40]

The array shows three peak position corresponding respectively to symmetric dipole (around 630 nm), lattice mode (around 770 nm) and antisymmetric dipole mode (around 880 nm). The main resonance shifts are recorded for lattice mode and anti-symmetric dipole mode, when the water–glycerin solutions of different refractive indexes are tested. They demonstrate a sensor based on LSPR, which is sensitive for refractive indexes changes with step of 0.01. The highest sensitivity was reported as 0.003 [41].

1.4.3 Chemical-sensing

One of the main axis of development and use of plasmonic materials is the improvement of the Raman scattering sensitivity. Raman spectroscopy is an efficient tool for material study through vibrational and rotational energy levels, which are a kind of fingerprints for molecules. Raman scattering is an inelastic interaction, when the scattered photon has higher (Anti-stokes) or lower energy (Stokes) than incident photon energy. The energy difference (Raman shift) between the incident and scattered photons describes the vibrational modes of a molecule. The majority of the works studies the Stokes scattering as the Anti-stokes process has smaller probability. The main drawback of Raman scattering is its extremely small probability of the scattered photons (1 in 10 million). Surface plasmons of metals are widely used for the Raman signals enhancement.

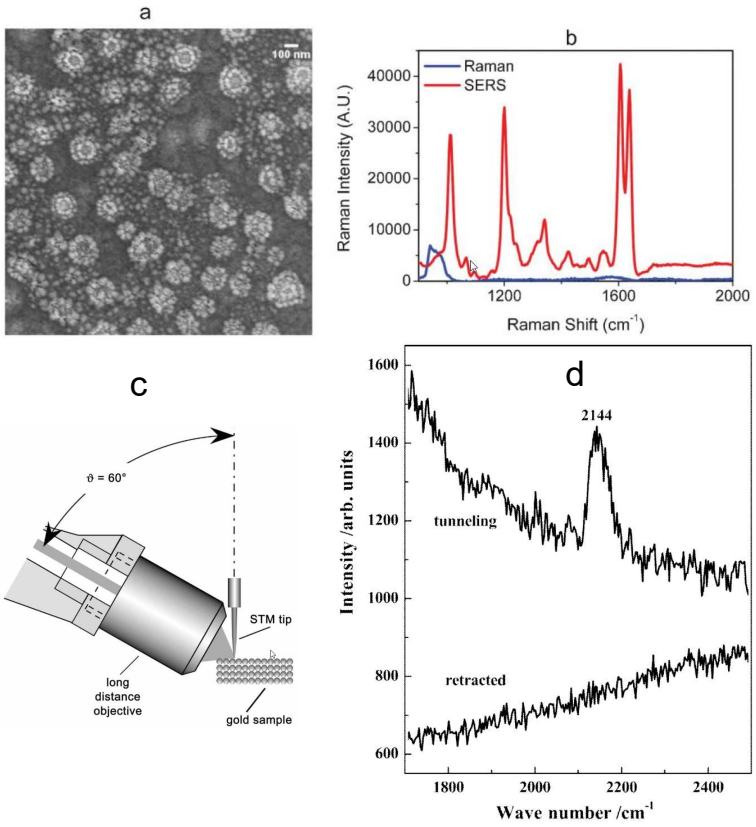

FIGURE 1.12: (a) SEM image of Ag nanocluster deposited on glass. (b) The SERS spectrum of BPE obtained from a single nanocluster. [42] (c) Schematic of the experimental setup for TERS. (d) TERS for CN^-. Bottom curve for the tip-retracted case and top curve for the tip-tunneling case. [43]

There are two main techniques for enhancing Raman scattering such as surface enhanced Raman scattering (SERS) and Tip enhanced Raman scattering (TERS). For the SERS spectroscopy, rough metallic surfaces or metallic nanostructures are used. The adsorbed molecules in the vicinity of metallic nanostructures exhibit an enhanced

Raman scattering under the laser illumination. Indeed, the Raman signal is roughly proportional to the fourth power of the electric field. Since the metallic nanostructures have a highly confined strong electric field under resonant excitations, a molecule locating in this electric field will exhibit stronger Raman scattering. The Fig 1.12a shows scanning electron microscopy image of Ag nano corn-flakes, which were used for SERS of BPE (Bis(phenylethynyl)naphthacene) molecules. These nano-structures demonstrate strong enhancement of Raman signals shown in Fig 1.12b. One may notice, the Raman spectrum is not detectable for a chosen concentration in contrast to SERS.

Another enhanced Raman spectroscopy technique is the TERS, which is an aperture-less optical near-field technique [44–46]. The tip of an atomic force microscopy (AFM) or a scanning tunneling microscopy (STM) can be used to enhance locally the electromagnetic field of an incoming light wave on the vicinity of the probing specimen. TERS may be used for any kind of sample and this technique does not need a rough or nanostructured surface in contrast to the SERS. Moreover, the Raman enhancement can be obtained at any point of the sample, which can lead to the Raman map drawing. In order to additionally increase furthermore the enhancement factor, a metallic surface is used to create a higher confined electric field between the tip and the surface. In other words, the spatial disposition of a gap mode provides a strong enhancement of the Raman signal coming from the specimen placed there. Fig. 1.12c shows the experimental setup of TERS probing a specimen on a metal surface. The TERS of CN^{-}(cyanide) ions adsorbed on a gold surface is depicted on the Fig 1.12d.

"Another mode of accumulating power arises from lifting a weight and then allowing it to fall"

Charles Babbage

2 Localized surface plasmon modes

2.1 Introduction

The Localized Surface Plasmon resonances are widely used in multiple applications. Part of them are not concerned in the internal nature of the resonances, but only concentrate on the macro properties of the system. The metal colloidal disordered films are successfully used in surface enhanced fluorescence and Raman scattering, when only the signal is recorded from wide area [47–52]. However, more precise applications connected with single nano-object measurements, require deep understanding of the plasmonic modes appearing and behavior [53, 54].

We mentioned in the General Introduction and the Chapter 1 that the shape and size of nano-objects play an essential role in the LSPRs (shown respectively in Fig. 2 and 1.8). In this chapter, we discuss the theory of the plasmonic modes and study the LSPRs dependence on the dimensions of nano-objects. We show that light can couple with different plasmonic modes under the various illumination conditions. Then, we introduce a simple numerical method to study the plasmonic modes of asymmetric nanoparticles. Usually, only the changes of dipolar mode for the nanoparticles of different shape and size are monitored. Herein, we investigate size effects on the other modes than a well-known dipolar mode.

Localized Surface Plasmon resonances

In the first chapter we discussed the polarizability of the nanosphere, which allowed to predict the spectral position of LSPR. According to the equation 1.20, the resonant conditions are met, when dominator is zero and $\epsilon(\omega) = -2\epsilon_m(\omega)$.

When LSPR is excited, the opposite electric charges tend to the counter sides of the nanoparticle and creates an electric dipole. In the quasi-static limit, i.e. when the size of the particle is very small compared to the wavelength, the resonance position is assumed to be independent on the nanoparticle size. In this limit the electric field is uniform across the nanoparticle and the multipolar modes do not couple to the planewave. The approximation of the uniform field over the volume of the particle is no longer valid for the particles whose sizes are comparable with the excitation wavelengths. These nano-objects, besides the dipolar mode, may sustain higher order modes known as quadrupole, hexapole, octupole and etc. [55–57].

The Fig. 2.1a shows the calculated extinction spectra of the silver nanospheres in air. A single mode is observed for nanospheres with 40 nm and 60 nm diameters, since the illumination wavelengths are long enough compared with the sizes of the nanospheres. The bigger nanospheres show the second plasmonic mode around 355 nm in form of the shoulder (80 nm diameter) or a peak (120 nm diameter) on the extinction spectra. With increase of the size of nanoshperes the response of the electron cloud to the incident electric field is delayed due to retardation effect [58–60].

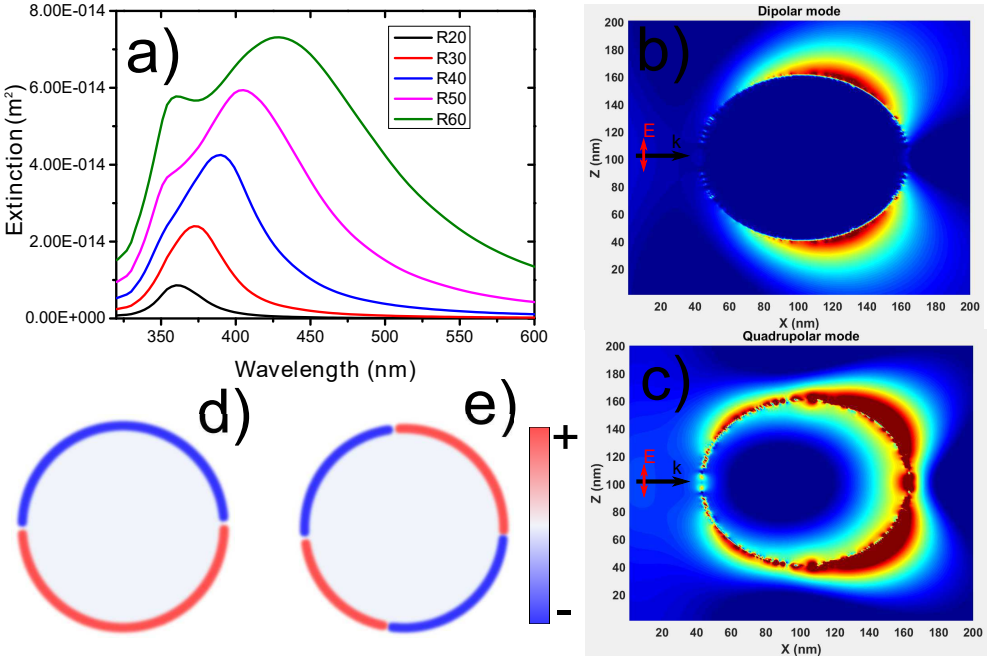

FIGURE 2.1: (a) Extinction spectra of silver nanoshperes calculated by Mie theory for vacuum. The radii vary from 20nm to 60 nm. (b) Electric field map for the excitation at the 428 nm and (c) 358 nm. (d) and (e) are the calculated charges distribution respectively by FDTD.

We present the electric near-field map for two positions of the extinction spectrum of 120 nm diameter nanosphere on the Fig. 2.1b and 2.1c. From the first view the electric field map for 428 nm excitation shows dipolar distribution and map for 358 nm shows quadrupolar mode characteristics. In order to better identify the plasmonic modes we calculated the charge distributions of these two modes (Fig. 2.1d and 2.1e). The plasmonic modes are identified by characteristic two (dipolar) and four (quadrupolar) nodes. Indeed, the higher order modes (quadrupole, octupole and etc.) can be excited by a plane-wave, when there is a phase variation inside the nanoparticle along the illumination axis [58, 60].

The plasmonic modes of spheres and spheroids nano-objects are the most studied. If we consider a nanocylinder which is the second most studied nano-object, whose planes (bottom and top) are in XY plane, the excited dipolar mode (shown in Fig. 2.2a) is aligned with the incident electric field. When the thickness of the nanocylinder is small compared with the illumination wavelength it may sustain only dipolar mode like small nanospheres. Unlike the nanospheres, the nanocylinders plasmonic modes are sensitive to their orientation respected to the planewave. When the nanocylinder is excited by the X-axis oriented EM wave from Y-axis, it may sustain in-plane quadrupolar mode (Fig. 2.2b), while for another orientation it sustains only dipolar mode (Fig. 2.2a). Outside the quasi-static limit, the phase variation of the electric field in nanoparticle creates two electric dipolar moments, countering each other on the plane of the nanodisk.

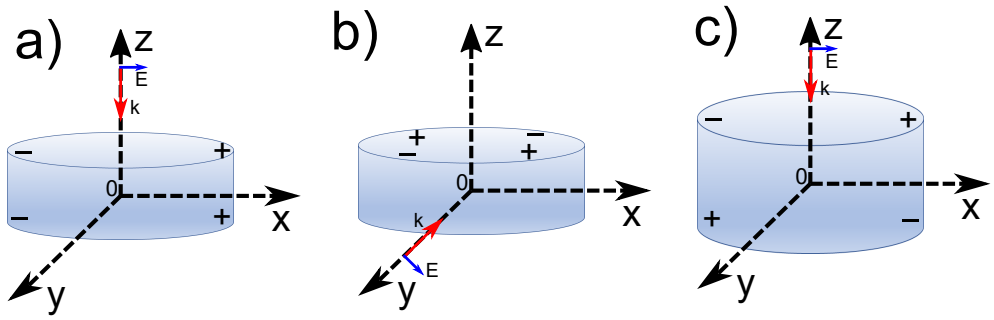

FIGURE 2.2: Scheme of the excitation of (b) dipolar, (b) in-plane quadrupolar and out-of-plane quadprupolar modes of a nanocylinder. The red arrow shows the wave vector and the blue arrow is the electric field (polarization)

A thicker nanocylinder can enhance the retardation effect, which induces excitation of the higher order modes like out-of-plane quadrupolar mode (Fig. 2.2c). Surrounding medium with a higher refractive index than air can enhance also the retardation effect, therefore higher order modes can be excited, even if they are not excited in air. Indeed, Yang et al. demonstrated experimentally an excitation of the quadrupolar mode sustained by aluminum nanocylinders in a hexagonal array surrounded by a symmetrical medium of refractive index 1.5 [61]. In this paper, the out-of-plane quadrupolar

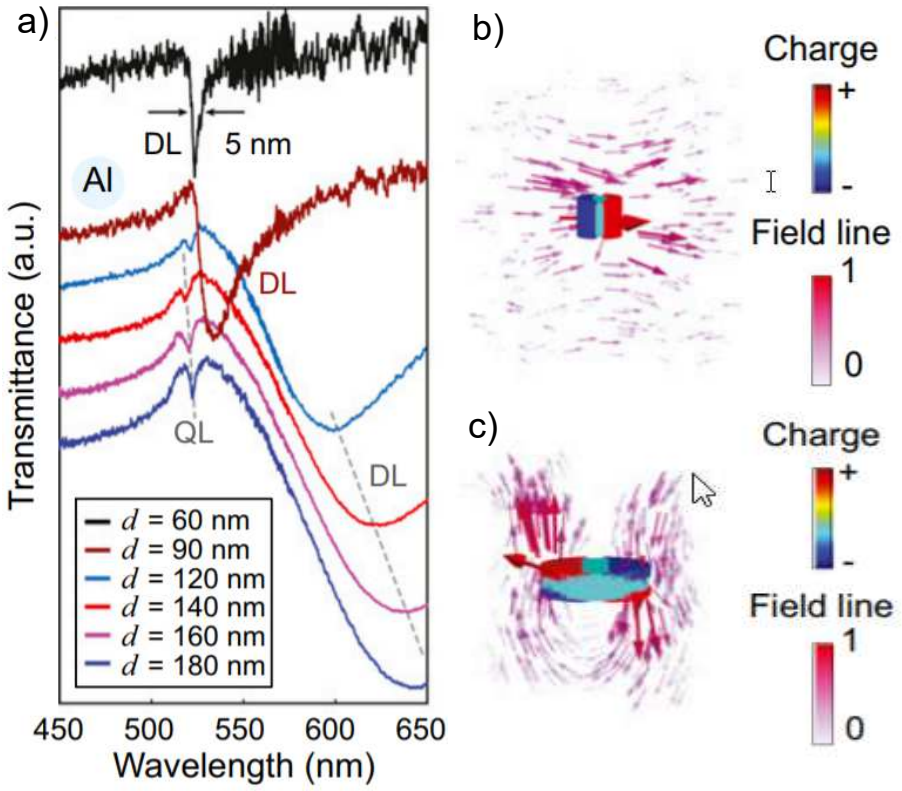

FIGURE 2.3: (a) Measured transmittance as a function of nanoparticle diameter with 35 nm height (d) of aluminum hexagonal arrays with 346nm spacing. The environment refractive index is 1.5. Charge distribution and the electric field lines of (b) dipolar and (c) quadrupolar lattice modes on resonance (x-z cross-section, z is out-of-plane direction). (extracted from [61])

mode is coupled successfully to the lattice resonance (the lattices modes are in-plane diffraction orders of an array). Fig. 2.3a shows the transmittance spectra of aluminum nanoparticles of different diameters in arrays. The electric charge distributions of dipolar and quadrupolar modes are shown respectively in Fig. 2.3b and 2.3c. They observed that a single nanoparticle quadrupolar resonances couple weakly with a light and are observed rarely even in ensemble of nanoparticles, when they are not coupled with lattice mode.

2.2 Numerical simulations

The 3D numerical simulations are done with a help of a commercial software from Lumerical, FDTD solutions based on a finite difference time domain method. The main idea of this method is to solve the Maxwell's equations in time domain using a discretization in time and space. First time FDTD was proposed by Yee in 1966 [62]. For better understanding the theory of the method we consider a simple one dimensional problem. The Maxwell's equation can be written as:

$$\begin{aligned} \frac{\partial \vec{E}}{\partial t} &= -\frac{1}{\epsilon_0}\nabla \times \vec{H} \\ \frac{\partial \vec{H}}{\partial t} &= -\frac{1}{\mu_0}\nabla \times \vec{E} \end{aligned} \tag{2.1}$$

For one dimensional case we can use only E_x and H_y, equations 2.1 can be modified as:

$$\begin{aligned} \frac{\partial E_x}{\partial t} &= -\frac{1}{\epsilon_0}\frac{\partial H_y}{\partial z} \\ \frac{\partial H_y}{\partial t} &= -\frac{1}{\mu_0}\frac{\partial E_x}{\partial z} \end{aligned} \tag{2.2}$$

Yee's method considers that E_x and H_y are shifted in space by half a cell of discretization and in time by half a time step. In this a case, equations 2.2 using the central difference approximation of the derivatives can be expressed as:

$$\frac{E_x^{n+1/2}(i) - E_x^{n-1/2}(i)}{\Delta t} = -\frac{1}{\epsilon_0}\frac{H_y^n(i+1/2) - H_y^n(i-1/2)}{\Delta z} \tag{2.3}$$

$$\frac{H_y^{n+1}(i+1/2) - H_y^n(i+1/2)}{\Delta t} = -\frac{1}{\epsilon_0}\frac{E_x^{n+1/2}(i+1) - E_x^{n+1/2}(i)}{\Delta z} \tag{2.4}$$

In order to explain the equations 2.3 and 2.4 we present the one dimensional discretization model of Yee in time and in space in Fig. 2.4. The left term of equation 2.3 is the derivative of the electric field (E) at time n Δ t is expressed as a central difference using electric field values at times (n+1/2) Δ t and (n-1/2) Δ t.

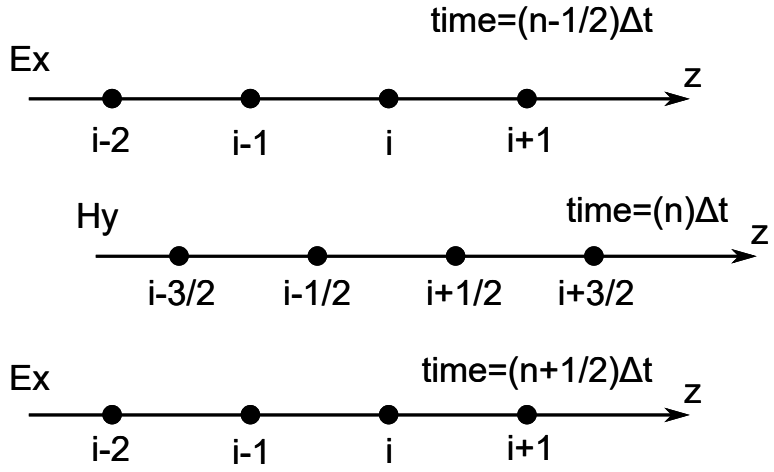

FIGURE 2.4: Yee's one-dimensional scheme for discretization of electric and magnetic fields in space and time.

The right term in equations 2.3 expresses the magnetic field (H) at point iΔz as a central difference using magnetic field (H) values at points (i+1/2) Δ z and (i-1/2) Δ z. These approximations calculate always the electric field (E) values at points . . . , (i-1)Δz, iΔx, (i+1)Δx, . . . and times . . . , (n-3/2)Δt, (n-1/2) Δt, (n+1/2) Δt, . . . and to calculate the H field values at points . . . , (i-3/2) Δz, (i-1/2) Δz, (i+1/2) Δz, . . . and times . . . , (n-1) Δt, n Δt, (n+1) Δt, ... This approach can be expended to 3 dimensions (3D) in order to solve the electromagnetic problem in 3D.z One of the characteristics of the FDTD model is that single simulation can cover wide spectrum range of frequencies as it is in time domain. The calculated electromagnetic field (E(t), H(t)) in time is converted in electromagnetic field (E(ω), H(ω)) in frequencies using Fourier transform.

In Fig 2.5 we show a model extracted from Lumerical software (visualization of XZ profile). A gold nanocylinder is placed on the glass substrate. We use a Total field scattered field (TFSF) source with linear polarization. The plane wave is injected only inside the TFSF box and only the scattered field propagates out of the box. The several monitors and analysis boxes are used in order to determine scattering and absorption spectra. The analysis box called "Absorption" on the Fig 2.5a shows the difference between the injected field power in the analysis box and scattered out light power from the analysis box caused by the nanoparticle. The analysis box called "Total scattering" calculates a total power scattered by the nanoparticle as the light source is not propagating out of TFSF box. We use two monitors for calculating separately a forward and a backward scattering placed below and above the TFSF box, respectively. Fig 2.5b shows a screen-shot of the field propagation, when the injected field is limited spatially by the TFSF box. The extinction spectrum is achieved by summing the absorption and scattering spectrum. We choose a discretization mesh equal to 1nm. We use as boundaries for simulation box the perfect matching layer (PML), which absorbs scattered field [63].

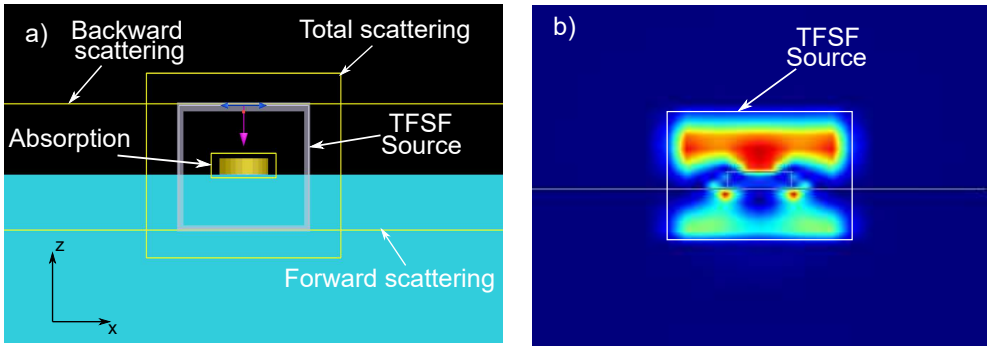

FIGURE 2.5: (a) A model of a single gold nanocylinder extracted from FDTD solutions. The pink arrow shows the wave vector direction and the blue one shows the electric field oscillation direction. (b) Screen-shot of the electric field propagation in the TFSF box.

2.3 Horizontal and vertical dipolar modes

The nanocylinders may exhibit two states of dipolar mode called horizontal (in-plane) and vertical (out-of-plane). In this section, we study comparatively the dimension effect on these orthogonally directed dipolar modes. We investigate the impact of the nanocylinder diameter on the vertical dipolar mode peak position and the effect of the nanocylinder height change on the horizontal dipolar mode peak position. There are very few studies on vertical dipolar modes. One of the pioneering paper that mentioned the vertical mode was published by Jin *et al.* in 2001 [64]. They used a colloidal solution of silver nano-prisms of different sizes and oriented randomly in the solution. Horizontal or/and vertical dipolar modes were exited depending on their orientation to the illumination axis. Also, they demonstrated that the vertical dipolar mode is weak and broad and then it is barely discernible.

Then, in 2011 Zhou *et al.* published a paper about vertical dipolar mode interactions with a lattice mode [65]. They studied gold nanoparticle arrays embedded in a polyurethane (n=1.34) matrix on a glass substrate. They showed by numerical simulation that it is possible to excite a couple state between a vertical dipolar mode and a lattice mode, while the isolated nanoparticle exhibits only the horizontal dipolar mode for the same illumination conditions. These examples show that the excitation and recording of the vertical mode of the single nanoparticle is a hard issue.

2.3.1 Horizontal Dipolar mode

In Fig. 2.6 we present a calculated map of absorption, scattering and extinction spectra for gold nanocylinders of different heights. The extinction spectra maps representing the sum of the absorption and the scattering spectra. The surrounding medium is vacuum. The incident polarization (electric field direction) is along the diameter of GNC, the scheme is on the inset of Fig. 2.6. For a 70 nm-diameter GNC, the LSPR peak shifts for about 20 nm with the change of the cylinder height from 20 nm to 55 nm. While this difference for 170 nm-diameter GNC is 60 nm.

One may note that the peak position of the horizontal dipolar mode depends on the ratio between the diameter and the height. When the ratio increases, the horizontal dipolar mode shifts more. To understand the relation of the peak position and the aspect ratio, we present in Fig. 2.7b these dependencies for different diameters. One may note, that the relation is linear and the curves are almost parallel. Indeed, many papers proved the linear behavior of the LSPR-aspect ratio dependence for nanorods [41, 66–68].

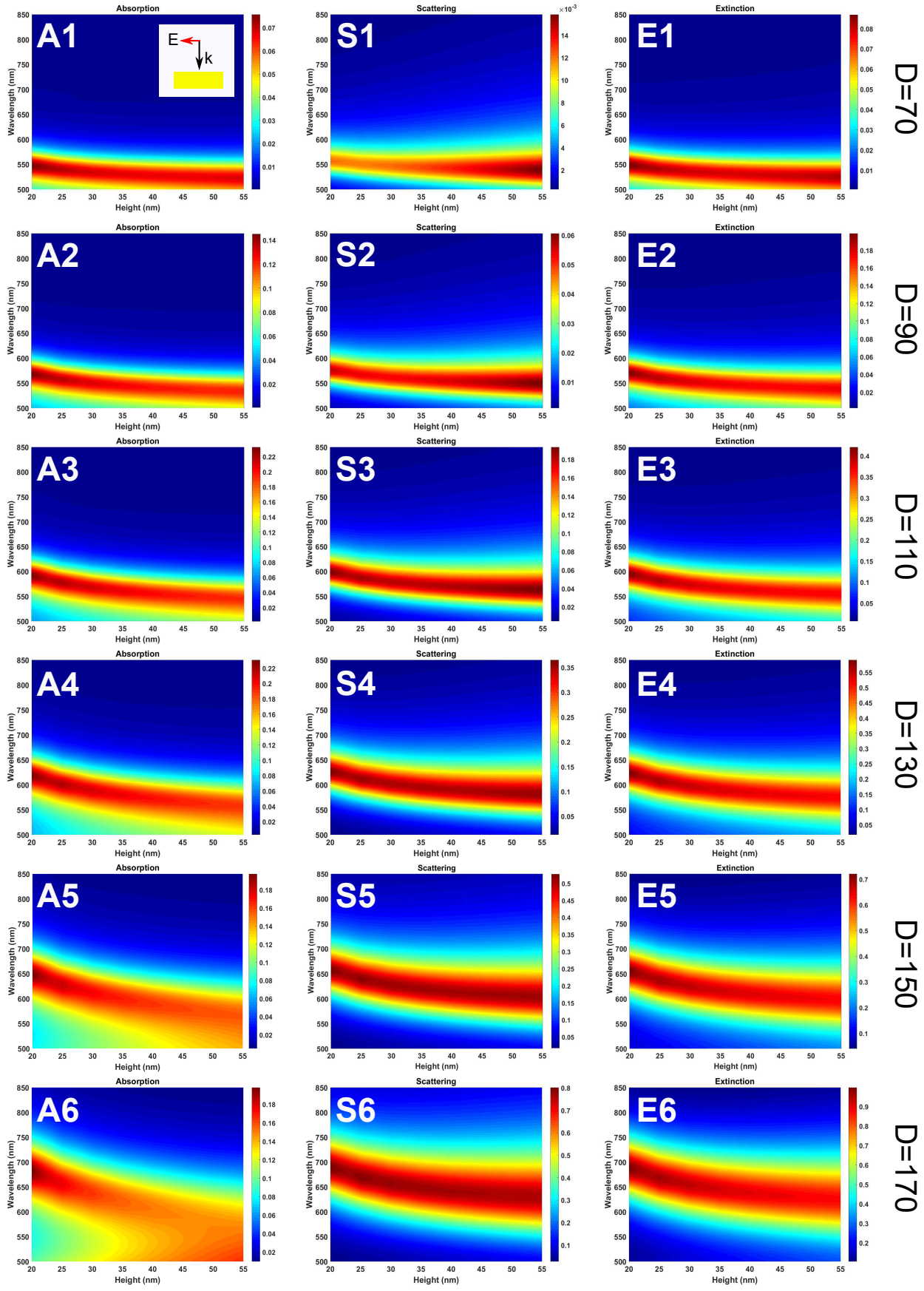

FIGURE 2.6: Calculated absorption, scattering and extinction spectra map of GNC for different diameters depending on the height. D is the diameter. The surounding medium is air.

However, there is no any evidence of collinearity. We can write a linear function as:

$$\lambda_{peak} = \lambda_0 + br, \tag{2.5}$$

where the r is aspect ratio. When $r \to 0$, $height \to \infty$, as r = diameter/height. Therefore, λ_0 shows the peak position of the resonance for infinite cylinder. The infinite nanocylinder, is practically a nanowire. We assume in this manner it is possible to predict the peak position of transverse plasmonic mode of a nanowire (r≪L, r-diameter, L is length). k is the slope of the curves, which is a universal number for all diameters, and is around 11.7. Knowing b, which is the characteristic of the material, and knowing the peak position for a cylinder of one diameter, it is possible to predict the resonant position for all aspect ratios of the same diameter using the the equation 2.5.

One can see in absorption maps that for thinner GNC the absorbed power is higher for the same diameter. The absorption maps for bigger and higher GNCs show the wide absorption band without a distinguishable peak position.

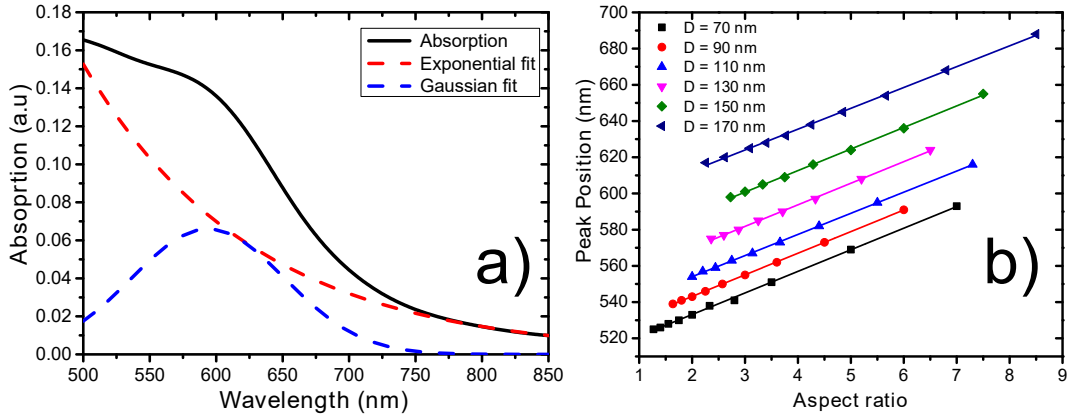

FIGURE 2.7: (a) Absorption spectrum (black solid curve) of 170 nm-diameter and 55 nm-height GNC in air. The dashed lines are the fits of absorption spectrum by exponential and Gaussian functions (b) The dependence of horizontal dipolar mode peak position from aspect ratio, calculated for different diameters.

For example, absorption map for 170 nm-diameter GNC above 35 nm height (Fig. 2.6 map A6) do not show resonant-like characteristics, when the GNCs of 20 or 30nm heights show the peak positions receptively at 680 nm and 637 nm. We show the absorption spectrum of 170 nm-diameter and 55 nm-height GNC on the Fig. 2.7a. We can see the exponential decay of the curve of the spectrum and small bump around 590 nm. The absorption spectrum is fitted by exponential and Gaussian profiles. This spectrum shows that the inter-band transitions become more important than plasmonic resonance.

Another observation is connected with the intensity variation of the plasmonic resonances depending on the height. The extinction spectra maps show that the thinner GNC exhibit more intense resonances at their peak positions. As a conclusion, a thin GNC is more convenient to use as it has bigger extinction cross-section at peak position of the resonance in the context of using the horizontal dipolar mode in applications.

2.3.2 Vertical dipolar mode

We illustrate the absorption, scattering and extinction spectra maps of GNCs for different heights depending on their diameters in Fig 2.8. Herein, we investigate the vertical dipolar mode. The illumination scheme is shown on the absorption spectra map when the heights of GNCs is 20 nm (H=20). As the resonances are close to the strong transition band the baseline are taken from the spectra. We choose a baseline of exponential decay as the spectrum of interband transitions of gold in the wavelength range from 450 nm to 800 nm shows an exponential lineshape [69] One may notice, that the peak position of the vertical dipolar mode of thin GNC is quite stable with a diameter variation. For example, between 70 nm-diameter and 210 nm-diameter GNCs the shift of the absorption peak is 5 nm, when their height is 20 nm (Fig. 2.8 map A1). The difference between 70 nm-diameter and 210 nm-diameter peak positions of the scattering spectra is 5 nm (Fig. 2.8 map S1). While we saw that the horizontal dipolar mode highly depended on the height for any diameter.

The extinction spectra map of 20 nm height does not differ much from the absorption map, as the scattered power is 10 times smaller the absorbed power (Fig. 2.8 maps A1, S1 and E1). A big thin GNC like 170 nm-diameter and 20 nm-height has stronger absorption than the scattering for the vertical dipolar mode, and stronger scattering than the absorption for the horizontal dipolar mode (Fig 2.6 map A6, S6 and E6).

One may notice that the diameter does not play an essential role on the behavior of the vertical dipolar mode. We state that the main factor influencing the vertical dipolar mode is the height. However, with the increase of the GNC height the peak positions of vertical mode begin to depend on the diameter. There is a kind of threshold when the peak position shifts become abrupt for thicker GNC in the absorption spectra maps. For example, for the 60 nm-height GNC peak position shift become obvious when the diameter is 90 nm or below (Fig. 2.8 map A5), and for 70 nm and 80 nm height are respectively 110 nm and 120 nm (Fig. 2.8 map A6 and A7). One may see when the ratio between the diameter and height is smaller than 1.5 the peak position changes appear clearly. We assume that the vertical mode dependence on the diameter is minimal when the diameter-height ratio is higher than 1.5.

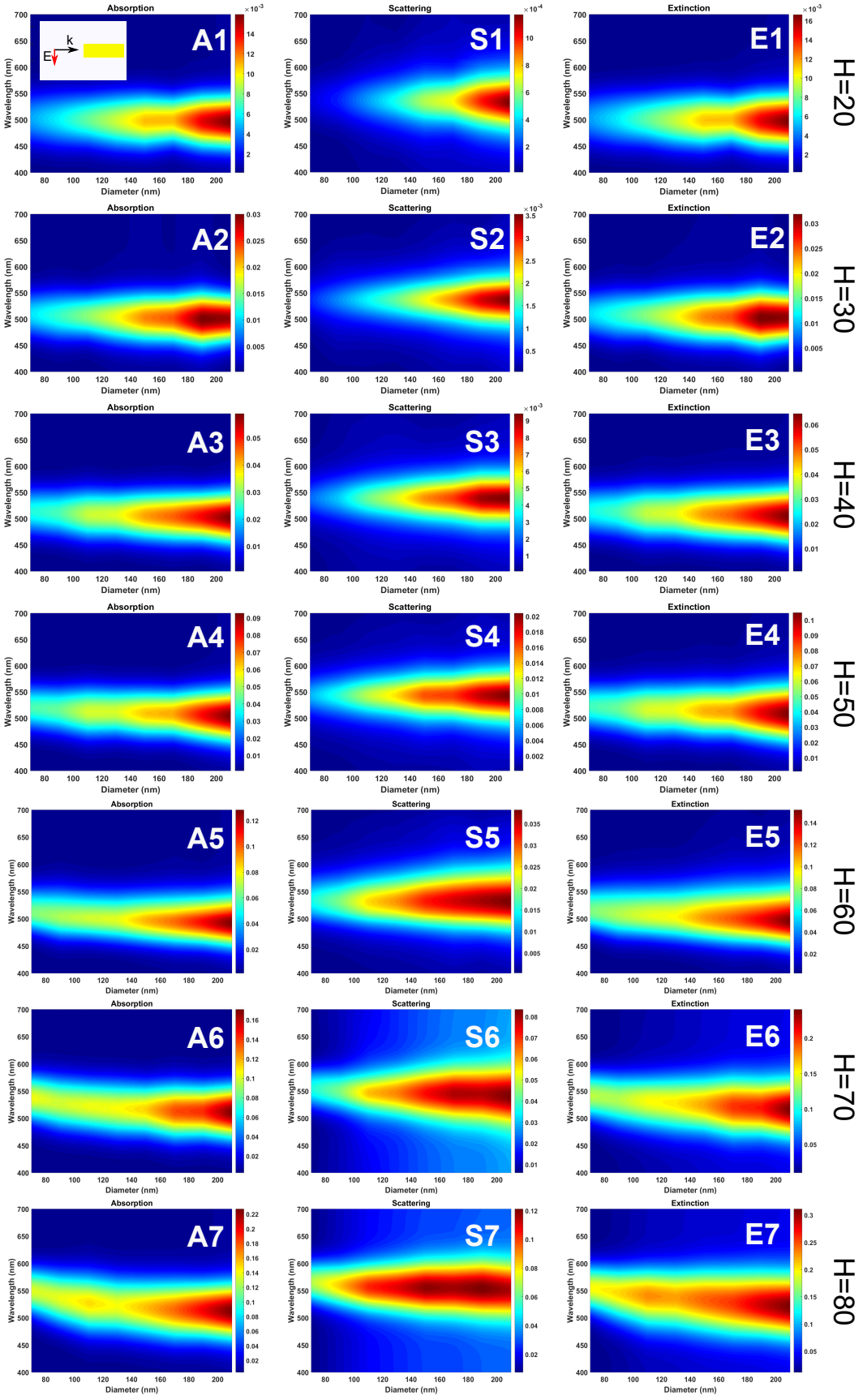

FIGURE 2.8: Calculated absorption, scattering and extinction spectra map of GNC for different heights depending on the diameters. H is the height in nm. Inset shows the illumination scheme. The surrounding medium is air.

This fact is important for the understanding of the possible control of the two dipolar modes (horizontal and vertical) separately by varying height and diameter.

One may observe strong spatial overlap between vertical and horizontal dipolar modes looking on the electric field maps (Fig. 2.9). This may play important role in the application based on the near field enhancement. Herein, we obtain a spectrally well separated and spatially overlapped plasmonic modes.

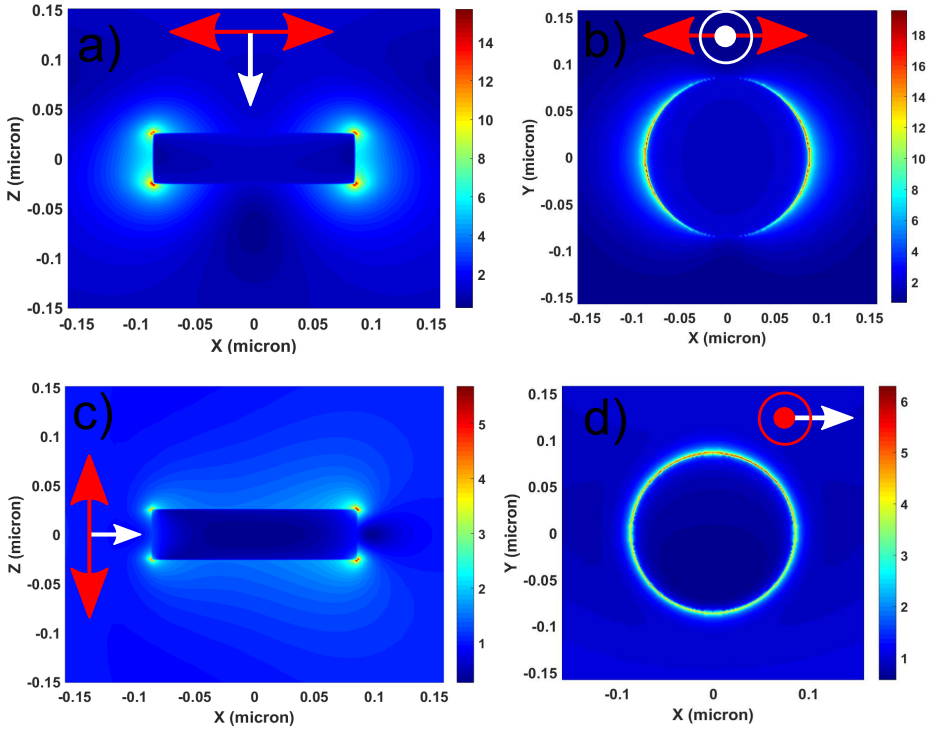

FIGURE 2.9: (a) Calculated electric field maps of 170 nm-diameter and 50 nm-height GNC for horizontal dipolar mode (a,b) and vertical dipolar mode (c,d) for XY and XZ planes. The red arrow or the circle-dot shows the polarization of the illumination. The white arrow or the circle-dot shows the wave vector of the illumination.

We have discussed the spectral specifications of the vertical and horizontal dipolar modes. The spatial disposition of the plasmons resonances is of great importance too. We show the electric field maps of the vertical and horizontal dipolar mode of 170 nm-diameter and 50 nm-height GNC in Fig. 2.9. Usually, the plasmonic modes like dipolar, quadrupolar or octupolar of a plasmonic system have different spatial confinement of electric field. Herein, the dipolar mode has two lobes in the opposite directions of the nanocylinder. The vertical mode has the confined field along all the edge of the nanocylinder.

In Fig. 2.10 we present the far-field polar plots for the horizontal and vertical mode of a GNC in air. A dipole moment induced inside a GNC by a x-polarized and a z-directed planewave, oscillates of the direction of the applied field and radiates along

the z direction (look Fig. 2.10a). Herein, we have an ideal dipole moment as the radiation is transverse to the polarization and the radiated power is identical for both directions. The Fig. 2.10b shows the far-field polar plot, when the verical dipolar mode is excited by a z-polarized plane wave directions.

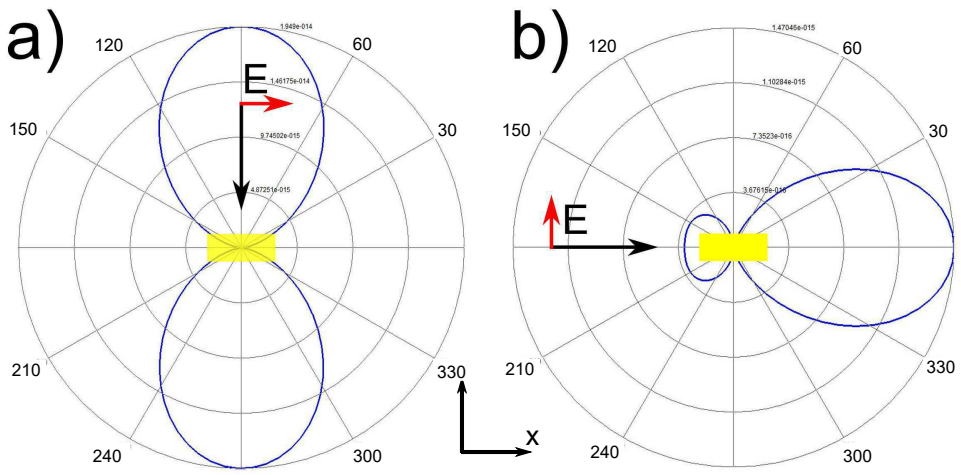

FIGURE 2.10: (a) Calculated far-field polar plot for 170 nm-diameter and 50 nm-height GNC of 170 nm-diameter and 50 nm-height GNC, when the horizontal dipolar mode excited at 630 nm, (b) and for vertical dipolar mode at 530 nm. The black arrow shows the wave vector and the red one is the electric field.

One may clearly see that the radiated power is not symmetrical for both directions, unlike the horizontal dipolar radiation. We assume this asymmetry is due to the phase variation of the electric field propagating inside the GNC. In other words, the incident electric field creates a phase variation along the diameter (170 nm), which is significant big compared to the illumination wavelengths.

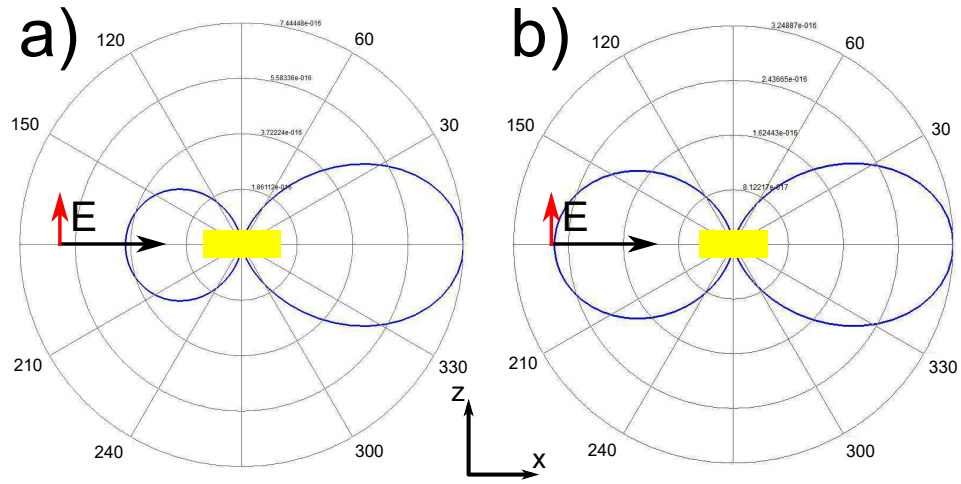

FIGURE 2.11: Calculated far-field polar plot for (a) 130 nm-diameter, (b) 90 nm-diameter and 50 nm-height GNCs, when the vertical dipolar mode excited. The black arrow shows the wave vector and the red one is the electric field.

On the other hand, the incident fiend exciting the horizontal dipolar mode creates a phase variation along the height (50 nm) of the GNC, which is small compared to the illumination wavelengths. In this case we can consider the electric field along the GNC uniform and the phase variation is not significant. Therefore the horizontal dipole mode radiation is symmetric in both

In order to prove that the asymmetric radiation of the vertical dipolar mode is due to the large diameter, we perform the far-field polar plot calculation for the GNC of 130 nm and 90 nm diameters shown respectively in the Fig. 2.11a and 2.11b. One can see that with the decrease of the diameter the two lobes of radiations become similar, what confirms our hypothesis.

2.4 Quadrupolar mode

LSPRs are relaxed by non-radiative (absorption) and radiative (scattering) losses. Also, these collective modes can be classified as "bright" or "dark" modes. Bright plasmon modes have finite dipolar moments and can therefore couple to the incident light. Since the bright modes couple to the light, they also radiate, and their spectral features can be broadened due to the radiative losses. In contrast, dark plasmon modes have zero dipole moments, and they are not broadened radiatively. The dominant damping mechanism for dark modes is the absorption, due to the imaginary part of the dielectric function of the metal. Hence, the dark plasmon modes are narrower than the bright plasmon modes. The even modes like quadrupolar, octopolar are considered as dark modes.

In this section we investigate the quadrupolar mode excitation and the peak position evaluation of gold nanocylinders depending on their diameter and height. Fig 2.12 presents the calculated absorption, scattering and extinction spectra maps of nanocylinders using an incident field and polarization parallel to the nanocylinders plane. The illumination scheme is shown on the inset of Fig. 2.12 map A1. By increasing the GNC diameter, the incident field couples with the quadrupolar mode due to phase variations inside the GNC along the illumination direction. Consequently, two distinct modes are observed. Though, on the scattering map (Fig. 2.12 map S1) we see clearly only one plasmonic mode (dipolar). It confirms that the quadrupolar mode is non-radiative mode since the mode is seen only on the absorption spectrum.

Another observation is that with the increase of the GNCs diameter the quadrupolar mode becomes prominent on the absorption map (Fig. 2.12 map A1), while the strength of the dipolar mode is decreased. It is important to note that the extinction spectrum shows both modes. Indeed, from an experimental point of view, the absorption measurements are much more complex to handle compared to the extinction ones.

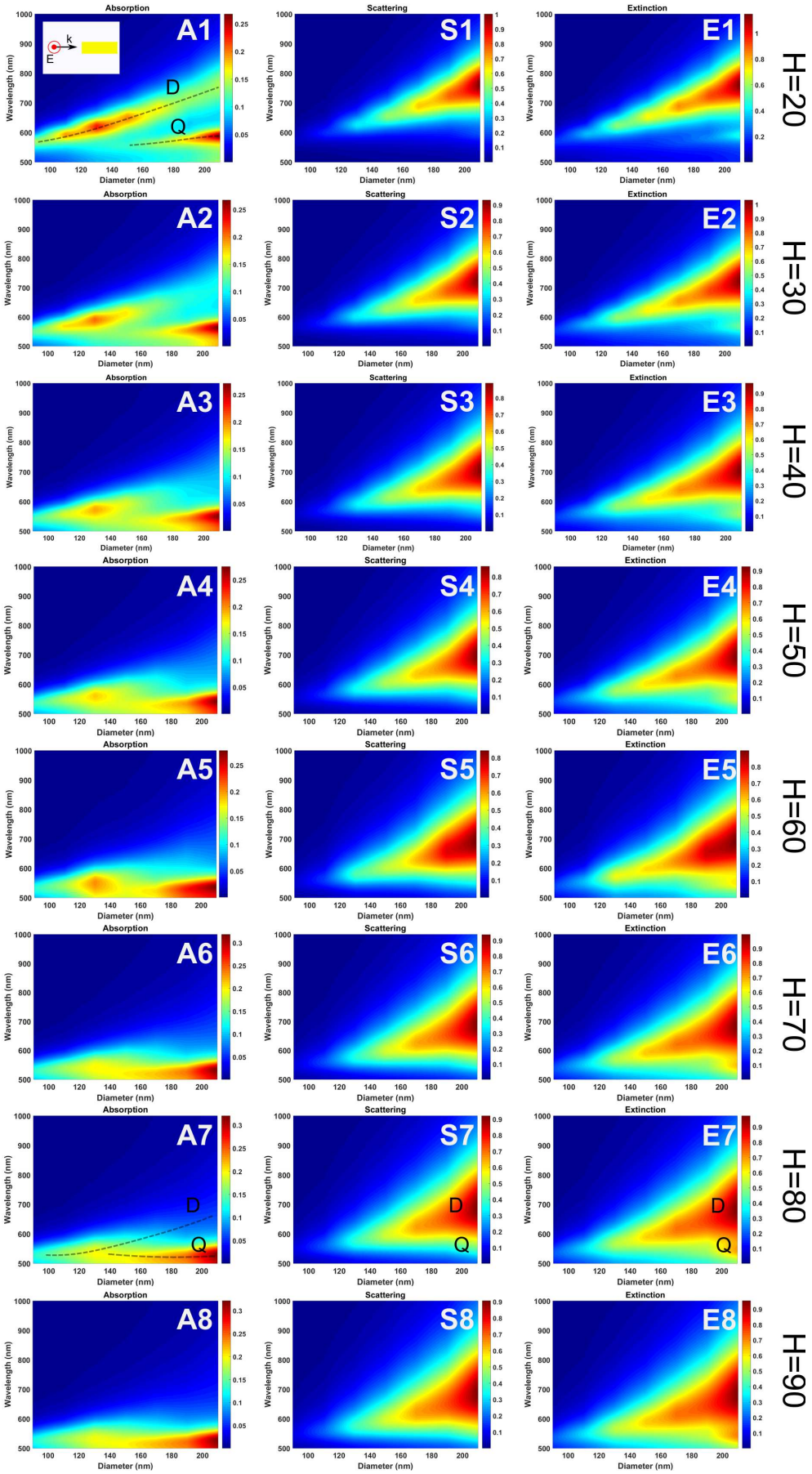

FIGURE 2.12: Calculated absorption, scattering and extinction spectra map of GNC for different diameters depending on the height. H is the heigth of GNCs. The surrounding medium is air. The illumination scheme is shown on the inset on the absorption map H=20

Looking to the absorption, scattering and extinction spectra maps for $H \geq 50$, one may see that the shift, related to the diameter increase, is minor for the quadrupolar mode comparing to the dipolar one. With the increase of the GNCs height, the strength of the non-radiative contribution (absorption maps) decreases for the dipolar mode, but it increases for the quadrupolar one. The combination of these two factors may lead to the wrong conclusions. For example, at the map A7 for the diameter more then 130 nm the dipolar mode shifts to the red and almost disappear, but it seems that the dipolar mode is blue-shifted. This conclusion has been done Coenen *et al.*, when the bigger GNC shows a blue shift of LSPR compared to the small one [70].

Indeed, the the quadrupolar mode becomes prominent for bigger GNC and the dipolar mode is not obvious anymore according to our studies.

We already have seen that the horizontal dipolar mode loses the resonant-kind behavior for the GNC D=150 nm and D=170 nm for the height more than 50 nm in the absorption maps (Fig. 2.6 map A6). Looking on the quadrupolar mode, on the extinction spectra maps (Fig 2.12) one may notice that with increase of the height of GNCs the quadrupolar mode becomes more evident and stronger unlike the horizontal dipolar mode. To sum up, the increase of the GNC height augments the strength of quadrupolar mode and diminishes the strength of the dipolar mode.

2.5 Shape Influence on LSPRs

In the previous section we discussed the size effects on the plasmonic mode peak positions and their properties. In this section we are going to study, the shape effect on the plasmonic resonances. Already in Chapter 1 we have mentioned one of the pioneering works reported on the shape effect on the LSPRs (Fig. 1.8b).

In Fig. 2.13a we show the calculated extinction spectra for gold nanoparticles of different shapes. We choose the shapes of a Triangular prism, Sphere, Truncated cone (T-cone), Cylinder, Cube, Cuboid and Pyramid. The electric field is oriented along diameter of the sphere, the base of the pyramid or along the arm of the triangular prism. The size of each structure along the electric field oscillation is equal to 100 nm. This dimension is called plasmon length. Previously Ringe et al. studied the optical response of the cubes, decahedra, icosahedra, triangles, octahedra and defined the plasmon length as an universal parameter to predicts LSPR resonances. They concluded that the nano-structures of different shape having same plasmon length show similar LSPR spectra [71].

Nevertheless, one may note that the NPs with electron oscillations across the same distance have different dipolar mode peaks (Fig. 2.13a). Surely, the sphere and the cube have different height then other NPs presented on the Fig. 2.13a. However, the NPs of

the same height show important shifts of peak positions also. For example, difference between the peaks of a triangle and a rectangle is around 65 nm. The dramatic shift of the peak position to 640 nm and the small peak appearance around 565 nm of the Pyramid is discussed in the Chapter 5.

One can assume that these LSPR peak shifts are based on the different volume of each NP. In order to check the correctness of this assumption we calculate the extinction spectra of the gold NPs of previously studied shapes of the same volume (Fig. 2.13b). Herein, we clearly see that the NPs of the same volume show approximately the same dynamics of LSPR shifts depending on the shape as for Fig. 2.13a.

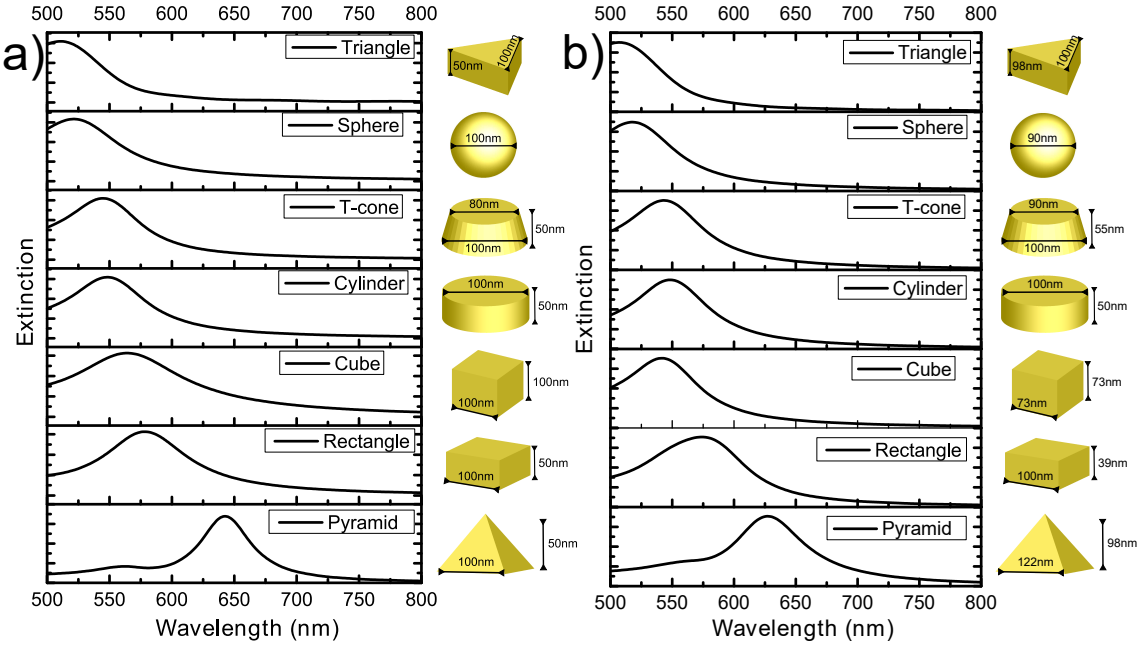

FIGURE 2.13: (a) Calculated extinction spectra of different shape gold nanoparticles. The distance along the polarization (electric field is kept constant (100 nm). And the height is 50 nm besides the cube and the sphere. (b) Calculated extinction spectra of different shape gold nanoparticles, when their volumes are equal.

For example, the peak difference of the extinction spectrum of the triangular prism and the cuboid is around 65nm as for extinction spectra on the Fig. 2.13a. The main difference on the dynamics of the peak position changes between Fig. 2.13a and 2.13b are the peaks of cubes. The Cube spectrum on the Fig. 2.13b is blue-shifted compared to the cylinder, while on the Fig. 2.13a the Cube spectrum is red-shifted. It can be explained by the difference between the Cylinder diameter (100 nm) and the facet length of the cube (73 nm).

As a conclusion, we would declare that despite of the use of the same amount of the material or the same unidirectional size (Fig. 2.13a), spectra show dramatic changes of LSPR position depending on the shape of the NPs. We show that a LSPR peak shifts in air for different shapes. Indeed, the increase of the surface (size) of NP may

record a blue-shift of LSPR or red-shift depending on the shape. For example, the triangle prism LSPR (Fig.2.13b) is blue-shifted compared to the pyramid LSPR on Fig. 2.13a, while the triangle prism has larger surface than the pyramid. In contrary, if we compare two cubes of different sizes, the cube with larger surface records red-shift of LSPR compared to small surface. This shape-size control of LSPR open wide options to obtain a desired LSPR peak position for the demanded surface (size).

2.6 Conclusion

The asymmetric nanoparticles like nanocylinders, besides dipolar and multipolar modes may sustain out-of-plane (vertical) dipolar mode depending on the illumination conditions. The near field confinement of these two dipolar modes is similar around nanocylinder, while spectrally they are well separated. These two mode can be potentially used in various applications. In contrast to the near-field similarities, their far-fields radiation patterns differ dramatically. Indeed, the phase variation inside a GNC can change the far-field radiation.

We demonstrated the "dark" nature of quadrupolar modes using FDTD simulations. Moreover we showed the importance of the shape on the LSPR control. Finally, we discussed and explained the effect of height-diameter ratios on the LSPR of GNCs. In summery, we showed the ways of tuning of LSPRs and their in-situ (near-field) and ext-situ (far-field) nature.

"In order for the light to shine so brightly, the darkness must be present."

Francis Bacon

3

Characterization set-up influence on optical spectra

3.1 Introduction

Nanospectroscopy simply addresses the spectroscopy of nanoscaled structures. With the huge increase of the interest in optical properties of nano-objects, multiple optical techniques have been developed for the characterization of the single nano-object. Zsigmondy *et al.* developed a dark-field immersion microscope in order to observe single nano-objects in a liquid [72]. For decades, dark field (DF) microscopy has been used to study the optical properties of metallic nanoparticles [73–77]. A DF microscope coupled with a high sensitive CCD camera and a spectrometer may measure scattering spectrum of the single nano-object revealing the LSPRs [74]. One of the first spectroscopic studies of a single metallic particle was reported by Mock et al. and Schultz et al. [36, 78]. They performed Rayleigh scattering measurements of the single silver nanoparticles to determine how the frequency of the LSPR depends on size and shape. A decade after, Fan et al. and Knight et al. showed how sensitivity of DF scattering technique depends on the excitation and the collection geometry [79, 80].

Fig. 3.1a shows the experimentally obtained DF scattering spectra for the same illumination geometry, but different collection numerical aperture[80]. Also, it is shown polarization influence on the DF spectra.

Fan et al. showed the impact of the incidence angle on the DF scattering spectra of a gold heptamer nano-cluster [79].

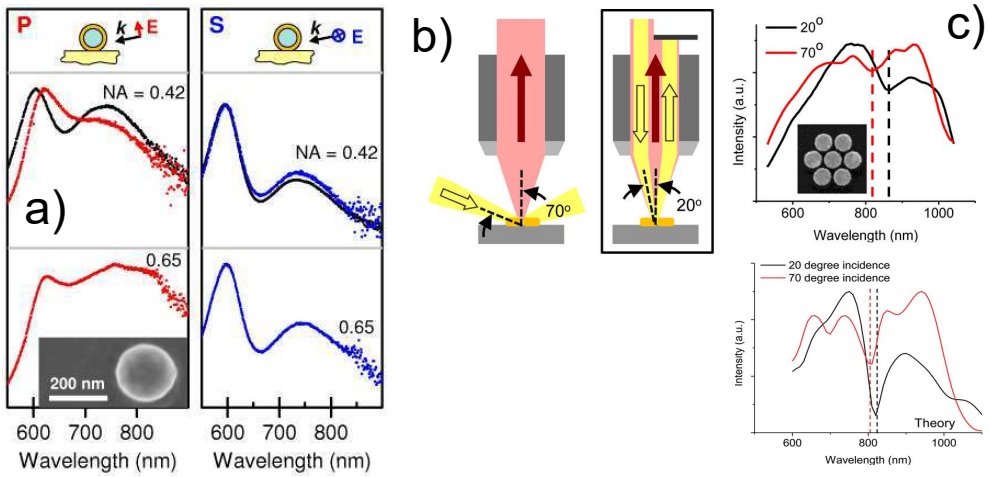

FIGURE 3.1: (a) Experimental DF scattering spectra for a silica-gold nanoshell showing scattering spectra for P-polarized and S-polarized incident light for two different objectives (NA = 0.42 and 0.65) when the excitation angle is 12 degrees relative to the substrate. Spectra for an excitation angle of 35 degrees are shown for a collection NA = 0.42 (black curves). The silica-core radii is 62 nm, and the gold-shell radii is 95 nm. The substrate is ZnSe, which refractive index varies from 2.55 to 2.8 in the visible range. Inset shows an image of the nanoparticle taken with help of scanning electron microscope. (b) Schema of near to normal and high angle Dark-field illumination. (c) Spectra of an individual lithographically defined plasmonic heptamer. Experimental s-polarized spectra of a gold heptamer measured for two different incident angles of illumination (20 and 70 degrees). The inset shows an SEM image of the nanostructure; the average disk diameter and interparticle gap distance are 144 nm and 15 nm, respectively. The substrate is ZnSe. Theoretical scattering spectra of the same structure below.

The schemes for excitation/collection and DF spectra are shown respectively in Fig 3.1b and 3.1c. They reported that the near-normal incidence illumination provides significantly higher signal-to-background ratios compared to the high incidence angle of illumination. In these two examples structures of complex organizations and substrates with high refractive index were used, which may increase the strength of the coupling between plasmonic modes or result in the multi-mode excitation depending on the excitation angle and polarization. Therefore, these modes may exhibit non-simple far-field radiation patterns which explains these changes in DF spectra for different collection and illumination geometries.

In this chapter we analyze the experimental factors that may cause the optical response changes in the DF scattering of a simple gold nanocylinder. Firstly, we describe the nanofabrication and optical characterization methods. We show an experimental and numerical comparative study of a single gold nano-cylinder (GNC) and of an ensemble of gold nano-cylinders. Finally, we discuss the influence of the pitch array on

the LSPR recorded by the extinction spectroscopy then draw some conclusions about the optimal inter-particle distance.

3.2 Nanofabrication

Electron beam lithography (EBL) is one of the most popular techniques for nanofabrication. In short, it involves the exposure by a highly focused electron beam of a resist. The solubility of the exposed resist is dramatically modified (brake the polymer chain of Polymethylmethacrylate into small fragments) and it allows the selective dissolution of exposed area. We will follow the steps of EBL process given in figure 3.2.

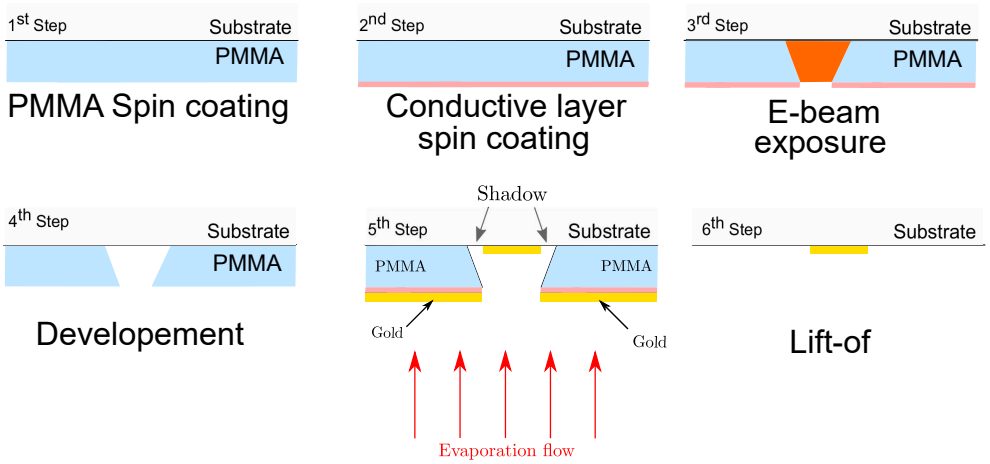

FIGURE 3.2: Illustration of the steps of electron beam fabrication technique

1^{st} Step

At first, we deposit a thin layer of PMMA (Polymethylmethacrylate) resist on a clean glass coverslip. The resist plays a role of a mask, that we design for EBL process. We use a spin coater to apply the resist to the sample. During the spin coating process the sample is held in place by vacuum suction. The resist is drop-casted on the glass coverslip by a pipette and set to spin at certain speeds (table 3.1). We obtain a layer (160 nm thick) of E-beam resist (PMMA) with molecular weight of 950kDa (kilodaltons) diluted in MIBK (Methyl-Iso-Butyl-Ketone).

2^{nd} Step

This step includes a deposition of a layer (40 nm thick) of a conductive polymer, which is necessary to prevent the charge accumulation during the E-beam exposure. After the spin coating, the sample is baked in an oven at 160°C for 3 hours for homogeneous hardening of PMMA.

TABLE 3.1: Recipe for Spin coating a layer of PMMA and a layer of conductive polymer

Step	PMMA layer			Conductive polymer layer		
	Time (s)	Acceleration (rpm/s)	Speed (rpm)	Time (s)	Acceleration (rpm/s)	Speed (rpm)
	60	3000	4000	30	3000	4000

3^{rd} Step

The exposure of the polymer is done with help of the electron beam microscope e-Line from "Raith". After the alignment process, which includes the adjustment of electron beam focus and astigmatism, the designed patterns are reproduced on the resist. The exposure is performed by 20kV high voltage electron beam and 450 μ C/cm^2 exposure dose.

4^{th} Step

The conductive polymer is washed out by immersing in a water for some seconds. The resist is typically immersed in a liquid developer to dissolve the area that was exposed to e-beam. The sample is dipped in a mixture of MIBK/IPA (1:3 ratio) for 60 seconds and in the stopper (IPA) for 15 seconds at the room temperature 18-22 °C. The development is terminated by a blow-dry with air gun.

5^{th} Step

We use evaporation as a method to deposit a metallic (gold or silver) layer to the substrate. The evaporation is managed in the evaporator MEB400 from Plassys. Some metals like gold do not stick well to the SiO_2 substrate, that is why an intermediate adhesion layer of chromium, titanium dioxide or nickel is required. Hence, $3nm$ of TiO_2 layer is deposited by e-beam evaporation. This technique is preferred for materials having very high melting temperature, as it is for titanium dioxide (1843 °C). Indeed, the thermal evaporation of the TiO_2 needs very high current which is not advised. $50nm$ of Au or Ag are deposited by thermal evaporation thereafter. The deposition of the metal layer is done using thermal method due to good controllability of the evaporated thickness of a metal using this method as compared to e-beam evaporation. Whole procedure was done in the same chamber without venting, where pressure was lower than $1 \times 10^{-6} mbar$, with evaporation rate of $0.1 nm/s$.

6^{th} Step

The last step is to finalize the designed pattern after the deposition of the metal. On the areas exposed by the electron beam the deposited metal sticks to the substrate, while on the unexposed areas the metal covers the resist surface (PMMA). After the metal deposition, the remaining (unexposed) resist is dissolved in acetone (lift-off) for approximately 4 hours, thereafter we rinse (wash) the sample by IPA and blew-dried. The metal covering the resist loses "footing" and so only the metal sticking to the substrate remains.

3.3 Optical characterization

3.3.1 Dark-field spectroscopy

A single nanoparticle optical characterization is carried out with the help of a commercial DF scattering microscope from Zeiss (Axio Imager Z2). It allows to collect scattered light in reflection and transmission geometry. The schematic of the DF scattering setup for the collection in reflection geometry is drawn in Fig. 3.3a. The light illumination and the collection are carried out by the same 50x objective. The light source is a halogen lamp with a broad-band spectrum in the visible-IR range. The illumination numerical aperture of the objective is between 0.8 and 0.95, which corresponds to a range of angles of 53,1 - 71,8 degrees. The collection numerical aperture is 0.8 (from 0 to 53 degrees). In this manner we do not collect back or forward reflected light, we collect only the scattered light coming from the sample. The DF illumination profile is shown in the Fig 3.3b. In order to obtain an experimental dark-field reflection scattering spectrum of a single nanoparticle, we record three different signals: S_{GNC} is the signal recorded on a nanoparticle, S_{BG} is the background signal recorded on the glass substrate and S_0 corresponds to the lamp spectrum. The final scattering spectrum is obtained by:

$$\frac{S_{GNC} - S_{GB}}{S_0}. \tag{3.1}$$

For dark-field transmission measurements, the illumination is performed with a help of an oil immersion dark field condenser, which has 1.2-1.4 numerical aperture. The particle is excited by a total internal reflection, it means by an evanescent wave (3.3c). So, we will collect only the scattered light avoiding any transmitted light from the sample by the objective placed above the sample. As the signal is sent to the spectrometer through a multimode fiber, the diameter of the collection area can be calculated by the following equation:

$$D_{collect} = \frac{D_{fiber} \cdot f_{tube}}{M \cdot f_{lens}}, \tag{3.2}$$

where, D_{Fiber} is the diameter of the fiber core, f_{tube} is the focal length of the tube lens of microscope, M is the magnification of the objective and f_{lens} is the focal length of the lens which focuses the light to the fiber. We can control the diameter of the collection area on the substrate by changing the fiber core size or the coupling lens (focal length).

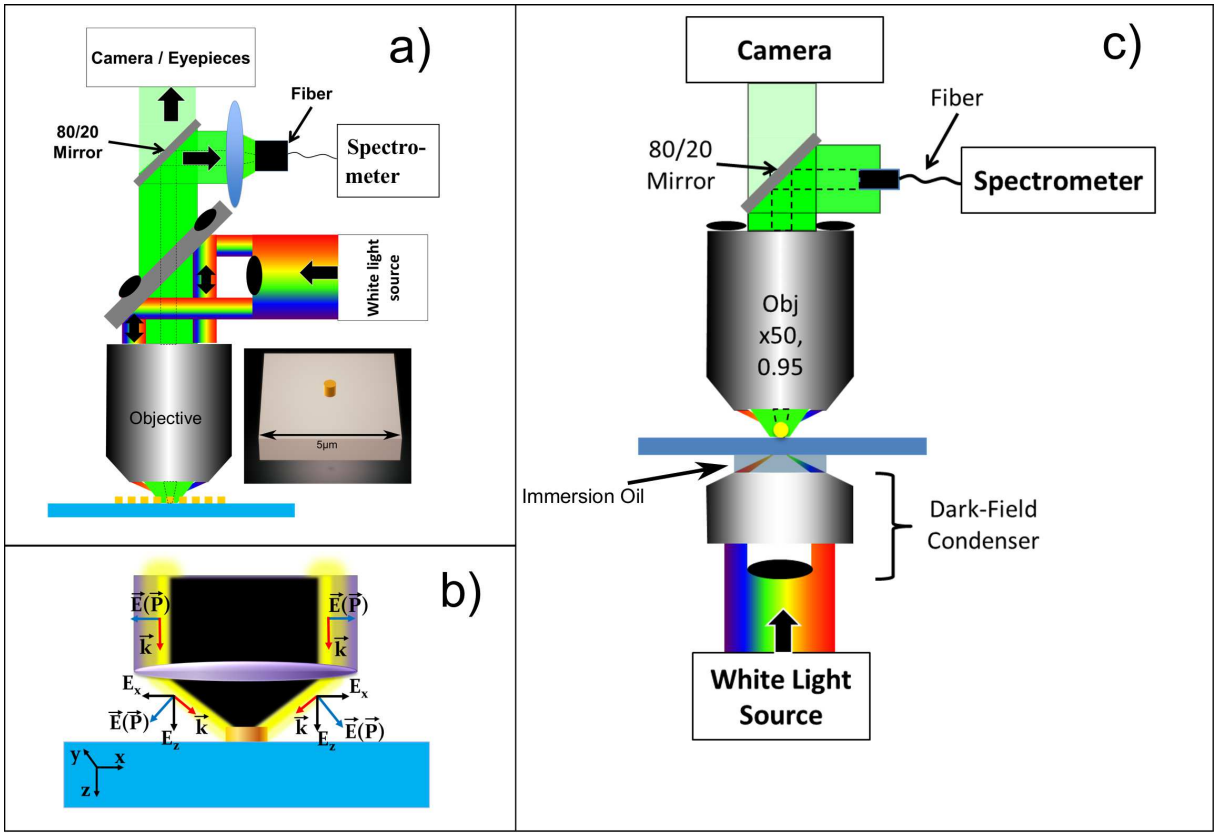

FIGURE 3.3: (a) Dark field reflection scattering setup schematic: a centrally blocked and linearly polarized beam is focused through the 50X dark field objective. The collected light is filtered confocally using an optical fiber coupled to a lens. The fiber has a 50 μm core size and the collection zone corresponds to 3 μm on the substrate. It is connected to the spectrometer Ocean Optics QE65000. (b) Scheme of the dark-field illumination beam profile: yellow-impinging light, black-collection, k - wave vector, E - electric field, Ex and Ez- components of electric field, P - Polarization. (c) Dark field reflection transmission setup schematic: linearly polarized beam is focused through an oil immersion dark field condenser which allows to excite an evanescent field on the glass substrate. Therefore, the nanoparticles are excited by that field.

3.3.2 Extinction spectroscopy

The optical extinction spectra of ensembles of nanoparticles are carried out with the help of a homemade setup illustrated in Fig 3.4. We use a broad band white light source in Vis-IR range. A collimated light is focused on the sample by an objective

(50x, 0.28), and the second objective collects the transmitted light. These objectives present a long working distance ($\simeq$ 30 mm) allowing the rotation of the sample in front of the objectives. A polarizer placed before the illumination objective allow to control linearly the polarization. The transmitted light is divided in two parts by a 50/50 mirror in order to have a signal on the spectrometer and an image on the camera as well. A lens focuses the transmitted light from the mirror on a fiber. As previously the fiber is used for controlling the size of the collection area. Therefore, the fiber transfers the signal to a spectrometer. The extinction spectrum is obtained by using the following formula:

$$1 - \frac{T}{T_0}, \tag{3.3}$$

where T is the transmitted light measured on the structure and T_0 is the transmitted light measured on the substrate without structures.

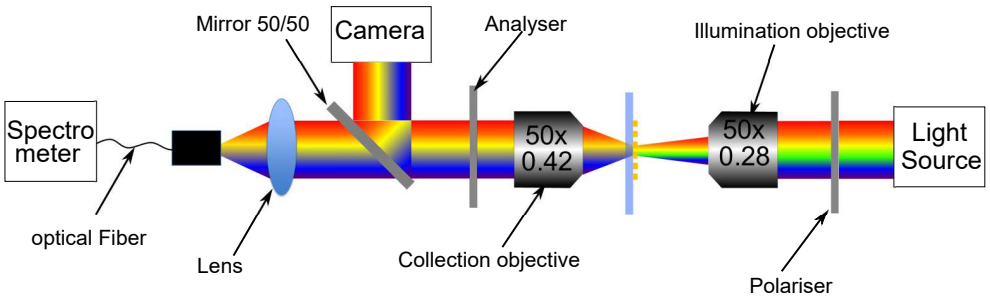

FIGURE 3.4: (a) Extinction setup schematic: a linearly polarized beam is focused through the 50X long focal distance objective. The light is collected with help of a 50X long focal distance objective. Hence, the collected light is filtered confocally using an optical fiber coupled to a lens. The fiber has a 200 μm core size and the diameter of collection zone corresponds to 8 μm on the substrate. It is connected to the spectrometer Ocean Optics QE65000.

3.4 Single nano-object optical characterization

3.4.1 Lamp spectrum for DF illumination

As it is shown in eq. 3.1 we need to normalize initial recorded spectrum with the lamp spectrum with the aim of obtaining a DF spectrum. The lamp spectrum for DF reflection spectroscopy can be recorded using a mirror or using a direct measurement (putting the source in front of a spectrometer). In the latter case, the optical components of microscope such as lenses and mirrors may change the lamp spectrum. Hence, we use a mirror in order to record the spectrum of the lamp for the reflection geometry. The DF illumination in the vicinity of the substrate contains high angles (53-71 degrees) of wave vectors and the light is not reflected to the collection of the objective due to its configuration. Furthermore, the mirrors do not have diffuse reflection, then we use a

bright mode illumination. The bright mode illumination does not use a blocked beam and the reflected light propagate to the collection of the objective. In Fig. 3.5a we show a DF spectrum of a single gold nanocylinder normalized by the lamp spectrum taken by a mirror. The corresponding simulation is depicted on the 3.5d and one may confirm a significant mismatch between experimental spectrum and the calculated one. The experimental curve shows a peak position place at 640 nm with a FWHM (full width half maximum) of 263 nm, while the simulated curve shows a peak position at 746 nm with a FWHM of 213 nm. Indeed, all the wavelengths of the lamp are not distributed homogeneously across the illumination beam profile. The DF illumination has a different spectrum from the bright field illumination because of a centrally blocked beam (3.5c).

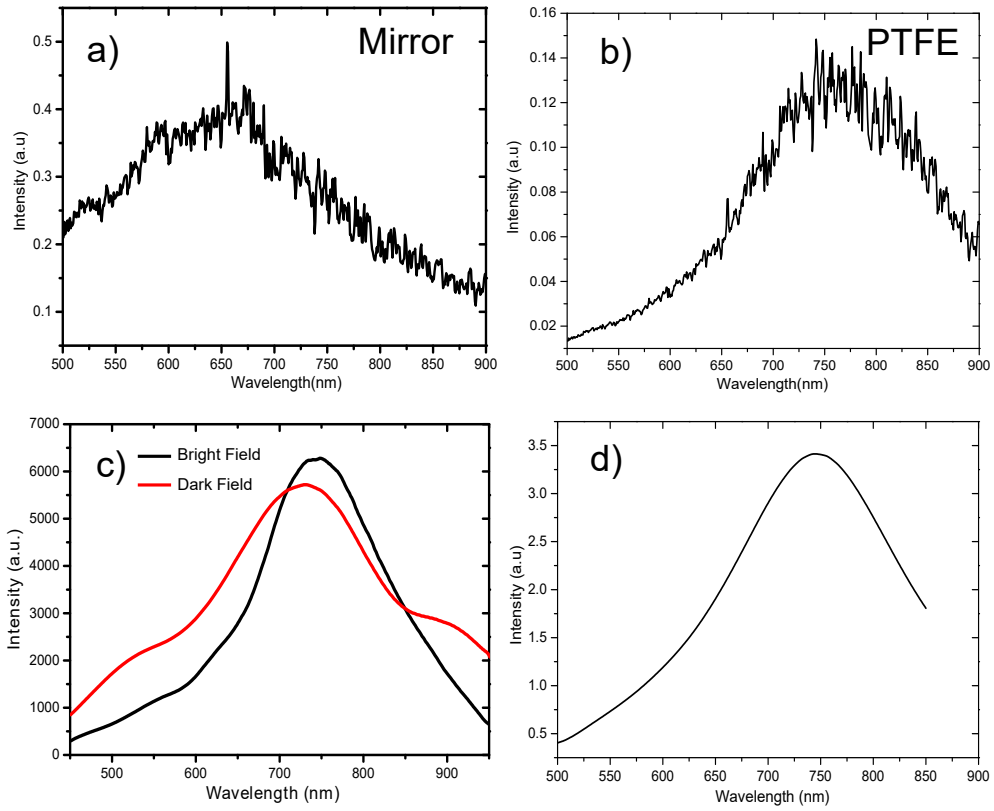

FIGURE 3.5: (a) DF reflection scattering spectrum of a nanocylinder of 170 nm diameter. The DF spectrum is normalized by the lamp spectrum taken by a mirror, (b) The DF spectrum is normalized by the lamp spectrum taken by a PTFE substrate. (c) Lamp spectrum taken with help of the mirror (black curve) and with help of PTFE substrate (red curve). (d) Numerically simulated DF reflection scattering spectrum for a GNC of diameter of 170 nm

We record the lamp spectrum of DF illumination by using a rough PTFE (polytetrafluoroethylene) substrate, as the PTFE has a uniform diffuse reflectance in visible-near infrared range [81]. The DF objective illuminates the PTFE substrate and records

the diffuse reflected light (3.5c). So, in this manner we retrieve the normalization spectrum S_0 and the normalized DF reflection spectrum is shown in Fig 3.5b. One may see a sufficient agreement between the experimental and simulated spectra. The scheme of the reflections of mirror and PTFE are shown in Fig. 3.6.

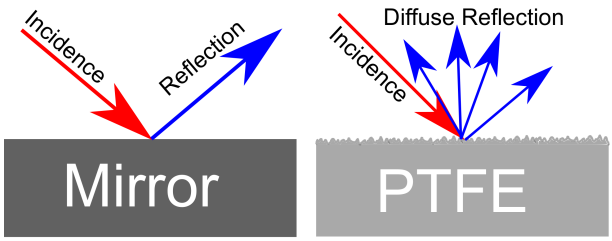

FIGURE 3.6: Illustration of the reflectance of the mirror and the PTFE. When the impinging light reach to the mirror it is forward reflected or back reflected the same angle of the incidence, While the PTFE reflects the light for different angles due to rough surface.

3.4.2 DF illumination FDTD modelization issues

A commercial DF microscope uses a multi angle illumination. For example, in our case it is from 53 to 72 degrees. Also, the DF illumination contains in-plane and out-of-plane polarizations after the objective light focusing on a sample. The scheme of the polarization features before and after the focusing of the beam is shown in Fig. 3.7.

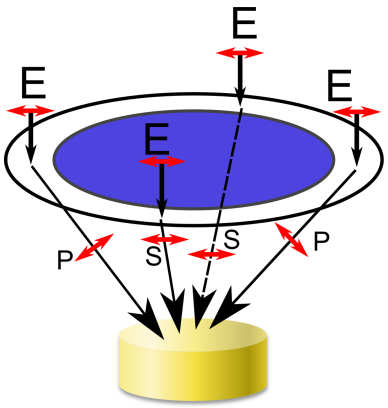

FIGURE 3.7: Schematic for the polarization feature of the optical beam as focused onto the sample through a DF objective coupled with a beam-blocker. The beam is polarized linearly before the focusing lens. After focusing the beam is declined by a certain angle and on the focus some wave-vectors have pure in-plane (parallel to the nanocylinder plane) polarization (S-polarization), others have a polarization with in-plane and out-of-plane components of the electric field (P-polarization).

In order to achieve a proper numerical simulation of a dark-field scattering spectrum we need to combine results of many simulations, for each illumination angle and for each polarization. In this manner we increase greatly the calculation time by doing many calculations instead of one.

However, even the use of a single angle illumination itself increases the calculation time in comparison to the calculation for the normal incidence illumination. The table below shows a relation between calculated angle and the calculation time (zero degree is corresponding to the normal incidence):

Angle (Degrees)	0	30	50	60	70
Simulation time	1x	2.0x	4.3x	7.5x	16.6x

Lumerical (FDTD solutions) always uses a broadband pulse. The example of such source wavelength range definition is shown in Fig. 3.8a. A plane wave source injects fields that have a constant in-plane wavevector for all frequencies. The Fig. 3.8b shows a source with an injection angle of approximately 50 degrees (black arrow). Since, the magnitude of the wavevector is proportional to frequency, the actual injection angle changes as a function of frequency. The FDTD software choses the in-plane wave vector (dotted green line) allowing the actual injection angle at the main frequency f_{center} to match the center injection angle. Higher frequencies are injected at smaller angles, while lower frequencies are injected at larger angles. The k_x is calculated with the following formula

$$k_x = k_{center} sin(\theta), \quad k_{center} = n\frac{2\pi f_{center}}{c}, \tag{3.4}$$

where, θ is defined as the injection angle, f_{center} is the center frequency of the source, n is the refractive index and c is the speed of light. So, when we use an angle illumination, the angles are changed for each frequency to match the wavevector to the fixed in-plane wavevector k_x. For a frequency “f" the relation between wavevector and in-plane fixed k_x is:

$$k(f) = \frac{k_x}{sin\theta(f)}, \quad k(f) = n\frac{2\pi f}{c} \tag{3.5}$$

In order to satisfy this relation for each frequency the $\theta(f)$ is changed each time. In Fig 3.8c is shown the dependence of wavelength on the actual illumination angle. Only for the central wavelength the result corresponds to the defined angle. In order to draw a spectrum for angle illumination we do many separate calculations for each wavelength by defining fixed angle as a central. Each calculation gives a value of the scattering intensity for a single wavelength. For example, we achieve a DF spectrum by doing 70 calculations at 55 degrees illumination and 70 calculations at 65 degrees. Note, this is for only one polarization. The final DF spectrum is the sum of the spectra of two polarizations and needs around 300 simulations.
Indeed, considering all these factors the modeling of DF illumination by a FDTD method demands enormous computational resourses and time.

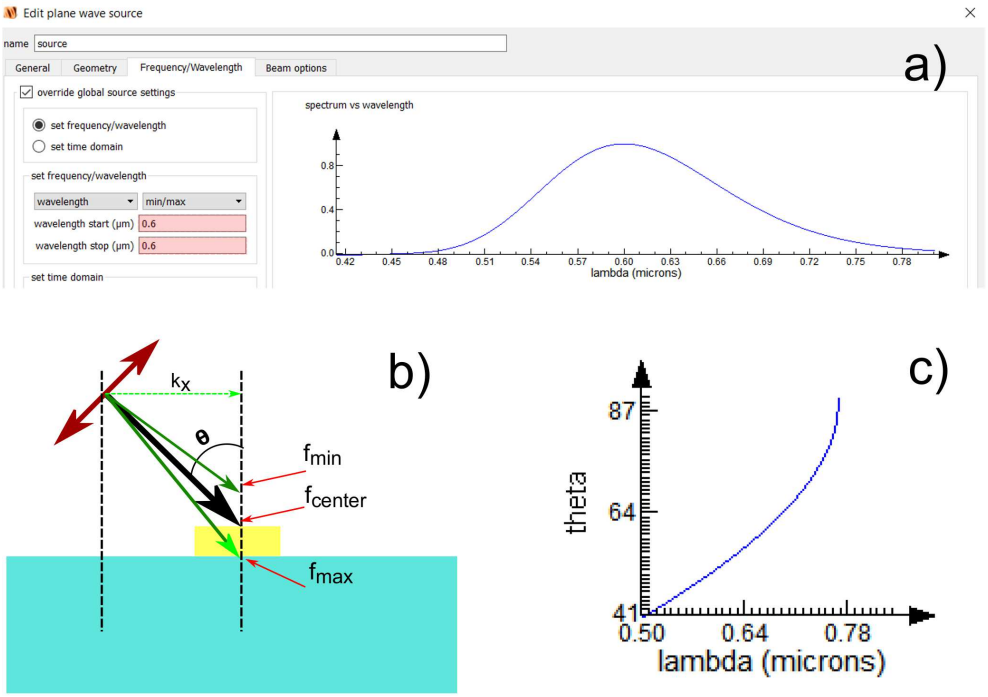

FIGURE 3.8: (a) Planewave source spectrum, when the central wavelength is 600 nm (extracted from software Lumerical FDTD). (b)Schematic of the angle illumination in FDTD. The black arrow shows the wavevector for central frequency of the illumination spectrum. The green arrows show the wavevectors for the minimum and maximum frequencies of the illumination spectrum. The green dash-lined arrow shows the in-plane component of wavevectors. The red arrow shows the direction of electric field (polarization). (c) Relation between the actual illumination angle and the wavelength, when the central wavelength is fixed at 55 degree, and the spectrum range is from 500-850 nm

3.4.3 Spatial filtering impact

Reflection geometry

To allow the detection of the scattering signal coming from a single nanoparticle, we use a spatial filter achieved using a fiber. The collection zone diameter in our setup is given by the fiber core diameter and focal distance of the lens. To understand the impact of the collection area, we use two different fibers: one with a of 50 μm core size coupled to a lens with a focal length of 5 cm and another one with a 10 μm core size coupled to a lens with a focal length of 3 cm. The collection area corresponding to these couples are equal to 5 μm and 1μm collection zone respectively.

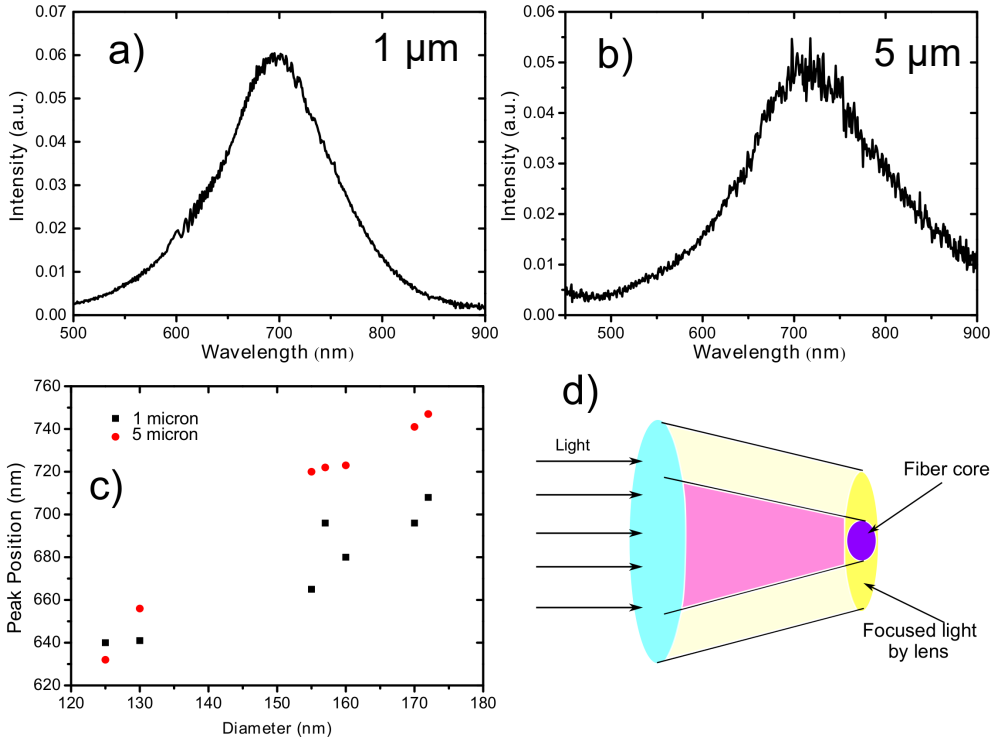

FIGURE 3.9: (a) DF reflection scattering spectrum of a nanocylinder of 157 nm diameter, when the collection zone diameter on the substrate is $1\mu m$ (b) and $5\mu m$. (c) Histogram of peak positions for different GNC depending on the collection zone diameter. (d) Schematic of the spatial filtering by a fiber

In the Fig 3.9a and 3.9b are presented the DF reflection scattering spectra of a gold nanocylinder for a collection zone corresponding respectively to $1\mu m$ and $5\mu m$. One may notice that even if the noise is reduced with the smallest collection area, we observe difference between these spectra. Indeed, the peak positions and the widths are not similar. Herein, the difference is explained by two effects. Firstly, by increasing the collection zone we decrease the signal to noise ratio as we collect more scattered light from the substrate. Moreover, $1\mu m$ collection zone may not be enough to collect all light scattered by the nanoparticle especially for big ones. The second effect depends on the numerical aperture of the fiber coupled to a lens. We used a lenses presenting a 0.24 NA and 0.38 whereas the $50\mu m$ core fiber and the $1\mu m$ core fiber present NA of 0.22 and 0.1 respectively. With this mismatch some wave vectors can be filtered. The Fig 3.9d shows a schematic when the fiber and the lens have the same numerical aperture. Below it is shown the table of the collection area depending on the chosen lens and fiber.

The beam focused on a fiber contains all light collected by the objective. The fiber filters only spatially if the numerical aperture of the fiber is bigger than the focusing lens (without k-space). In our case the numerical aperture of 10 μm fiber is 0.1 (collection area of $1\mu m$) and the lens has 0.38, therefore we achieve both k-space and a spatial

Collection area	Fiber core diameter	Fiber NA	Lens focal distance	Lens NA
5 μm	50 μm	0.22	5 cm	0.24
1 μm	10 μm	0.1	3 cm	0.38

TABLE 3.2: Spatial filtering parameters depending on the optical set-up compounds

filtering.

For the 50 μm fiber the numerical aperture is 0.22 and for the lens it is 0.24. Herein, the k-space filtering is less and we depict on the spectrum almost all wave vectors contributions collected by the objective. The Fig 3.9c shows a histogram of the dipolar mode peak positions of different diameters nanocylinders for 1μm and 5μm collection zones. In the majority of the cases the peak positions for 5μm are red-shifted respected to the 1μm, where the k-space filtering and the nanocylinders radiation patterns may play a role. In Chapter 4 we discuss further the effect of filtering on the collected signal.

Transmission geometry

We perform the same comparative study for collection areas of 1μm or 5μm using the DF transmission scattering spectroscopy. Note, the fibers and the lenses are chosen the same as for DF reflection scattering spectroscopy. In the Fig 3.10a and 3.10b are shown the spectra of a gold nanocylinder for the collection of 1μm and 5μm respectively.

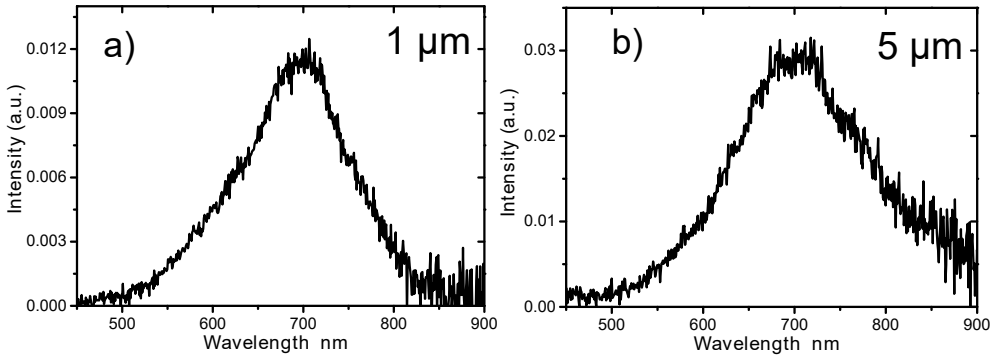

FIGURE 3.10: (a) DF transmission scattering spectrum of a gold nanocylinder of the diameter of 157 nm, when the collection zone is 1μm and, (b) when it is 5μm

The spectrum on the Fig 3.10a shows a peak position at 696 nm and the width is 163 nm. If we compare it with the peak position of DF reflection scattering spectrum (Fig 3.9a) the peak positions are the same, however the widths are different (163 nm versus 132 nm). The spectrum on the Fig 3.10b shows a peak position at 708 nm and the width is 188 nm. Herein, we see a difference on the peak positions in comparison

with DF reflection geometry, although widths are very close. As for reflection, the DF transmission scattering spectra show various features for different diameters of collection zones as well. One may notice that there is a difference between DF reflection and transmission spectra peak positions for the same collection zone. The further discussion and explanation of the difference between the DF reflection and transmission scattering spectra will be drawn in the Chapter 5.

3.5 Single nanoparticle optical characterization using the ensemble measurements

One of the simple methods for the optical characterization of nano-objects is the extinction spectroscopy (ES). In that case, the transmitted light is directly recorded and the ratio between the recorded and the illumination reference signal gives the extinction value. Although this method is easy to implement, it is not suitable for single NPs due to the very small difference between the recorded signal of single nanostructure and the reference signal. Therefore, one solution is to measure the extinction spectrum of a NPs ensemble in order to increase the signal-to-noise ratio. Nonetheless, there is a general conception for the 2D pitched arrays that the LSPR of metallic NP patterns is different from that of a single NP. The coupling between the LSPR of NPs and diffraction orders of the array may result in a visible change of the spectrum. However, the use of ES excludes many problematics of DF spectroscopy discussed previously. Fig. 3.11 presents the extinction spectra of various arrays with periods from 400 nm to 1000 nm for different nanocylinder diameters from 135 nm to 200 nm. Herein, the illumination is at normal incidence and linearly polarized. One may observe the variations of plasmonic resonances such as widths and peak position changes for different periods of the same nanocylinder. If we compare for the periods of 1000 nm and 600 nm for different diameters of GNC, we can see that depending on the diameter the spectra for the periods of 600 nm is blue or red-shifted with respect to the periods of 1000 nm. The distance between the nanoparticles has an influence on the signal in different ways: on the one hand a widely-spaced array does not give a much higher signal than the single NP, on the other hand compaction of the array leads to the stronger appearance of the diffraction orders in the visible range. We chose a pitch of $1\mu m$ to have a good compromise between the signal-to-noise ratio and the grating influence in order to compare it with single nanoparticle plasmonic resonances.

In Fig 3.12a and 3.12c we set apart the experimental extinction spectrum of the $1\mu m$ pitched arrays respectively for diameters of 135 nm and 170 nm. Though, the numerical simulation of the extinction spectrum of a finite size array is an issue as it

demands huge computational resources. Moreover, the extinction spectrum of infinite size array differs drastically from finite size array extinction spectrum [82].

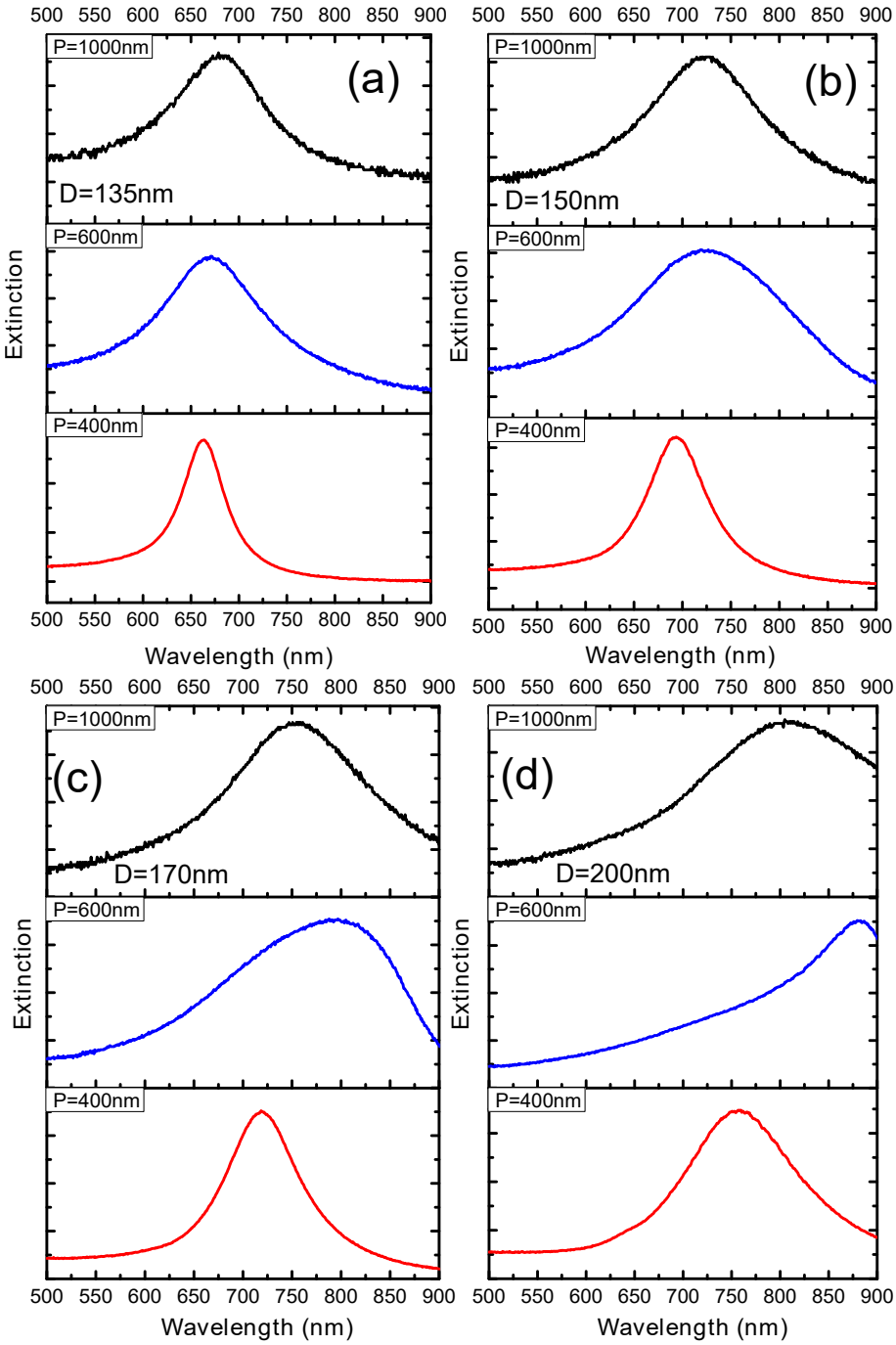

FIGURE 3.11: Experimental extinction spectra for GNC arrays with a diameter of D and the period of P.

We decided to simulate the extinction spectrum of a single GNC (3.12b, 3.12d, 3.12f). There is a good agreement between numerical and experimental results. In order to compare the ensemble measurements with a single one we also show the experimental

DF reflection scattering spectrum of a single GNC in Fig. 3.12g. The spectrum shows a peak at 764 nm and it has a FWHM of 254 nm.

We calculated the DF scattering spectrum via simultaneous use of p-polarized and s-polarized angle excitation. Note, that the collection angle (NA=0.8) of the experiment is applied in the numerical simulation. We show the dark field simulated spectrum on Fig. 3.12h. The obtained spectrum has a maximum at 746 nm and has a FWHM of 217 nm. One may note a satisfactory agreement between experimental and numerical results, even if there is a discordance of 18 nm in the peak positions. The accurate modeling and simulation of the dark field illumination is a hard issue due to an infinite number of high angles excitations in the range of the objective numerical aperture.

The extinction simulation of 170 nm-diameter shows a 744nm peak position and the experimental one is 742 nm. Furthermore, the peak positions of simulated DF scattering spectrum and the extinction spectrum of single GNC are very close, respectively at 746nm and 742nm. We can see that the spectra obtained by different techniques of a single GNC and of an ensemble of GNC have similar features.

A periodic array of nanoparticles with a grating constant of 1 μm supports many diffraction orders in the visible and near infrared wavelength ranges. In Fig 3.13a we show the calculated number of supported propagating grating orders for normal incidence and wavelengths ranging from 500 nm to 850 nm in glass using the grating theory (equation 3.6).

$$\begin{aligned} k_{x(m)} &= k_{x,inc} - mK_x \\ k_{y(n)} &= k_{y,inc} - nK_y \end{aligned} \tag{3.6}$$

where, $k_x(m)$ and $k_y(n)$ are diffracted wave vector components, n and m are integer numbers defining the diffraction orders, $k_{x,inc}$ and $k_{y,inc}$ are incidence wave vector components, and K_x and K_y are grating vectors components. Note, the number of the supported diffraction orders is greater than in air side (illumination side) due to the higher refractive index (1.52) of the glass.

One may ask why if we have so many diffraction orders as we do not see them or their influence on the experimental extinction spectrum (Fig. 3.12a and 3.12c). Indeed, diffraction orders have in-plane (grazing) or out-of-plane propagation. They may be seen in two different ways. Firstly, the out-of-plane diffracted orders can propagate directly to the objective. Secondly, diffraction orders may couple with LSPR and modify it, the stronger coupling occurring for in-plane orders. We present a far-field map of out-of-plane diffracted orders in the glass at a wavelength of 502 nm and 850 nm on the Fig 3.13a and 3.13b correspondingly. Considering Snell's law, above 41° in the glass, the light will be totally internal reflected. Thus, many orders will be locked up

in the glass slide and will not be transmitted. The 0.42 numerical aperture collection angle in air corresponds to an angle of 24°, which is half of the full angle collection of the objective. According to Snell's law 23° in air corresponds to 16° in glass.

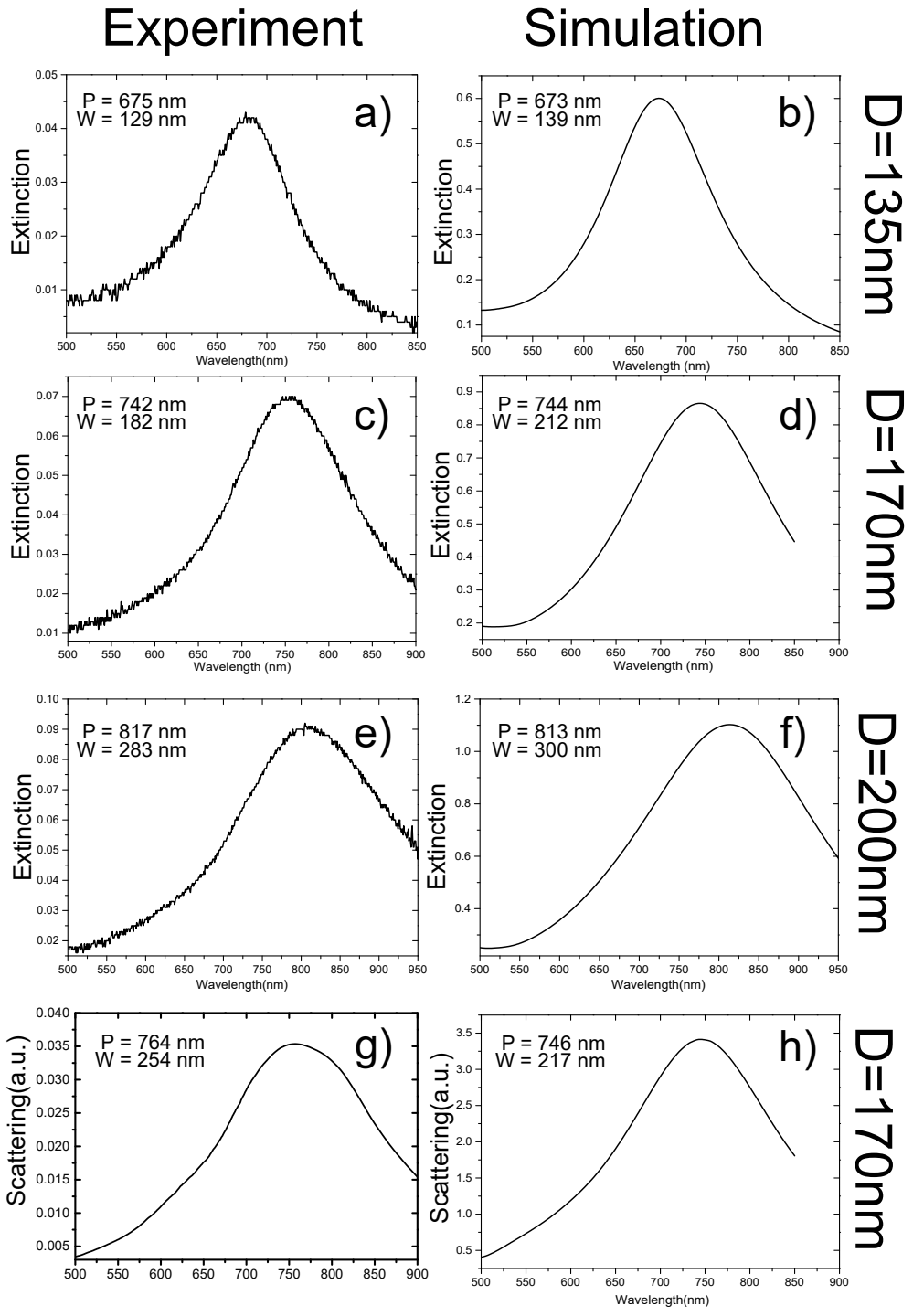

FIGURE 3.12: (a-f)Extinction spectra of GNC arrays with a period of $1\mu m$. D is the diameter of GNC. P is the peak position of spectrum and W is the width of the spectrum. (g,h) DF scattering spectra (smoothed) of a GNC.

One may note by looking at Fig 3.13b and 3.13c that we collect only the zero order of diffraction. Hence, we will not have directly diffracted light into the objective. Nevertheless, extinction spectroscopy measures the total losses and thus an extinction spectrum includes all optical losses due to the diffracted orders as well. Here, the zero-diffraction order intensity is greater with a factor of 10^2 - 10^3 than the intensity of other out-of-plane diffracted orders (see in Fig 3.13b and 3.13c). Accordingly, we do not observe them on the experimental extinction spectrum.

The strongest coupling between diffraction orders and LSPR is for (0, $\pm$1) and ($\pm$1, $\pm$1) in-plane diffraction orders [83]. We calculated that the wavelengths of these orders are out of our collection spectrum range as they are at 1.52 μm (0, $\pm$1 orders) and 1.075 μm ($\pm$1, $\pm$1 orders) wavelengths correspondingly.

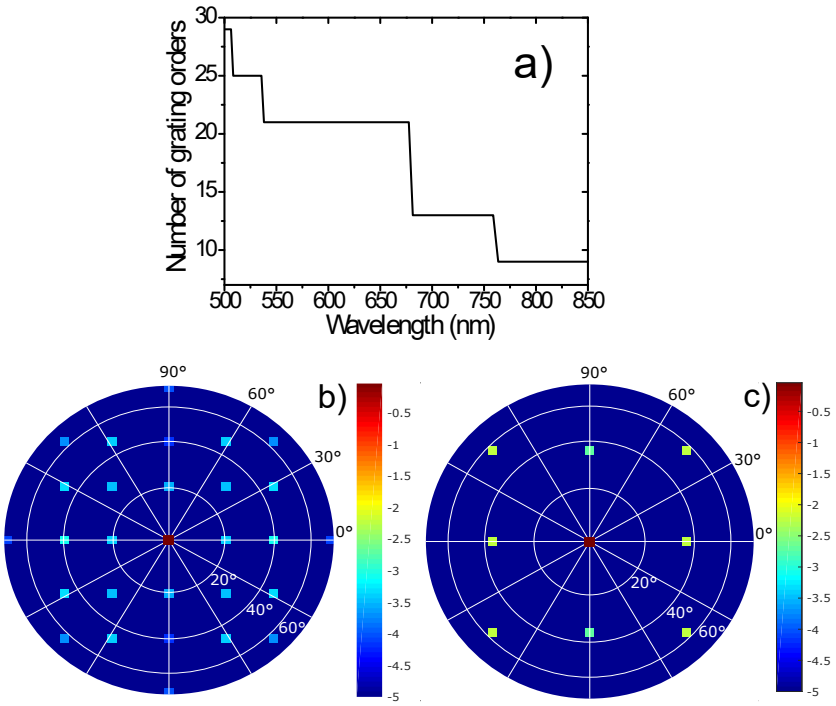

FIGURE 3.13: (a) Supported propagating orders in the glass for infinite periodic 170 nm GNC array with 1μm pitch. (b) Far-field distribution of diffracted orders in the glass at wavelength of 502 nm and (c) 850 nm. Scale is logarithmic.

3.6 Conclusion

Retrieving the experimental DF scattering spectrum of individual plasmonic nanostructures is complex and the analysis of the data is complicated. We have shown here the problematic of DF spectroscopy, both in experiments and in numerical simulations. Many characteristic optical features may be smoothed out and a spectral broadening of the experimental spectra may as well occur. Considering the sensitivity of LSPRs

to the excitation angle and the importance of accurate optical characterization of the single nanostructures for applications, we have shown here a novel approach to the exploration of the single NP extinction spectrum using normal incidence illumination. The extinction measurements of an array of nanoparticles can be used to predict and describe the LSPR of a single nanoparticle in the visible-IR range. The comparison between the optical characterization of a single nanostructure and an ensemble of them shows similar results providing the grating spacing is well chosen. This analogy makes a simple, easy and fast characterization of optical properties of metallic nanoparticle produced by electron beam lithography as a $1\mu m$ pitch arrays. The minimum diameter 60 nm may be explored for a pitch size of one micron, but we believe this analogy is possible for smaller diameter if the pitch size is decreased to get enough signal-to-noise ratio. We thus demonstrate the advantages of extinction spectroscopy over the DF spectroscopy for single nano-object optical characterization.

"The numerical simulations are cool how long they exist, but not awesome how long they are not proved experimentally. "

Unkwown student

4 Hidden plasmonic modes

4.1 Introduction

The financial expenses on nanofabrication by lithography are huge considering their material (noble metals) and machines demanding high electrical power. The experimental instruments are expensive as well. With increase of the computational power of the supercomputers it becomes possible to predict and explain the plasmonic properties of the NPs and systems using the numerical simulations. The main question is whether the results of numerical simulations can be trusted. In the "Chapter 2" we presented the plasmonic modes of a single GNC floating in air, which is not possible to realize experimentally. Hence, we design a plasmonic NP placed on a substrate, which how they are produced in experiments. The simulations for exploring the horizontal dipolar mode of a single GNC do not creates any problem. However, we remember that to excite the quadrupolar and the vertical dipolar modes of GNC we used illumination from the side of the GNC (Insets of Fig. 2.12 and 2.8).

We understand that the approach used in simulations to excite the quadrupolar or vertical dipolar modes (an illumination from the side of GNC) is hard to reproduce experimentally. It has been shown that by using an angle illumination, it is possible to excite and record higher order modes like quadrupolar or octupole modes using an angle resolved extinction spectroscopy [57, 82, 84]. It was shown that vertical mode also can be excited in array using an angle illumination [84]. However, the reflection

and transmission DF spectra do not show these modes (Fig. 3.9 and 3.10). In the following, we will try to understand why the vertical and the high-order modes are not visible on the DF spectra and will propose a method to reveal them.

4.2 Revealing the hidden modes

4.2.1 Extinction spectra

We proved in “Chapter 3" that under some conditions the influence of the array on the LSPR can be negligible. For experiments we use an array of 170 nm-diameter and 50 nm-height GNCs, choosing $1\mu m$ pitch in order to match the condition, when the extinction spectrum of an array corresponds to the single GNC spectrum. The optical characterization is done with the help of the optical setup described in Fig. 3.4.

We perform the angle resolved extinction measurements for P and S polarized illuminations. The Fig. 4.1a shows the extinction spectra of the GNC array measured at different angles (15°, 30°, 40°, and 50°) relative to the objective optical axis. The illumination is P-polarized. The spectrum for the illumination at 30 degrees (red curve) shows a rise of the plasmonic band around 605 nm. Moreover, with the increase of the illumination angle besides the well pronounced peak (i) at 761 nm, one may see the appearance of two peaks, around 605 nm (ii) and around 525 nm (iii). The peak positions are determined by fitting the curve with Gaussian functions. It is important to note that new peaks were not observed for the 15 degrees or normal incidence illumination (Fig. 3.12c). Depending on the angle of the illumination the electromagnetic wave can couple to the plasmonic modes which are not excited for normal incidence [57, 82, 84]. The Fig. 4.1b shows the simulation of the extinction spectra of a GNC for the same conditions.

In Fig. 4.1c we show the experimental extinction spectra for a S-polarized wave at the oblique illumination from 15 to 50 degrees. There are two plasmonic modes expressed at 738 nm (mode 1) and at 601 nm (mode 2) for the illumination at 50 degrees. Mode 2 becomes more evident for 40 and 50 degrees illuminations, while for the normal and the 15 degrees incidences it is imperceptible.

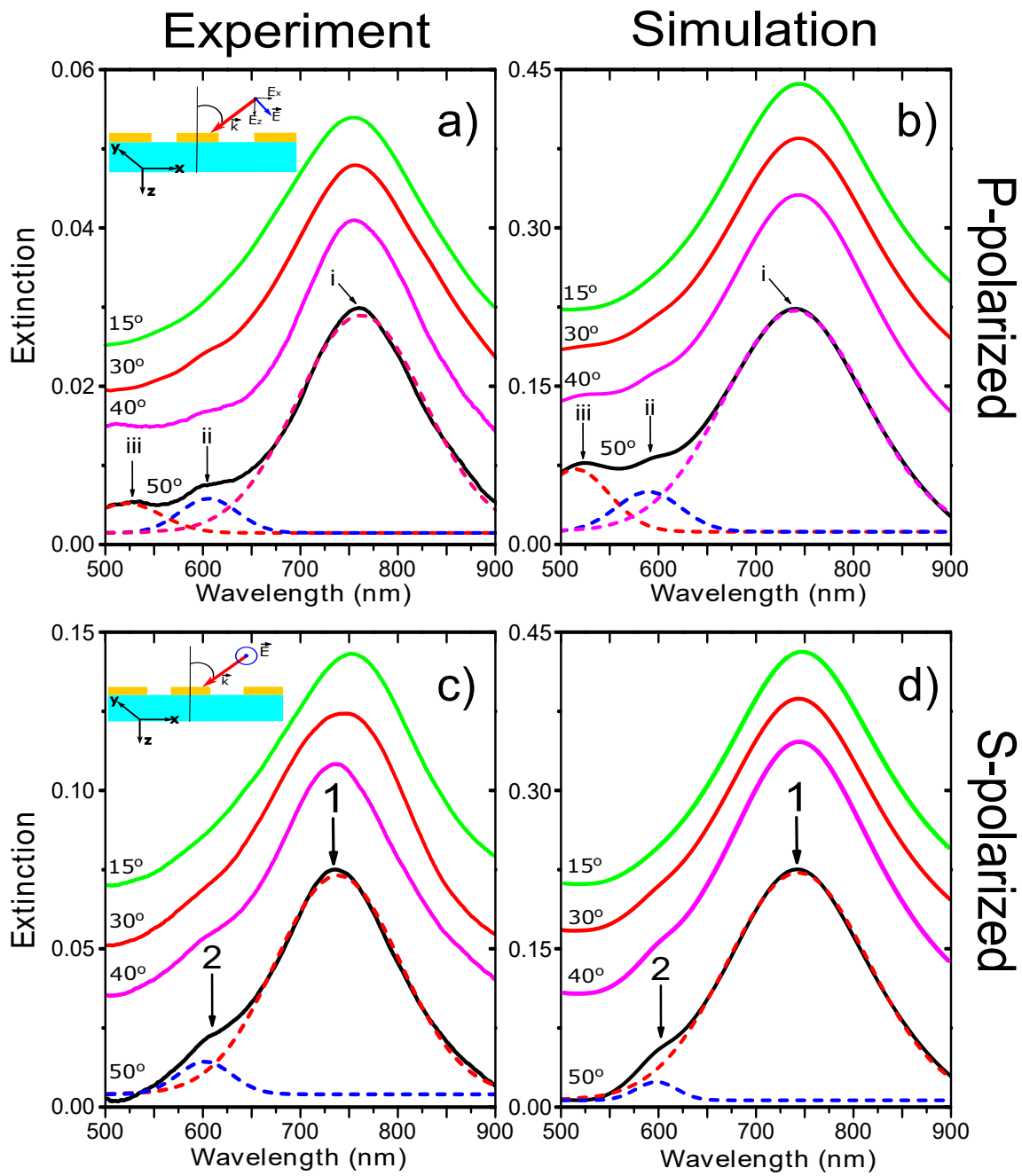

FIGURE 4.1: (a) Experimental P-polarized angle resolved extinction spectra of GNCs (170 nm-diameter, 50 nm-height) for different angles of illumination, (b) corresponding numerical simulation. (c) Experimental S-polarized angle resolved extinction spectra different angles of illumination, (d) corresponding numerical simulation. The dashed lines are the fits of the spectra by Gaussian profiles. The spectra are offset for better visualization.

The simulated extinction spectra of the GNC for the S-polarization are shown in Fig. 4.1d. One may note a good agreement between the experimental and calculated spectra for both polarizations.

4.2.2 Hidden modes plasmonic nature

To understand the nature of the non-dipolar modes we show the calculated scattering and absorption spectra of GNC for different polarizations in Fig. 4.2. In this manner we separate the radiative and non-radiative contributions of the plasmonic modes. The calculated absorption and the scattering spectra for P-polarization illumination are shown in the Fig. 3a (respectively black and red curves). The absorption spectrum shows three plasmonic modes labeled (i), (ii) and (iii), while the scattering spectrum shows a small shoulder between the position of mode (ii) and mode (iii). The radiative losses cause a strong broadening of the plasmonic resonances and the modes (ii) and (iii) are overlapped and not separable in the scattering spectrum. We assume that the non-radiative losses cause smaller spectral broadening, which leads to the separation of modes in the absorption spectrum.

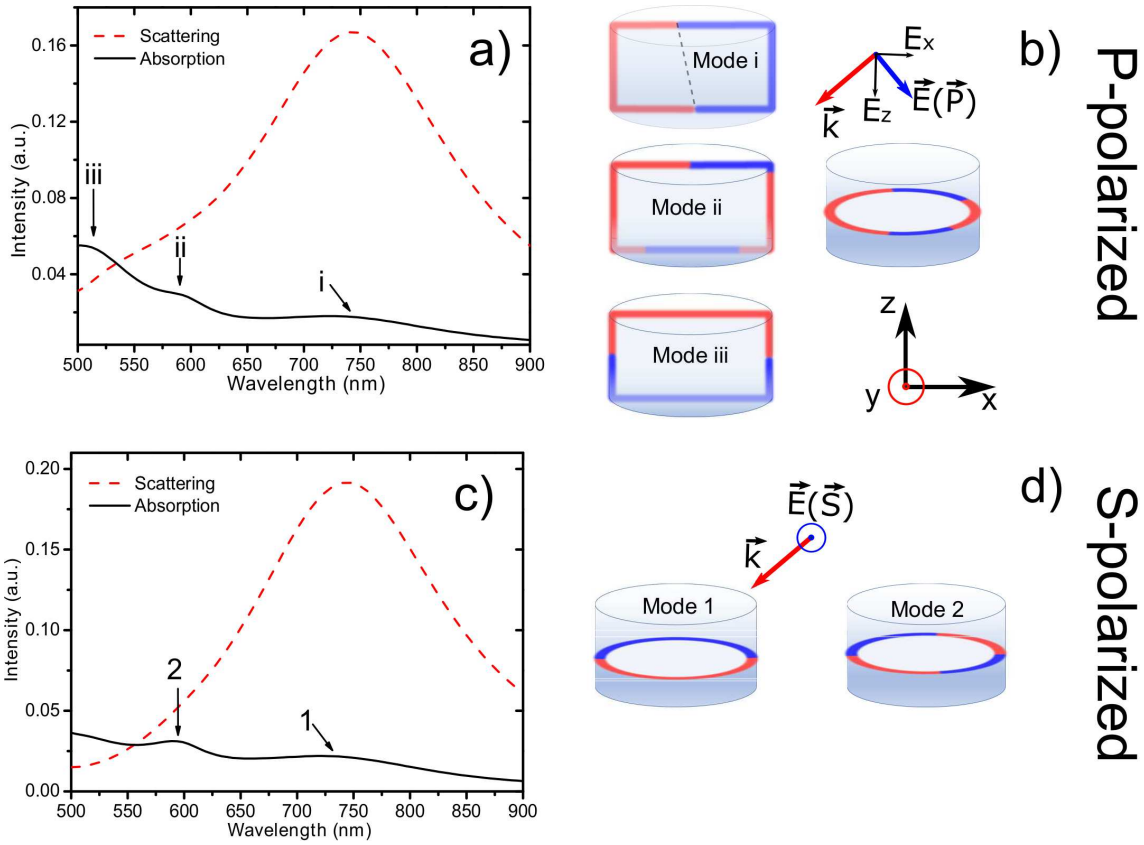

FIGURE 4.2: (a) Calculated absorption and scattering spectra (collection- 4π) of the GNC, when the illumination is at 50 degrees and P-polarized. (b) Calculated charge distributions for the wavelength of 523 nm (mode (iii)), 594 nm (mode(ii)) and 750 nm (mode(i)). The dashed line on the charges distribution map of mode (i) shows that the dipole moment is tilted with respect to the normal. (c) Calculated absorption and scattering spectra of the GNC for 50 degrees and P-polarized illumination. (d) Calculated charges distributions for the wavelengths 588 nm ("mode 2") and 744 nm ("mode 1").

In Fig. 4.2c we show the absorption spectrum of GNC for S-polarized, 50-degrees

illumination. The absorption spectrum shows two plasmonic modes labeled (1) and (2) like in the extinction spectrum (Fig 4.1d), while the scattering spectrum (red curve in Fig. 4.2c) shows only one mode and it does not show any genuine radiative mode between 500 nm to 600 nm. Then we consider "mode 2" as a dark mode.

In order to identify the excited plasmonic modes we perform the surface charges distribution (SChD) calculations. The calculated SChDs of 750 nm (mode i), 594 nm (mode ii) and 523 nm (mode i) for P-polarized, 50 degrees, plane wave excitation are shown in the Fig. 4.2b. The excitation wave vector and the electric field directions are depicted also. Here, the mode (i) shows a defined dipolar mode excitation, where the negative and the positive charges are placed on the counter sides and create an effective net dipole moment. The mode (ii) SChD on XZ (out-of-plane) profile is revealed to be a diagonal quadrupole-like mode. The excitation of a quadrupole mode takes place when there is an overlap between the field distribution of the incident planewave and the field distribution of the mode itself. Herein, we demonstrate that it is possible to excite a quadrupole-like mode with an oblique illumination, since the opposite charges are counter localized compared to the illumination axis. On the one hand, using the oblique incidence we increase the optical path of the incident field along the GNC and the phase variations inside it, which results in a new plasmonic mode (mode ii). On the other hand, we obtain a complex and asymmetric charge distribution caused by the substrate. This asymmetric charge distribution of mode (ii) for in-plane (XY) and out-of-plane (XZ) profiles, leads to the radiative character of the mode due to the nonzero net dipole moment.

The mode (iii) is associated with a vertical dipole mode (Fig. 4.2b). Unlike the horizontal dipole (mode (i)), the vertical dipole oscillates along the height axis of the GNC. This mode is only visible under P-polarized illumination, since it requires an out-of-plane component of electric field (E_z) to be excited. To summarize, the P-polarized tilted illumination excites three plasmonic modes such as the horizontal dipolar mode (mode i), a diagonal quadrupolar mode (mode ii) and the vertical dipolar mode (mode iii) and they radiate.

In Fig. 4.2d we present the calculated SChD of the GNC XY profile, for 744nm, S-polarized, 50 degrees excitation. In this case the incoming electric field is parallel to the substrate. Herein, we clearly see that the "mode 1" is a dipolar mode. The calculated SChD for the "mode 2" (572nm) features the in-plane quadrupolar mode, when the two counter dipole moments result in almost zero dipole moment, and so a non-radiative or dark mode.

The extinction spectra on Fig. 4.1a and 4.1c show that the oblique incidence can excite other modes than dipolar. However, the scattering spectrum on Fig. 3.5b (Chapter 3) shows only a dipolar mode although the conditions to excite higher order modes

like the illumination at oblique incidence, are there. Indeed, the main difference between the extinction and the DF scattering measurements is the collection process. We confirm the assumption that an oblique incidence may excite other modes than dipolar but they are not detected by the DF microscopy.

4.2.3 Far-field simulations

In order to further to understand why we do not observe experimentally the higher order modes in the DF spectrum we perform the calculation of the scattering radiation patterns for two collection geometries (reflection and transmission) and two polarizations in air (Fig. 4.3). The Fig. 4.3a and 4.3b show the illumination geometry respectively for the P and the S polarizations. The illumination takes place at the angle of 50 degrees compared to the normal of the sample (marked as 90° on the schemes). The red dotted semicircle corresponds to the transmission geometry and the green one corresponds to the reflection geometry. The calculations are done for an azimuthal angle equal to zero and the polar collection angle varies from 0 to 180 degrees. The Fig. 4.3c pictures the radiation pattern for the reflection geometry projected on a semicircle. The horizontal axis shows the wavelengths and the vertical one shows the polar angle. For all the far-field maps the prominent dipolar mode peak is at the wavelength of 750 nm and at the angle of 100 degrees. The emission of a horizontal dipole should be centered at 90°, but in our configuration the tilted illumination creates a tilted dipolar moment, as shown on the charge distribution of mode (i) (Fig 4.2b). This 10° shift is then a consequence of the tilted illumination.

Besides the main dipolar mode, there are several modes in form of two lobes in different directions (indicated by white arrows on the figures). One is mostly back scattered (120-160 degrees) at the wavelengths 500-560 nm and the second is forward reflected (20-50 degrees) at the wavelength 570-610 nm (Fig. 4.3). Although these lobes for transmission and reflection geometries show the radiative nature, we do not see clearly these modes on the scattering spectrum (Fig. 3.5b).

The simulated scattering spectrum on Fig. 4.2a shows that even if we could collect the scattering for full 4 π angle, we do not see other mode than dipolar one. Indeed, the strong dipolar mode intensity covers the other modes and make them invisible. Moreover, the experimental scattering spectrum is collected by an objective with a numerical aperture of 0.8 represented by the horizontal dashed lines on Fig 4.3c and4.3e. Therefore, it does not collect completely the radiated power of the lobes as their radiation is out of the collection zone. That is why we do not observe in the experiments clearly these new modes on the DF scattering spectrum.

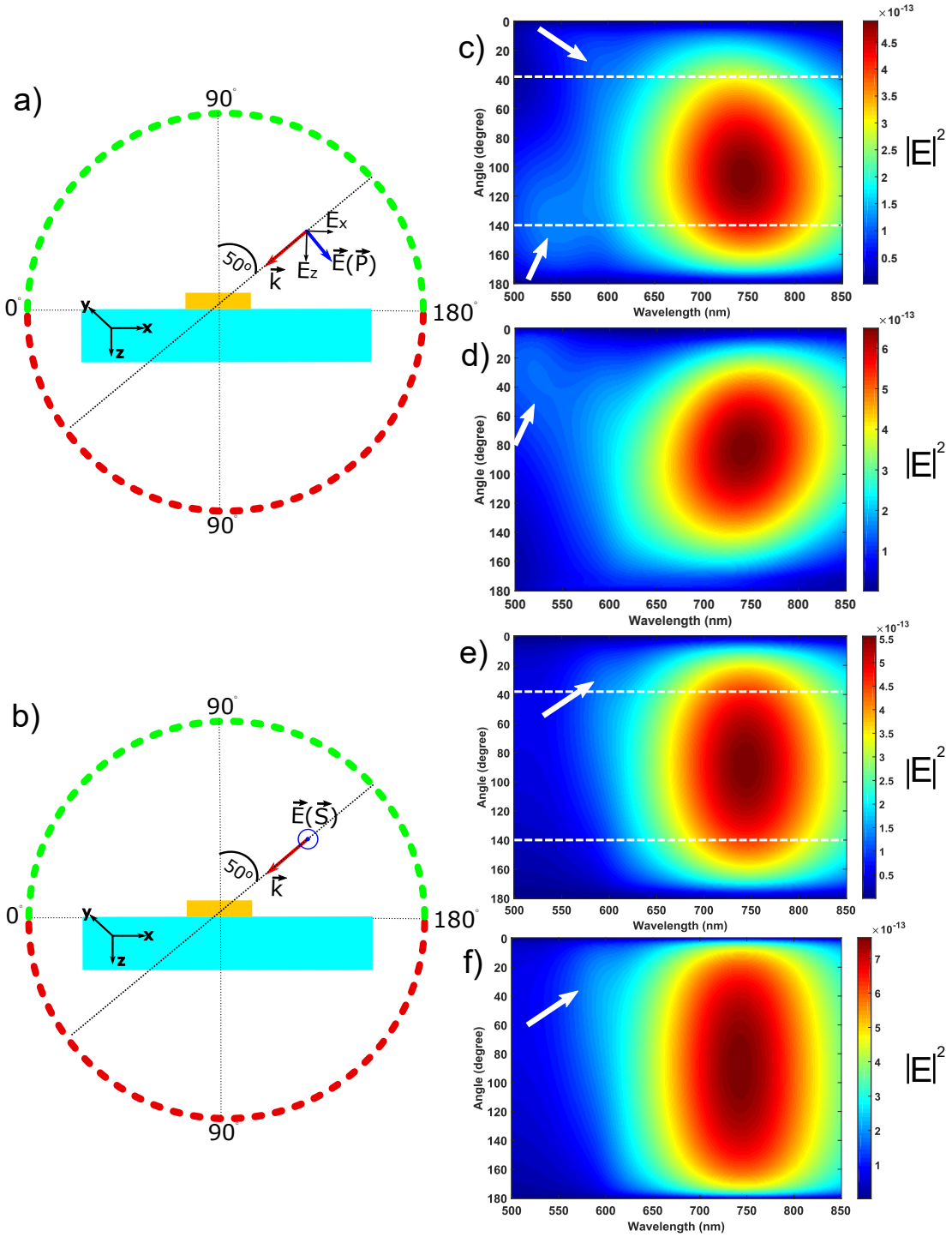

FIGURE 4.3: (a) and (b), schemes of the P-polarized and S-polarized 50 degrees excitation respectively. The reflection and transmission collection geometries are given by the green and the red dotted semi-circles respectively. k - wave vector, E - electric field, P and S - polarization, E_x and E_z components of the electric field. (c) and (d), angle dependent collection far-field map for reflection and transmission geometry respectively for P-polarized, 50 degrees excitation. (e) and (f), angle dependent collection far-field map for reflection and transmission geometry respectively for S-polarized, 50 degrees excitation. The white dashed lines show the collection boundaries for a numerical aperture 0.8, when the collection is centered at 90 degrees

The radiation patterns of the reflection and the transmission collection geometry for a S-polarized illumination are shown respectively in the Fig. 4.3e and 4.3f. These maps show a mode (560-620nm range) which radiates from 20 to 40 degrees.

However, the scattering spectrum (Fig. 4.2c, red curve) does not show any evidence of the quadrupole mode ("mode 2"), even though there is a small radiative part besides the absorption. Herein, also the dipolar mode covers other excited modes due to the ratio between the radiative weights of each mode. Therefore, the only way to observe these new modes using the scattering technique is to minimize the horizontal dipolar mode contribution on the recorded scattering spectrum. Although it has been reported multiple studies of plasmonic nanoparticles using scattering microscopies, these hidden modes were not observed due to their low scattering cross-sections compared to the main dipolar mode [85–89].

To summarize, the lobes observed in the far-field maps (Fig 4.3c and 4.3d) have quadrupole-like and vertical dipolar modes nature. The full spectrum far-field map is a practical tool to observe different plasmonic modes radiation among all spectral range.

4.2.4 Revealing the hidden modes using DF microscopy

We have seen the different modes radiation features and understand why DF-scattering technique does not record other modes than the horizontal dipolar one. Considering the specifications of different modes radiation we propose a method to retrieve these “hidden modes" with DF technique.

Fig. 4.4 shows the dark-field scattering spectra for a GNC when the collection zone is either centered on it or apart from it. These spectra have been recorded by using a piezo stage. In the case of D = 0, the GNC is centered compared to the collection zone as shown by the dark-blue dashed line on the inset of Fig. 4.4.

If we move laterally the sample to a distance D, the collection area is moved to the same distance. It is important to note that a micro-metric motion cannot change significantly the excitation process as the illumination with a broadband source has a large (hundreds of microns) spot. The red dash line on the inset of the Fig. 4.4 (gray colored zone) corresponds to the new collection angles. In this manner we change the collection geometry and filter some radiation coming from the dipolar mode. In that case, the ratio between the radiations collected from the dipolar mode and from the other modes is changed.

The translation of a distance below 500 nm does not lead to any significant changes except the reducing of the dipolar mode intensity. The main changes on the scattering spectra are observed when the collection zone translation is 500 nm and more. The

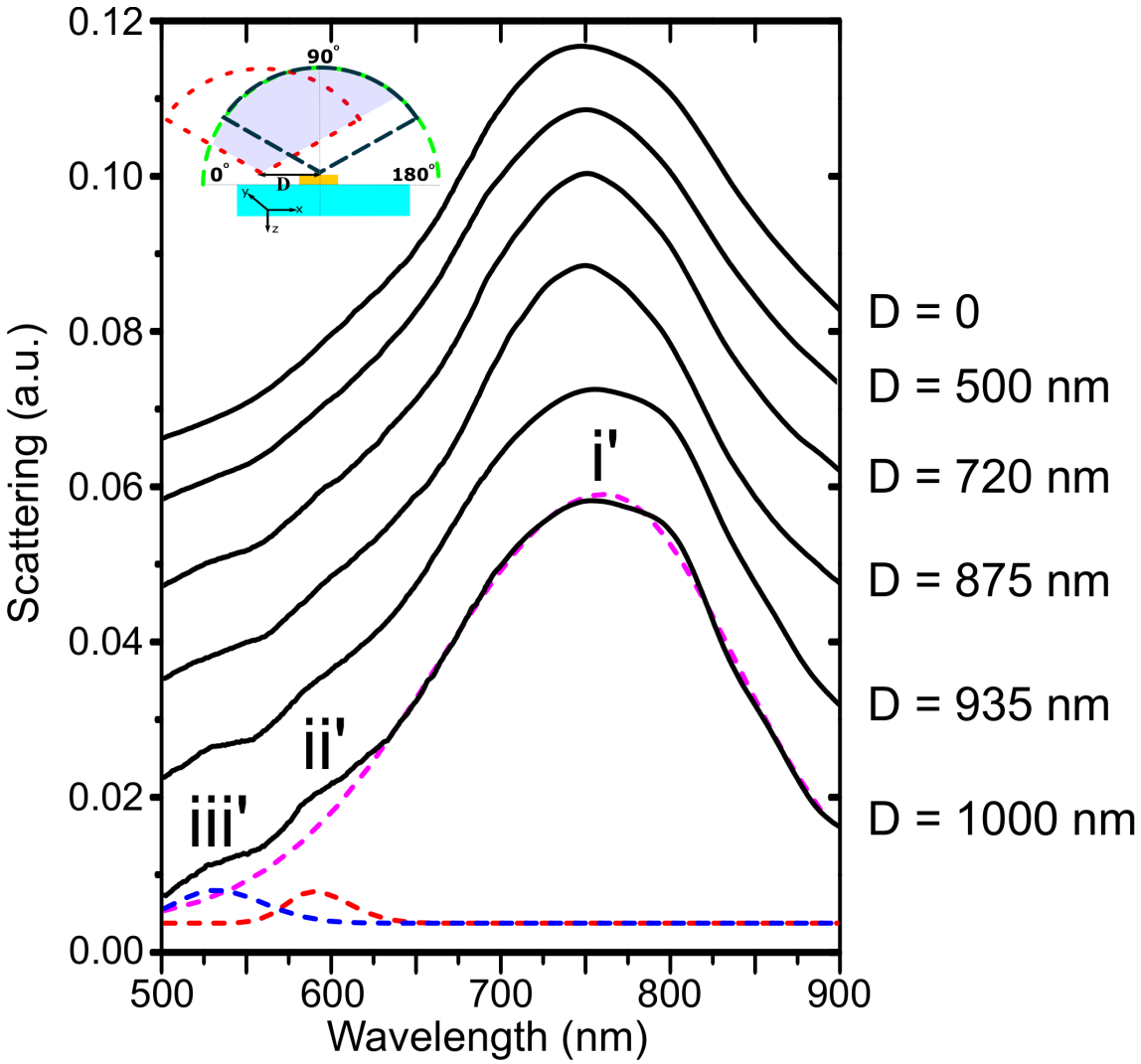

FIGURE 4.4: DF scattering spectra of a 170 nm-diameter GNC when the collection is centered on it and when it is moved from the center of the GNC by D distance. The inset illustrates the collection zones when the collection is centered on the GNC (blue dash line) and when the collection is moved from it (red dash-line) by D distance. The spectra are offset for better visualization.

spectrum for D = 500 nm shows a small plasmonic band around 525 nm and a symmetry breaking of the main peak (left side around 550 nm). For the furthest translation of the collection zone, one may observe that another plasmonic band arises around 585 nm. This mode is observed for longer translation because the long distances provide a strong reduction of the dipolar mode contribution, which enables one to observe the hidden modes.

Indeed, the experimental dark-field scattering spectrum recorded with this new collection geometries (Fig. 4.4, D = 1000 nm) confirms the detection of new peaks (mode (iii') and mode (ii')). The mode (i') is the prominent dipolar mode, whereas the mode (iii') is vertical dipolar mode and the mode (ii') matches spectrally with the

quadrupolar mode. Note, the dark-field illumination contains in-plane and out-of-plane components of the electric field. They may excite two quadrupole modes such as in-plane (mode 2) and diagonal (mode ii), which are spectrally close. Therefore, the scattering spectrum represents the contributions of in-plane and out-of-plane excited modes.

4.2.5 Presentation of a faster way to simulate hidden modes

In "Chapter 3" we presented an overview of the difficulties one has to face when calculate an angle illumination. Moreover, to retrieve the quadrupolar and horizontal dipolar modes of GNC on a substrate using the illumination from a side by FDTD simulations like we did in Chapter 2 is not possible. We decide to use the model of so called effective refractive index, when the air-substrate (glass) system is presented as a homogeneous index medium (1.3) [57]. In this manner we can perform the FDTD simulations using side illumination that presents GNCs deposited on the substrate.

The Fig. 4.5 depicts the extinction spectra maps of GNC in homogeneous medium of the refractive index 1.3. Herein, these maps show the excited horizontal mode of GNC for different heights and diameters illuminated from the GNC top.

The modes for the GNC in refractive index of 1.3 have the similar behavior to the presented previously modes for GNCs placed in air (Chapter 2). With the increase of the height the LSPR peak is blue-shifted for the same diameter. For example, the GNC of 170 nm-diameter and 20 nm height shows a peak at 834 nm, while the same diameter and 50 nm-height GNC shows a peak at 762 nm. In Figure 4.6 we calculated the extinction spectra maps of GNCs of different diameters and heights using an illumination from GNC side, when the polarization is parallel to the GNC plane as shown on the inset (H=20 nm). We use similar illumination conditions in order to excite in-plane quadrupole mode of GNCs in air (Fig. 2.12).

We already mentioned that a medium with the higher refractive index than air increases the retardation effect. A quadrupolar mode becomes visible on the extinction spectrum of 140 nm-diameter GNC (Fig 4.6 H=20), while we can observe the quadrupolar mode for GNC in air, when the diameter is 160 nm (Fig. 2.12 H=20). If we verify the peak positions of the horizontal dipolar mode of 170 nm-diameter and 50 nm-height GNC for two illumination geometries presented in the insets of Fig. 4.5 and 4.6, the peaks are respectively at 762 and 774 nm. When the GNC is illuminated from the top side (Fig. 4.5) the optical path is equal to the height, in this case 50 nm, and for the side illumination (Fig. 4.6) the optical path is equal to the diameter (170 nm). We assume this shift is due to the difference of these optical paths of the incident field.

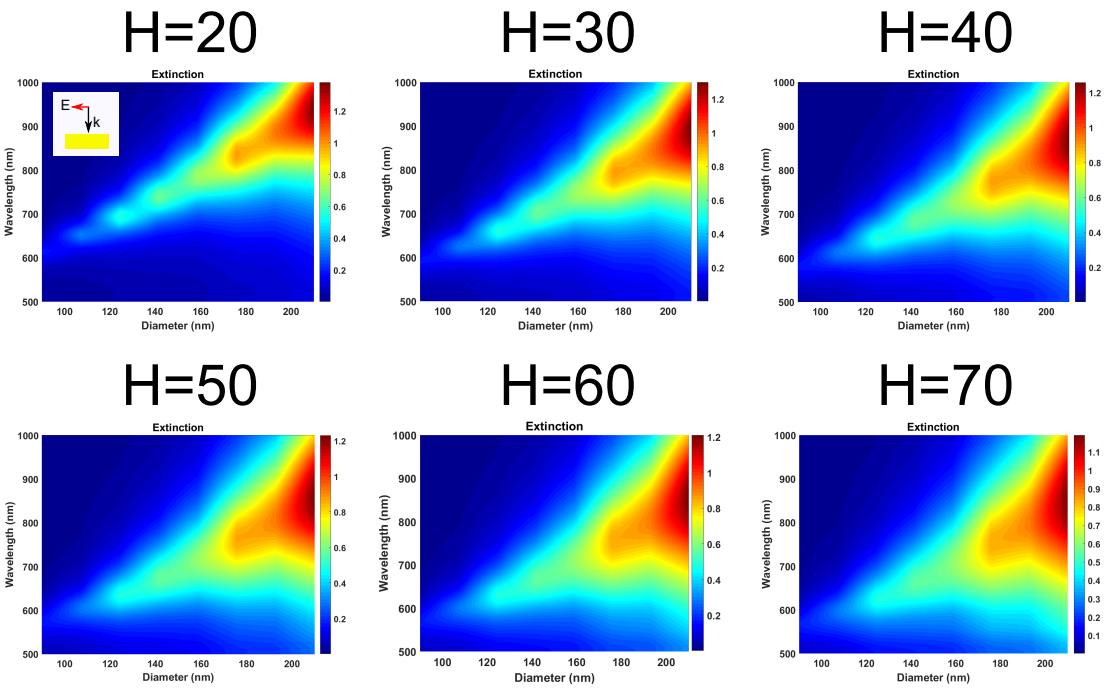

FIGURE 4.5: Calculated extinction spectra map of GNC for different heights depending on the diameters. H is the height in nm. The polarization is along the diameter. The horizontal dipolar mode is excited. The surrounding medium has a refractive index of 1.30.

We show the extinction spectra maps of GNC of different height and diameter, when the vertical mode excited in the medium of 1.3 refractive index in Fig. 4.7.

Herein, we observe redshifts of the vertical dipolar mode compared with the calculation done in air, as for horizontal and quadrupolar mode. The plasmon resonance redshift due to refractive index was predicted by equation 1.19.

Now, we can make a comparison of the spectral positions of the calculated plasmonic modes like horizontal, vertical dipolar and in-plane quadrupolar modes with the plasmonic modes revealed by the angle resolved method. The peak positions of the 170 nm-diameter and 50 nm-height GNC obtained for horizontal, vertical dipolar and quadrupolar modes respectively from the Fig. 4.5, 4.7, 4.6 show peaks at 762 nm, 538 nm and 590 nm. Indeed, the peak positions from calculation using angle illumination are slightly different like 744 nm, 523 nm and 572 nm. Nevertheless, we think that the complete nature of modes (1), mode (2) and mode (iii) revealed by tilted illumination can be different than the calculated horizontal, vertical dipolar and quadrupolar modes using normal incidence.

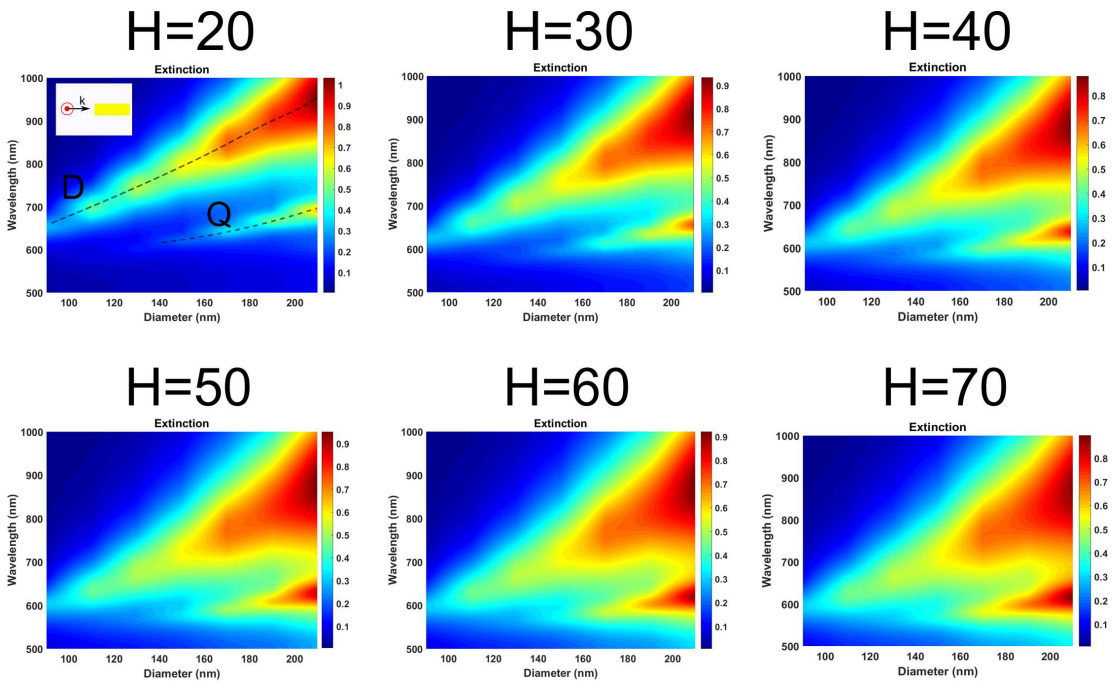

FIGURE 4.6: Calculated extinction spectra map of GNC for different heights depending on the diameters. H is the height in nm. The polarization is along the diameter and the illumination is from the side of GNC. The horizontal dipolar and quadrupolar modes are excited for big GNCs. The surounding medium has a refractive index of 1.30

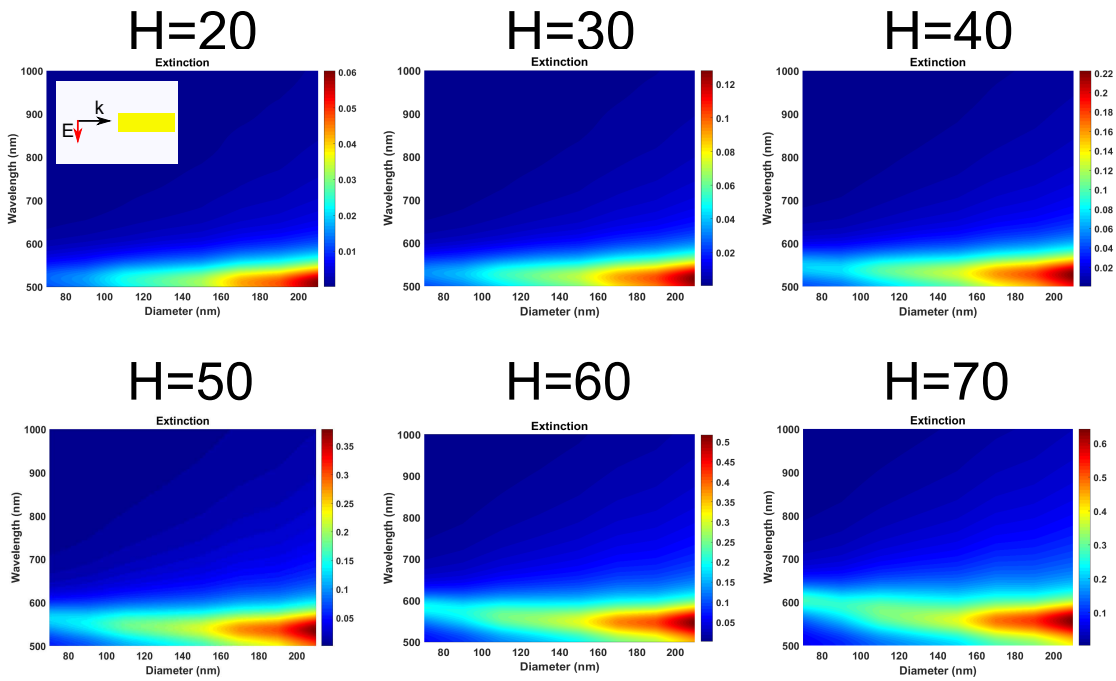

FIGURE 4.7: Calculated extinction spectra map of GNC for different heights depending on the diameters. H is the height in nm. The polarization is along the height. The vertical dipolar mode is excited. The surounding medium has a refractive index of 1.30

Due to angle illumination and substrate effect the plasmonic modes (mode (1), mode (2) mode(iii)) defined as horizontal dipolar, in-plane quadrupole and vertical

dipolar may have other near-field from these modes excited using other illumination geometry (shown in Fig. 4.6 and 4.7), even though the spectral positions are close enough.

As a proof we show the near field maps of horizontal and vertical dipolar modes excited by the angle illumination for the GNC deposited on a substrate in Fig. 4.8a and 4.8b. When we compare the near field of these modes excited by normal incidence (Fig. 4.8c and 4.8d) and angle illumination (Fig. 4.8a and 4.8b), we find that their near-field are not the same, although they are spectrally close and have similar nature (horizontal and vertical dipolar modes).

We have seen how the angle illumination can create tilted dipole mode or quadrupole-like mode excitation. Fortunately, the peak positions shift between experimental and simulated values using normal incidence are not more than 5 %. Therefore, from the point of view of the huge demanding computational time and resources for the angle illumination modeling, one may use the method of calculating described in the section above of this chapter using different illumination geometries and a surrounding homogeneous medium in order to determine multi-mode characteristics of plasmonic nanoparticles.

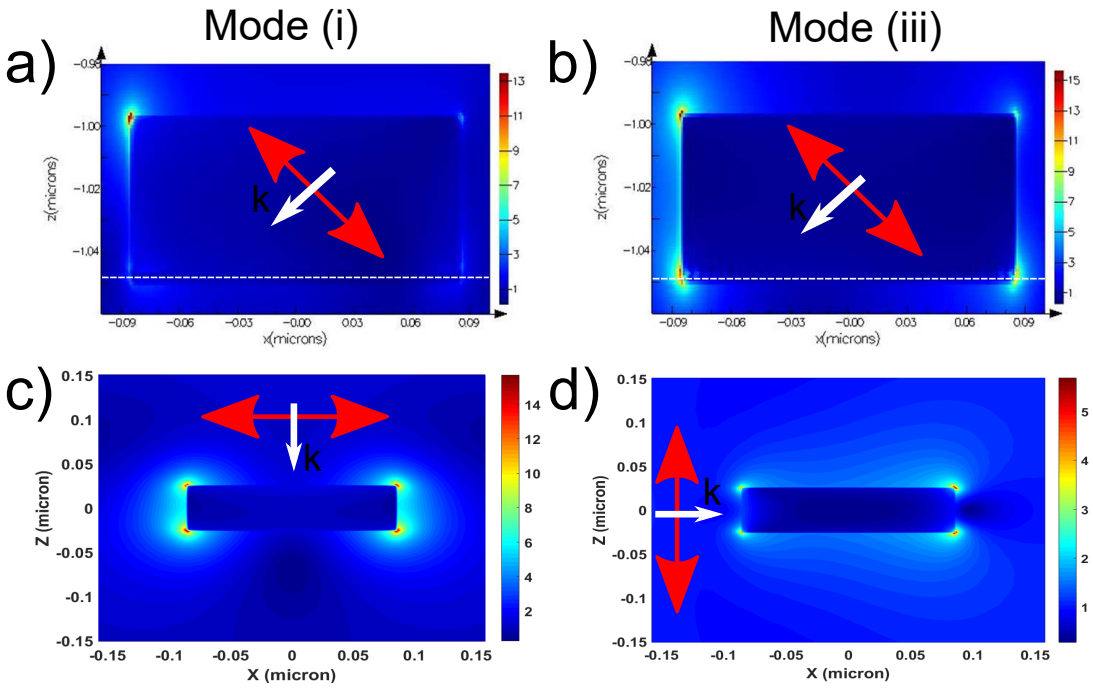

FIGURE 4.8: Electric near-field of (a) mode (i) and (b) mode (iii) excited by a planewave at 50 degrees. Electric near-field map of (c) horizontal and (d) vertical dipolar mode. Red arrows show the incident electric field polarization

4.3 Conclusion

In this chapter, we showed how to reveal plasmonic modes of gold nanocylinder using simple numerical simulations and how they differ from the simulations for the angle illumination. We studied with a use of the angle resolved extinction spectroscopy and numerical simulations hidden plasmonic modes of a gold nanocylinder of 170 nm-diameter. We reported on the experimental observation of the quadrupolar and vertical dipolar mode besides the horizontal dipolar mode in a single nanocylinder. The calculations of far-field maps for a wide spectral range explain why some of these modes are hidden on the scattering spectra. Furthermore, we showed that adapted version of the dark-field spectroscopy can be used for disclosure of these modes.

5 Hybridization of plasmonic modes

5.1 Context

In previous chapters we discussed the number of factors effecting the plasmonic resonances of a single metallic nano-object. The deep understanding of their influences allows to control and manipulate the plasmonic modes excitation and spectral position. It was found that besides the initially bright modes it is possible to excite the dark or almost dark modes under certain conditions. One of the way is to take advantage of the retardation effect, but this approach is suitable only for the nanoparticles of size comparable to the wavelength.

Another mechanism to reveal the dark modes is to study their coupling with bright modes. The coupling arises with a symmetry breaking of the system. For example, an anisotropic medium can cause a coupling between dark and bright modes. The coherent coupling, when besides the spectral overlapping there is a spatial overlapping, creates so called Fano resonance [90]. When, the resonant conditions are matched, the highly confined energy is located around the particle. The spatial localization depends on the plasmonic mode nature. Besides the spectral position of plasmonic resonances, the spatial disposition of the electric field is of prime interests for applications, such as biomolecule detection using environment change effect or surface enhanced spectroscopy.

To understand the plasmonic modes behavior in a coupling regime, Prodan *et al.*

proposed a so-called hybridization model [91]. This model has some similar features with a molecular orbital theory. The theory of hybridization for plasmonic modes aims to explain the behavior of the complex plasmonic structures with a use of its decomposition to the simple nano-objects. For example, the Fig. 5.1 shows the hybridization of the nanoshell modes. This nanostructure is presented in terms of the basic structures forming the nanoshell, in this case sphere and a cavity. The plasmonic modes of the sphere and the cavity interact with each other, which results in appearing of the two hybridized modes such as bonding (low energy (ω_-)) and anti-bonding (high energy (ω_+)). This model gives an understanding of the coupling between different plasmon modes.

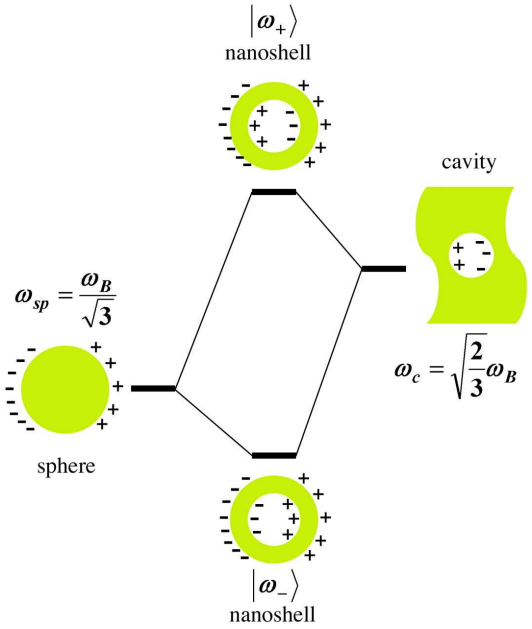

FIGURE 5.1: Model of hybridization of a nanoshell. ω_{sp} and ω_c are the surface plasmon energies respectively of the sphere and the cavity, where the ω_B is the plasmon energy of the bulk. The figure is extracted from [91].

In this chapter we propose an experimental study of hybridized plasmonic modes of silver nanocylinders disordered arrays on the substrate. Herein, for the first time we show experimentally two genuine localized plasmonic modes, where for the first mode the energy is confined near the substrate-air interface and for the second mode energy is confined on the top plane of nanocylinders. Also, we study the hybridization of the plasmonic modes of the gold nanospheres depending on the contact point with a substrate. Finally, we investigate hybridization of the plasmonic modes due to the shape symmetry breaking of the nanostructure.

5.2 Hybridization of silver nanocylinder modes

5.2.1 Introduction

This section is inspired by two papers, where Sherry et al. [92] and Zhang et al. [90] study the hybridization of two plasmon modes of a simple structure. Sherry et al. show experimentally and numerically the existence of two hybridized substrate mediated bright modes for a single silver nano-cube. For one mode energy confinement is located at bottom of the nano-cube, for another one it was on the top plane. Zhang et al. proposed theoretical model and explanation of these modes origin [90]. Although, Sherry et al. demonstrate two prominent modes in the experimental scattering spectrum for single nanoparticle, the measurements for the ensemble of the nanoparticles show only one plasmonic peak because of the inter-particle coupling and averaging effect. In this experiment the nanoparticles were produced chemically, then it was hard to control their position and exact size. Also the experimental setup included cooled chamber and piezo stage. Also we should note, that the scattering is only a part of the optical losses in a nanostructure, while the extinction measurements of a nanoparticles ensemble records all the losses and have higher signal-to-noise ratio (SNR). Practically, a low sensitive system is able to achieve good SNR using the extinction measurements of nanoparticles, which is essential for applications.

The effect of the substrate on the cylinder modes was predicted by simulations previously [93]. However, the mechanism was not explained on the base of the hybridization theory. In this section we deeply investigate the changes in optical response of the silver nanocylinder while approaching the substrate and confirm the simulated results with experiments.

5.2.2 Experimental and numerical simulation methods

The numerical modeling of a silver nanocylinder (SNC) placed on a substrate or apart are performed with the help of the commercial software FDTD solutions (Lumerical). For a planewave illumination we use TFSF (total field scattered field) source. The discretization mesh is 0.5nm. The normalized transmittance spectra are obtained with a “frequency-domain field and power" monitor. For numerical simulation, we use the dielectric permittivity of silver (Ref). The glass (quartz) substrate refractive index is 1.47.

The silver nanocylinders were fabricated with the help of electron beam lithography. To prevent the inter-particle coupling effect and diffraction effect of the nanoparticles array, we produced a disordered array. The minimum distance between the particles is three times diameter. The array measures 30x30 μm^2. The NPs nanocylinders

diameter is 70 nm and the height is 50 nm. We use 3 nm adhesion layer of titanium oxide in order to assure a good bonding between the substrate and the NPs. Optical spectroscopy is done with a standard homemade microscope using a collection lens (numerical aperture 0.2), equipped with a UV lamp source, a fiber-coupled spectrometer (Ocean Optics USB2000+). Optical spectra are acquired in transmission (transmittance T), normalized by the lamp signal (T_0), and plotted as $1 - T/T_0$. It measures the fraction of the light that is absorbed and scattered by the nanoparticles, in other words, we measure the optical losses. The nanoparticles sizes are measured with the help of an electron beam microscope.

5.2.3 Substrate effect

In Fig. 5.2a we show the calculated transmittance spectra of a single nanocylinder (SNC) in air and placed at different distances from a glass substrate. The transmittance spectrum for SNC in air show a single peak labeled (i) and a shoulder around 347 nm labeled (iii). With the approach of the substrate, the prominent peak (i) moves to the red and a new peak labeled (ii) appears. In contrary to the mode (i), which shifts when the substrate approaches, the mode (iii) stays on the same spectral position for different SNC-substrate distances. To understand the origin of the mode (iii), we calculate the electric field map and charge distribution for an excitation at 345 nm in Fig. 5.2d. The electric field is confined on the nanoparticle surface and sides. The charge distribution at the top plane of the nanocylinder has a unusual behavior. Unlike the dipolar, quadrupolar and higher order modes, which has the electric field localization near the edges of the nanoparticle. The black arrow on the Fig. 5.2d highlights the calculated charge distributions map of top plane. This map shows that the mode (iii) besides one azimuthal node, which is characteristic for the dipolar mode, has a radial node. The nodes are labeled on the figure. We attribute this mode to the admixture of a radial and the azimuthal modes. Indeed, a similar mode of nanocylinders was observed in several works [57, 94, 95].

The electric field map of mode (ii) is depicted on the Fig. 5.2c. The main electric field confinement is noticed on the edges of the top plane of the SNC. Corresponding surface charges distribution is shown in Fig. 5.2e. It has kind of dipolar mode distribution with charges mostly localized on the corners of the top plane of the SNC.

The mode (i) shows a feature of dipolar mode with a strong confined field located on the edges of the bottom plane (Fig. 5.2d). The calculated surface charges distribution of the mode (i) is presented respectively in Fig. 5.2f.

The mechanism of creation and the appearance of similar mode (i) and mode (ii) are explained for a silver nanocube by Zhange *et al* [90]. We present an analogical model

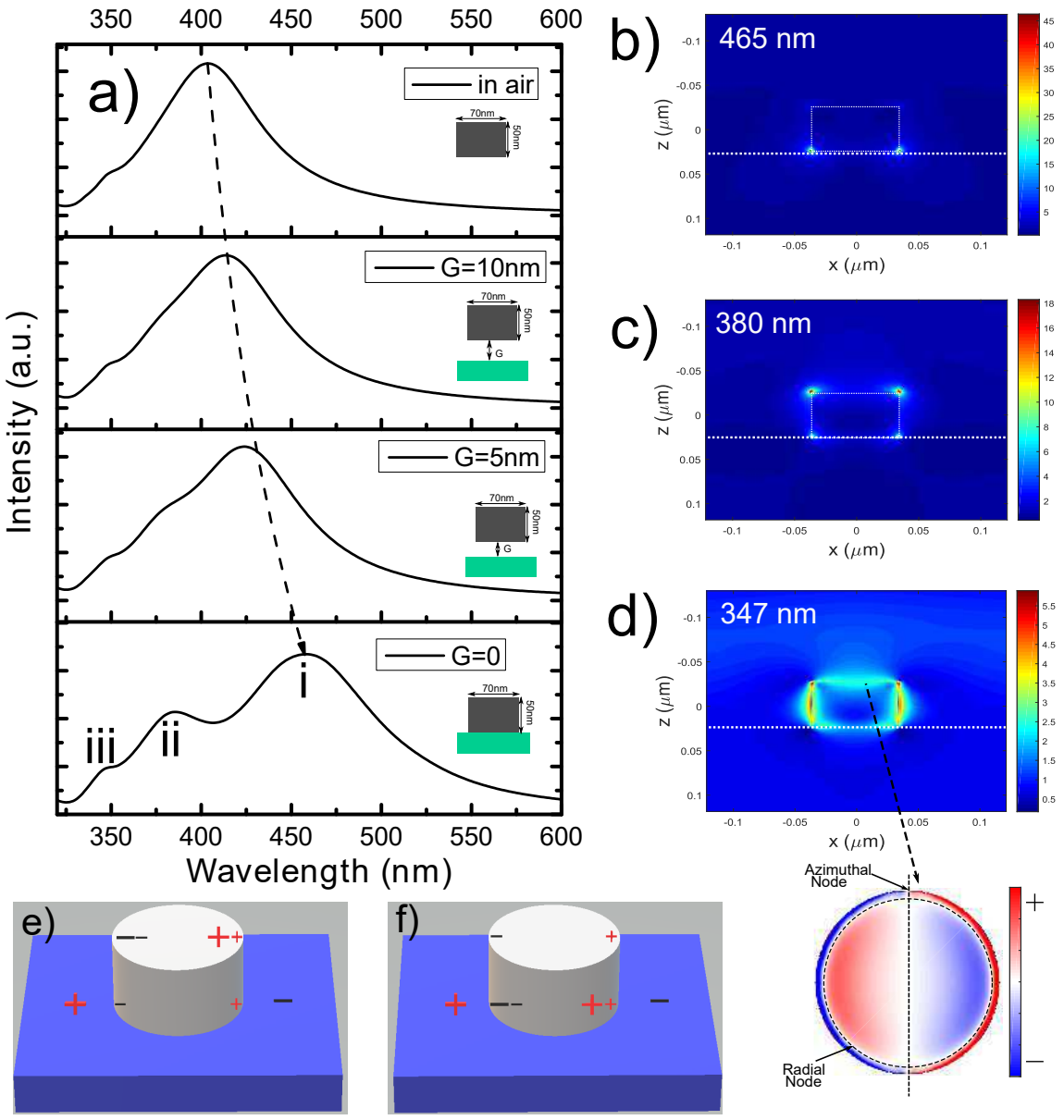

FIGURE 5.2: (a) Calculated transmittance spectra of a silver Nanocylinder in air and different distances from glass substrate, the diameter is 70 nm and the height is 50 nm. (b) Electric field maps: XZ cut profile in the center of nanocylinder. White dashed lines shows the substrate surface, the dotted lines show the nanocylinder. EF map for 465nm excitation (Mode i) (c) 380nm (Mode ii), (d) 347nm (Mode iii). Charges distribution for (d) mode (iii), (e) Mode ii and (f) Mode i.

for a nanocylinder in Fig. 5.3. To understand the behavior of the single nanocylinder modes near a dielectric substrate, we distinguished the contributions of the initial modes (modes of a SNC without the substrate). We consider an interaction between the bright dipolar mode and dark quadrapolar mode existing in the nanocylinder in air. Their energies are marked in Fig. 5.3 by white lines. When the SNC approaches to the substrate the both two modes red-shift due to the local refractive index change and

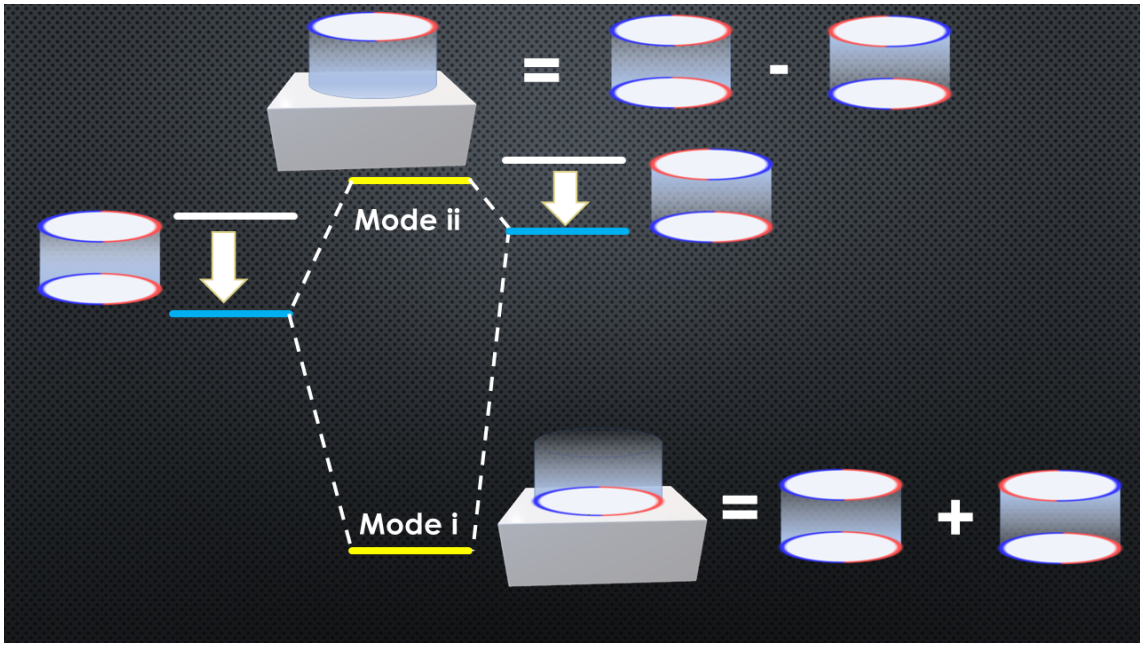

FIGURE 5.3: Model of the hybridization of dipolar and the quadrupolar modes of SNC.

their new energies are marked by blue lines. We assume these two modes are spectrally close and with the approach of the substrate they start to interact with each other and create new hybridized bonding (i) and anti-bonding (ii) modes. The energies of the hybridized modes are marked by yellow lines.

Then, for the SNC on the substrate, the mode (i) is represented as a sum of the dipolar and the quadrupolar mode (Look Fig. 5.3). With the approach of the substrate the redshift of the quadrupolar and dipolar modes are greater due to the increase of the effective refractive index, therefore their sum shows greater redshift. One can see clearly that with a smaller distance the redshift of mode (i) is higher.

In its turn, the mode (ii) originates from the dark quadrupolar mode [90]. This mode does not shift with the decrease of the SNC-substrate distance. It stands out from the mode (i) due to the redshift of the latter mode. We illustrate the mode (ii) as the difference between the quadrupolar and the dipolar modes (look Fig. 5.3). The mode (ii) stays almost stable with an approach of the substrate, although both the dipolar mode and quadrupolar modes should be red-shifted due to dielectric screening. We assume that the red-shifts of the dipolar and quadrupolar modes cancel each other for the mode (ii). Simply, if the dipolar mode is red-shifted by X value and quadrupolar mode by Y value, and the X and Y are close, their difference will not be significant. We cannot quantify the redshift of the intrinsic dipolar and quadrupolar modes separately, however the simulations show that mode (ii) is almost the same for all distances from the substrate, which means our approach is realistic. The similar observation was reported by Zhang et al. [90] for cubes. They explain the stability of the anti-bonding

mode by the compensation of the red shift due to the local refractive index change by the blue shift due to the hybridization.

5.3 Experimental study

We show the experimentally obtained extinction spectrum of SNCs deposited randomly on a glass substrate in Fig. 5.4a. Firstly, we notice two defined peaks in contrast to the three peaks that are present in simulations (Fig. 5.2a). Moreover, we clearly observe a non-symmetrical peak located at 485 nm.

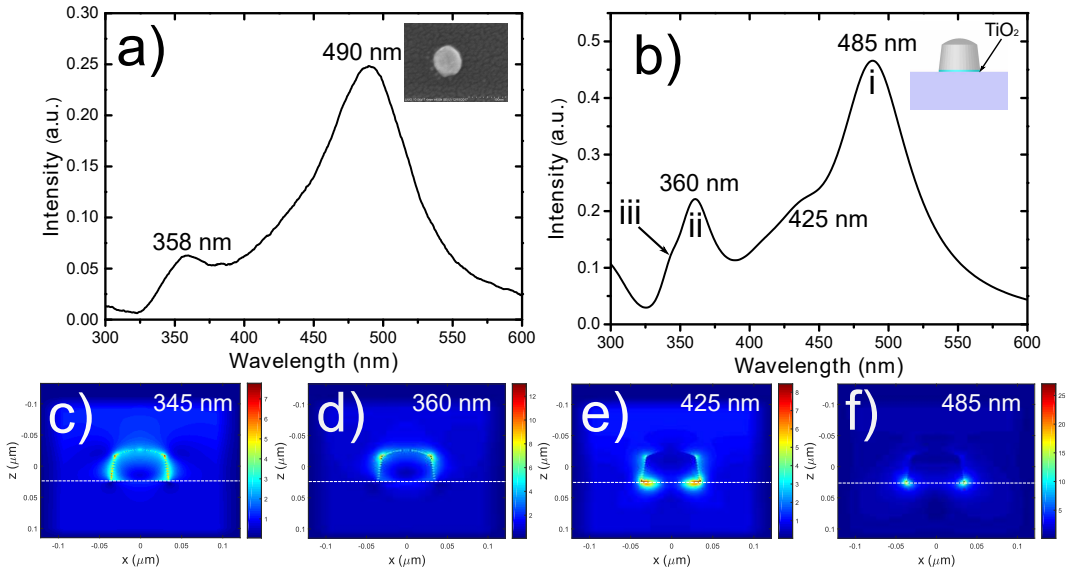

FIGURE 5.4: (a) Experimental transmittance spectrum of a SNCs, the diameter is 70nm and the height is 50nm, (b) Corresponding numerical simulation. (c) Electric field maps: XZ cut profile in the center of nanocylinder. Illumination is along z-axis from top side and polarized along x axis. Black dash line shows the substrate surface. EF map for 345 nm excitation (Mode iii), (d) 360 nm (Mode ii), (d) 425 nm (magnetic mode), (f) 485 nm (mode i)

We performed more exact simulations of the experiment taking in to account the peculiarities of the silver nanocylinders production (the shape of the nanoparticles and the presence of the adhesion layer). Indeed, the SNCs produced by the electron beam lithography do not have an exact cylinder profile. They have a curvature at the top plane and a small bending angle at the nanocylinder side walls (inset of Fig. 5.4b). In Fig. 5.4b we show the results of the more accurate simulations. One may observe a good match between the experimental and simulation spectra. The electric field maps of new modes are presented in the Fig. 5.4(c-f).

There are few main differences from the simpler simulations. Firstly, the mode (i) has strong red-shift compared to the simulations on the glass substrate (Fig. 5.2a) due to the higher refractive index of the titanium oxide than the glass.

Secondly, one can note that a shoulder from 420 nm to 450 nm appears on the spectra. The electric near-field map (Fig. 5.4e) shows the confinement of the electric field inside the titanium layer, then we assume that it is a mode of the titanium oxide layer. The layer of titanium oxide is very thin and it is not uniform (Fig. 5.4e). This is the reason why we do not see good prominent shoulder as in simulation.

Thirdly, the modification of the shape changes the spectral position of the modes. In fact, the hybridization model predicts that the mode (i) mostly localized on the bottom plane of the SNC, then it does not depend on the top diameter in contrast to the mode (ii). When we reduce the top plane diameter and change the curvature, the mode (ii) blue-shifts and spectrally overlaps with mode (iii). Even though the mode (ii) is modified after SNC profile changes, the electric field maps study shows confinement of energy on the top plane.

5.3.1 Silver Oxidation effect

In this section we present the experimental and simulated spectra of an SNC deposited on a glass substrate without any adhesion layer. We did it in order to simplify our problem and get rid of the cavity mode in the titanium oxide layer. The Fig. 5.5a shows the experimental spectrum of 70 nm-diameter SNRs. The corresponding simulated spectrum is shown on Fig. 5.5b.

Herein, we see clearly that there is no shoulder on the main peak on the experimental or simulated spectra unlike the system with the TiO_2 layer (Fig. 5.4a and 5.4a). The experimental spectrum of SNRs without TiO_2 layer is blue-shifted to about 50 nm compared to the spectrum with the adhesion layer (5.4a). One may conclude that the reason is the decrease of the refractive index of the inter-medium with the removal of the adhesion layer. However, the experimental and simulation spectra (Fig. 5.5) of SNR without adhesion layer do not perfectly match, particularly the main prominent peak. The mismatch of the main peaks between experiment and simulation is around 30 nm.

We assume that the silver evaporated directly on the substrate without any intermediate layer (TiO_2), is oxidized at the vicinity of the substrate, while the adhesion layer protects silver from the oxidation. To verify the proposed hypothesis, we add to the simulation a thin layer (2 nm) of silver oxide. In some papers the refractive index of silver oxide is given from 1.05 - 1.7 depending on the deposition process [96, 97]. When we choose 1.2, then the simulation and the experiment match sufficiently. However, we cannot explain the exact oxidation process and its chemistry.

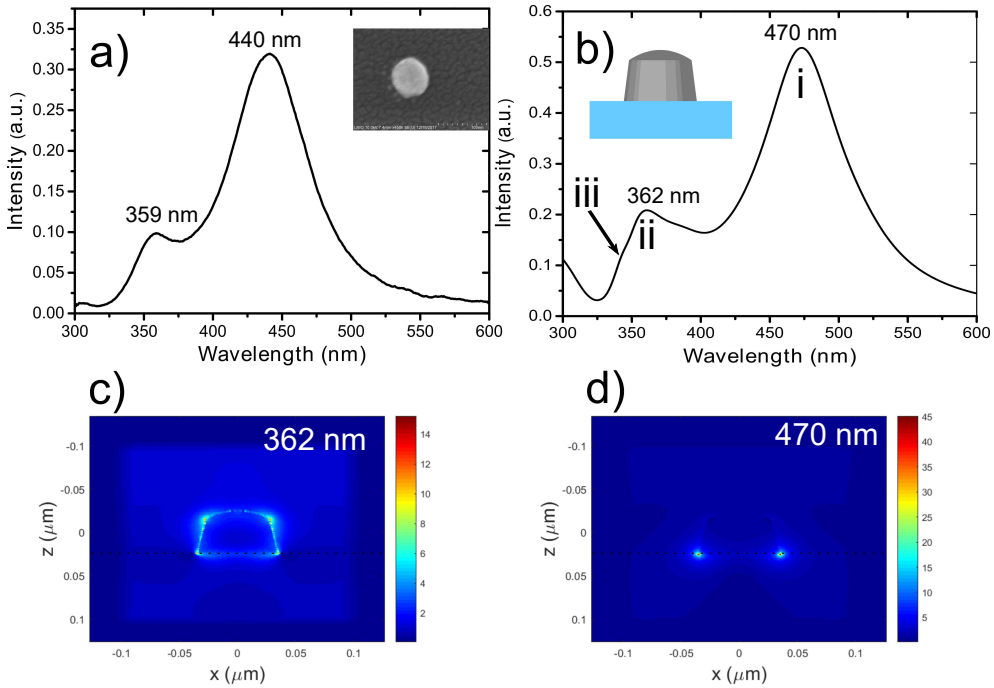

FIGURE 5.5: (a) Experimental extinction spectrum of 70 nm diameter silver nanocylinder deposited on a glass substrate, (b) corresponding simulation. Electric field maps: XZ cut profile in the center of nanocylinder. Illumination is along z-axis from top side and polarized along x axis. Black dash line shows the substrate surface. EF map at (c) 362 nm, (d) 470 nm

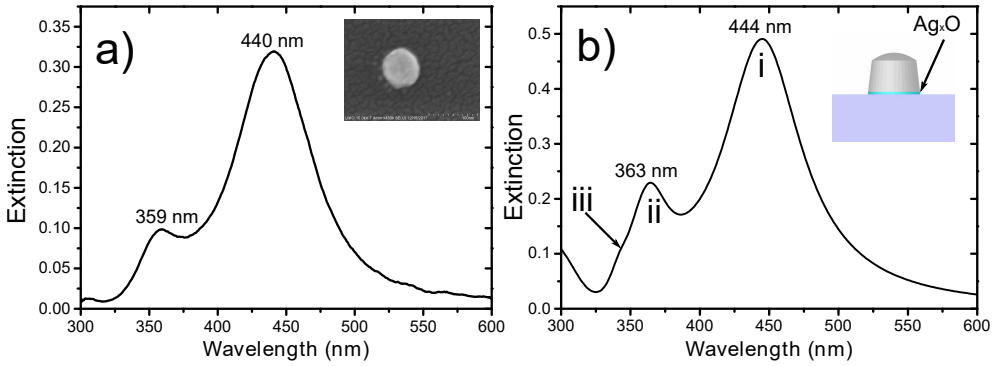

FIGURE 5.6: (a) Experimental extinction spectrum of 70 nm diameter silver nanocylinder deposited on a glass substrate, (b) Corresponding simulation, where there is an intermediate silver oxide layer as shown on the inset. The refractive index is retrieved from Ref. [96]

5.4 LSPR of perfect sphere on a substrate

5.4.1 Introduction

The optical properties of colloidal gold nanospheres find a wide use in enhanced spectroscopies due to their distinguished plasmonic features and affordable fabrication

process. Usually they are characterized with a use of extinction spectroscopy measurements in colloidal solution or in the dense plasmonic films deposited on a substrate. These kinds of measurements do not give insight to the plasmonic resonance of the individual spheres in the system. It gives an average signal of the system of the nanospheres where all of them have slightly different diameter and shape due to their chemical nature. The substrate measurements are in the same time affected by the interparticle interactions and aggregation. Also, as we have seen in the previous part of the chapter, substrate changes the symmetry of the system and induce further spectrum change. Other point is that, due to the nanosphere imperfections they may have different area of contact with the substrate. The proposed previously approach to measure the extinction spectra of the rarefied ensemble to understand the one nanoparticle properties is valid only for the monodispersed systems [98]. Then we can conclude that the only approach to clarify the intrinsic properties of the nanospheres and determine a single nanosphere LSPR is to characterize each nanosphere separately.

Indeed, nanospheres is one of the most studied plasmonic objects. Its modes in a homogeneous medium were discussed firstly by Mie. We decide to check if the substrate has the influence on it. The numerical simulations help to compare LSPRs of nanospheres placed in air and on the substrate. The gold nanospheres for experiments are prepared by Dr. Sylvie Marguet (Université Paris-Saclay) deposited on ITO substrates. Their diameters vary from 125-220 nm.

5.4.2 Simulations: single nanosphere characterization

We present the calculated extinction and reflection scattering spectra of a gold nanosphere (GNS) in air and on an ITO substrate in Fig. 5.7. The extinction spectrum represents the sum of the optical losses, due to absorption and scattering. We chose a perfect GNS deposited on the substrate. The local refractive index usually has the impact on the LSPR position, but comparing the extinction spectra in the Fig. 5.7a and 5.7b one may notice only a minor shift (3 nm) of the main mode in the presence of the ITO substrate. The redshift of the resonance position depends strongly on the area of the contact between the plasmonic particle and the substrate. Since, the GNS has only one touching point, we do not see an obvious redshift (from 594 nm to 597 nm) of the dipolar mode peak position. The main change comes from the peak shoulder around 540 nm on the Fig. 5.7b, which may announce a new mode.

The Fig. 5.7c and 5.7d show the calculated reflection scattering spectra of GNS respectively in air and on the ITO substrate. The calculation of the scattering spectrum for a single nanosphere placed in air shows a broad single peak (Fig 5.7c). In the case of the substrate presence the shoulder appears at 540 nm. The similar behavior for

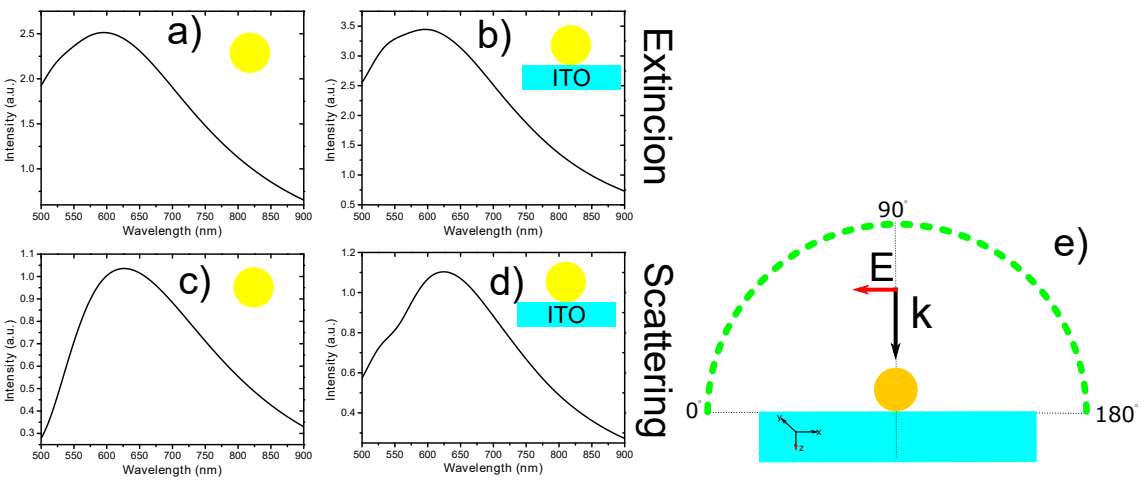

FIGURE 5.7: a) Simulated extinction spectrum of GNS of 199 nm-diameter placed in air. b) Simulated extinction spectrum of GNS of 199 nm-diameter deposited on a ITO substrate. (c) Simulated backward scattering (reflection geometry) spectrum of GNS of 199 nm-diameter placed in air. (d) Simulated backward scattering (reflection geometry) spectrum of GNS of 199 nm-diameter deposited on a ITO substrate. (e) Scheme of illumination and the reflection geometry of collection (green dash line)

the plasmonic nanospheres was reported previously [80]. As we discussed in previous section, the substrate breaks the symmetry of the system and may cause a coupling between dipolar and dark quadrupole modes if they are overlapped spectrally. Due to the hybridization, the plasmonic modes change their spectral/energy position. We have done the same calculations for a gold nanosphere deposited on a glass substrate, and the scattering spectra show only single peak as for in air. A higher ITO refractive index than glass amplifies coupling to the substrate and a higher spectral separation between dipolar and quadrupolar modes due to dielectric screening effect.

5.4.3 Experiments: Reflection and Transmission Geometries

Previously, Y. Fu et al. experimentally demonstrated a directional light scattering by spherical silicon nanoparticles in the visible spectral range [76]. They showed a difference between far-field radiation patterns for reflection and transmission collection geometry. Also, they show the spectral differences for both collection geometries. Dielectric nanoparticles may exhibit electric resonant modes but also magnetic resonant modes in contrast to metallic nanoparticles. A simultaneous excitation and surface mediated mutual interference of these magnetic and electric resonances inside a single dielectric nanosphere cause the spectral asymmetry for different collection geometries. Herein, we demonstrate different radiation patterns for reflection and transmission geometry for metallic GNS.

The experimental DF scattering reflection spectrum of a GNS is depicted on the Fig. 5.8a and the Fig 5.8b shows the corresponding numerical simulation. We observe nicely the separation of two modes on the scattering spectrum for the reflection collection geometry. The modes are noted as D′ and Q′. One may notice a good agreement between simulation and experiment. This proves that the GNS has one contact point as the simulations are performed for a GNS with one contact point with the substrate. The Fig. 5.8e shows the scheme of the two different collection geometries. The green dashed semi-circle shows reflection geometry and the red is transmission geometry.

We show the experimental forward DF scattering spectrum in Fig. 5.8c. There is no defined separation of modes. We see only one broad peak. The simulation for transmission collection geometry is presented in the Fig 5.8d. Here, we see an asymmetry of the left and right slopes of the scattering spectrum. Nevertheless, we observe only one peak position and it is blue-shifted respectively to the reflection geometry scattering spectrum (simulation in Fig. 5.8c). For transmission geometry the peak positions of experimental and simulated spectra (Fig. 5.8c and 5.8d) are not matching, as for simulation we were not able to use the same illumination conditions. The corresponding simulations demand huge computational power. Indeed here, we used plane wave excitation for the simulations. We assume that Q′ mode has a stronger contribution on the scattering spectrum in transmission geometry (Fig. 5.8(c,d)) than in the reflection geometry ((Fig. 5.8(a,b)). Therefore, the spectral overlapping of the mode Q′ and D′ for transmission geometry do not let a separation of the modes, and it seems we have a blue-shift of mode D′. In fact, this effect is due to the strong radiativity of mode Q′ in transmission geometry.

5.4.4 Far field and near field

To understand the nature of the two hybridized modes (D′ and Q′) we did far-field maps in k-space (Fourier space) for reflection geometry. The Fig. 5.9a and 5.9b show k-space images respectively for the mode D′ and the mode Q′. The mode D′ shows a dipole-like character as the radiation is similar to the dipole radiation pattern, when it has a form of a projected donut. The mode Q′ has a quadrupole-like character as it has two lobes on the edges on the radiation pattern. As it is a hybridized mode and spectrally close to the dipolar mode the radiation pattern of mode Q′ does not show pure quadrupole radiation pattern. We justify that the mode D′ originates from a dipolar mode and the mode Q′ from a quadrupolar mode. The electric near-field maps of mode D′ and mode Q′ are shown respectively in the Fig. 5.9c and 5.9d. One may notice that the Mode Q′ does not have quadrupole mode like distribution of the

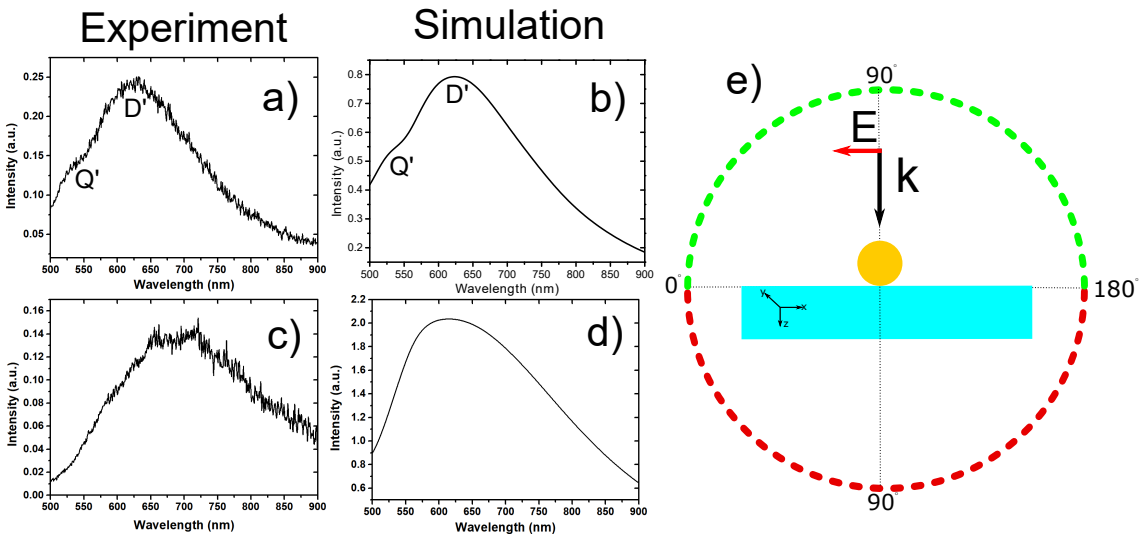

FIGURE 5.8: (a) Scattering spectrum of gold 199 nm-diameter nanosphere, the collection is in reflection geometry, and the numerical aperture is 0.8, (b) corresponding numerical simulation, the numerical aperture is applied on the simulated spectrum. (c) Experimental scattering spectrum for transmission collection geometry. The illumination is done by an evanescent wave using the oil immersion, d) corresponding numerical simulation using plane wave excitation. (e) Schematic of reflection and collection geometry, the green semicircle shows the reflection geometry and the red shows transmission geometry

field. The mode Q' and D' have a spatial overlapping, while the mode Q' has a higher confinement of the field between the substrate and the GNS than the mode D'.

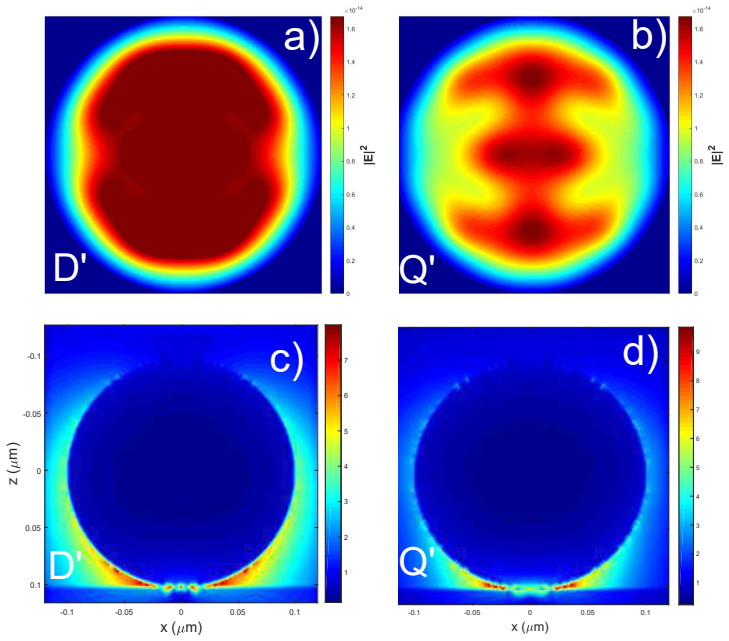

FIGURE 5.9: (a) Calculated far-field map for 625nm excitation of the 199 nm-diamater GNS and for (b) for 545 nm excitation of the 199 nm-diamater GNS. (c) Calculated near field electric field map for 625 nm excitation and (d) for 545 nm excitation

5.4.5 Effect of the substrate touching area

We present the scattering spectra for different GNS sizes in the Fig. 5.10. The main goal is to show the influence of the contact point on the scattering spectra.

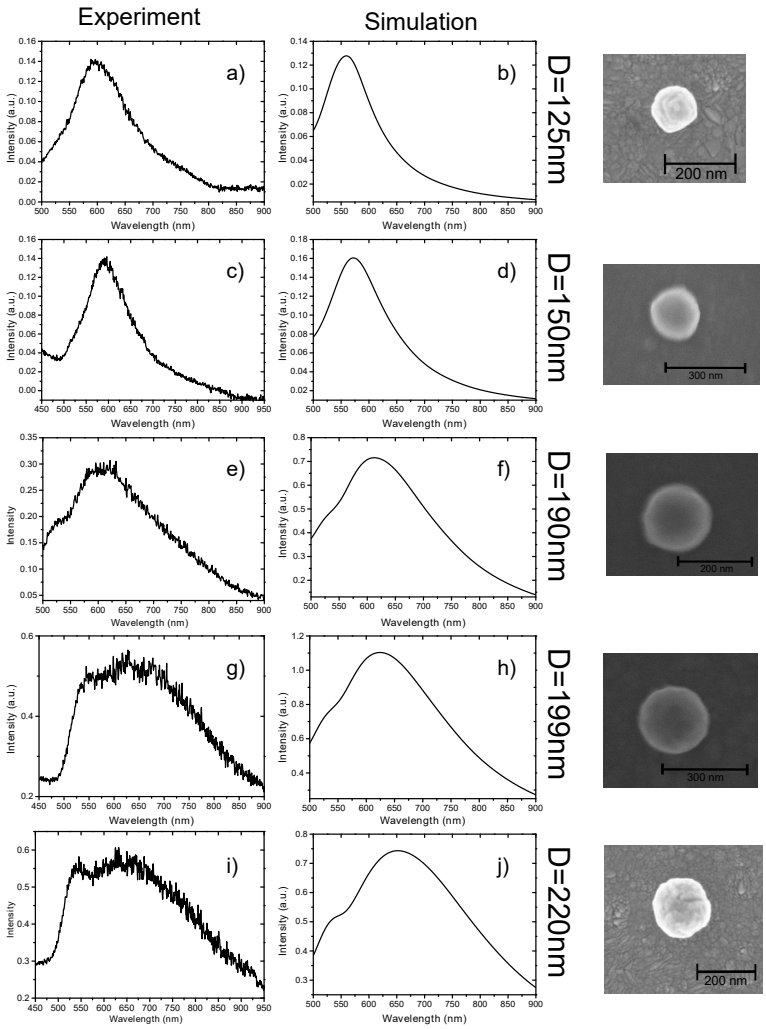

FIGURE 5.10: (a-j) Experiments and simulations of a single GNS with different diameter (D). The diameters of spheres was measured by scanning electron beam microscope.

One may observe that some of the experimental spectra match with simulated spectra like the spectra for D=190 nm and D=150 nm. As we have a set of nanoparticles of very close sizes it is possible to check the reproducibility and deposition peculiarities. Some of the measurements for the 199 nm NSP show results very close to the simulated spectra, some of them have different form. Previously, we demonstrated that a GNS of 199 nm-diameter shows a perfect match with simulations, unlike another GNS of 199 nm-diameter (Fig. 5.10g and 5.10h). The same image we have for D=220 nm (Fig. 5.10i and 5.10j). We assume that for these GNSs the contact area between the substrate and GNS is not a point.

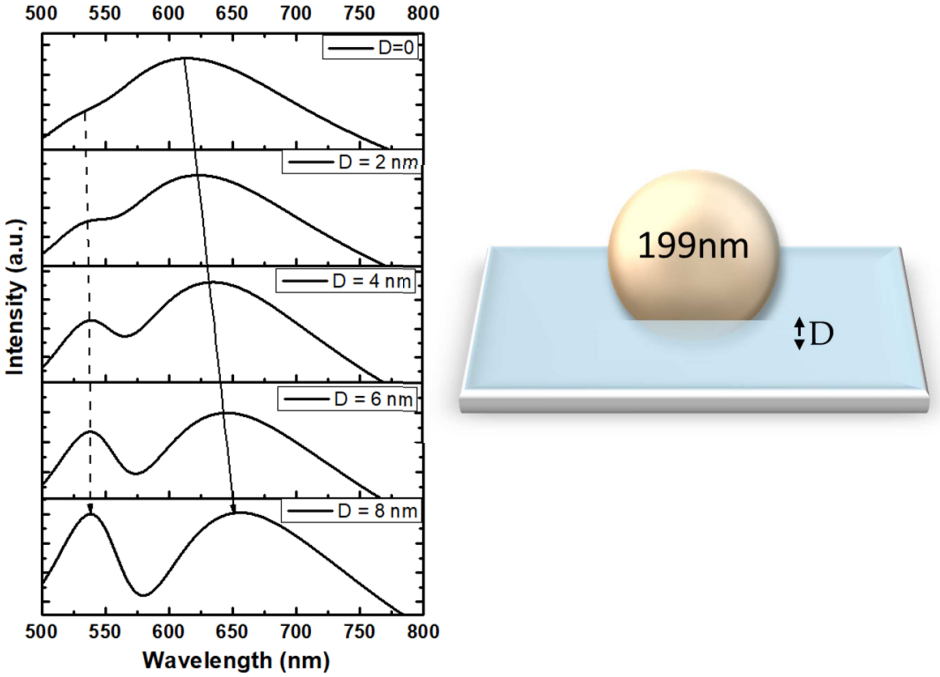

FIGURE 5.11: Simulations of a GNS buried in glass D distance. The GNS diameter is 199 nm.

To understand the effect of the touching area on the substrate we calculated the scattering spectra for GNS of 199 nm-diameter for different touching areas. The calculations are done for a GNS which we bury into the glass (Fig. 5.11) for different depths. With the increase of burring depth, the touching area increases and strengthens the redshift of the hybridized dipolar mode (D'), but not of the hybridized quadrupolar mode (Q'). Why Q' is thus not redshifted? A GNS in air has Dipolar (D) and Quadrupolar (Q) modes. Due to coupling with the substrate the modes are hybridized and coupled into Q' and D' modes. We can represent the new modes by the difference of the energy (anti-bonding) of air modes Q'=Q-D or by the sum of the energy (bonding) of the air modes D'=Q+D. The scheme and the short description of the anti-bonding and bonding modes are explained in the Fig. 5.12. When we change the touching area between substrate the effective refractive index around the GNS is changed. In this manner the mode D and mode Q are redshifted. The mode D' is the sum of the redshifted D and Q modes, which means D' will be redshifted depending on the effective refractive index change surrounding the GNS. As the mode Q' is the difference between the redshifted D and Q modes, Q' will not be redshifted or very small shifted because of the effective refractive index. One may also observe the increase contribution of Q' mode with the increase of the touching area in Fig. **??**. We see the contribution of mode Q' is higher for spectrum in Fig. 5.8g than in Fig. 5.8a, although the GNSs have the same diameters. One may conclude that the touching area for GNS of Fig. 5.8g is bigger than a point. Nevertheless, we were not able to recover completely the spectrum of Fig. 5.8g as we

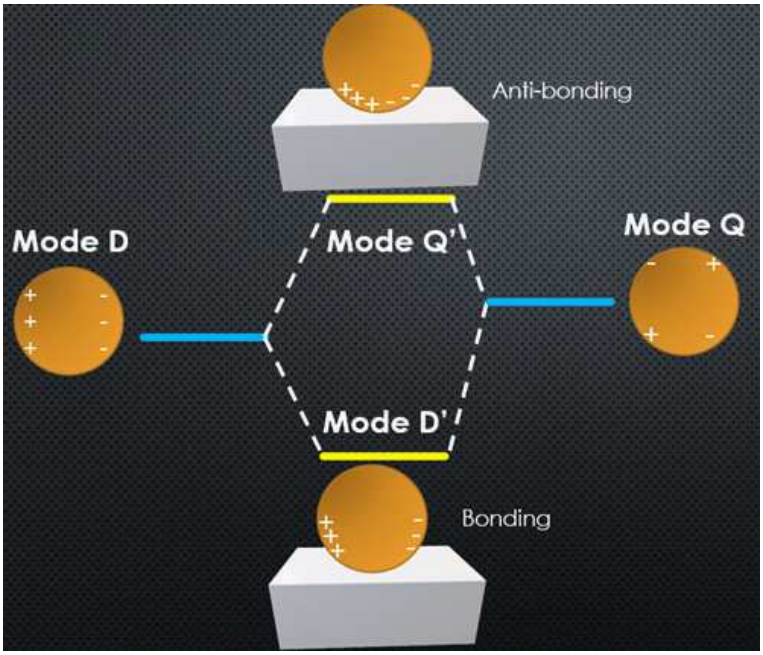

FIGURE 5.12: Illustration of the scheme of the hybridization and the coupling of the dipolar (D) and the quadrupolar mode (Q). The substrate creates a symmetry breaking of the plasmonic system and it result in the coupled modes of lower energy (bonding-D') and higher energy (anti-bonding – Q')

do not know the exact profile of this GNS and the shape of the contact on the substrate.

5.5 Nanostructure symmetry breaking

We have presented the spectrum of the pyramid in Chapter 2, here we discuss the its LSPRs nature. Herein, the Fig. 5.13 presents the extinction spectra of a parallelepiped which transforms to a pyramid. The parallelepiped has a single peak on the extinction spectrum, which we attribute to the dipolar mode. When we start to change the symmetry by reducing the top plane size, the extinction spectrum shows a symmetry breaking on the left slope of the peak (parallelepiped $100x70x50nm^2$).

With the increase of the dimension difference between the bottom plane and the top plane of the truncated pyramid, the dipolar mode is redshifted and the it is formed a new mode (shoulder noted by red dashed line). And finally, the pyramid shows a defined peak at 560 nm instead of the shoulder. In order to identify the nature of these two plasmonic modes located at 560 nm and 640 nm we calcuated their charges distribution. Fig. 5.14a shows the charges distribution of an excitation at 560 nm. One may not that there is dipole distribution on two opposite faces, while on the edges of the faces we notice the quadupolar mode distribution. Remind, that the plasmons are surface waves and the geometrical lengths of surface are important. The height

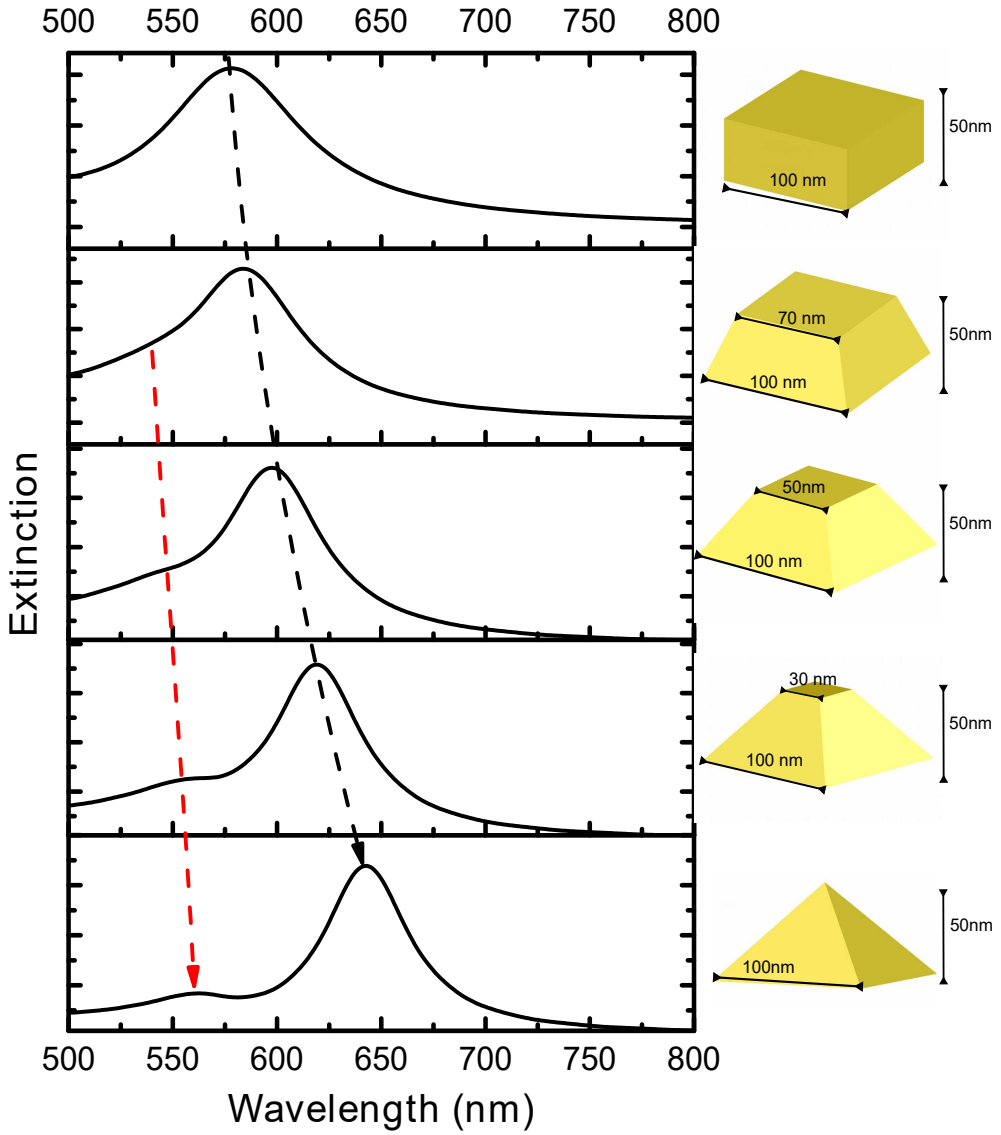

FIGURE 5.13: Extinction spectra of a parallelepiped transforming to the pyramid

length of parallelepiped is parametric of side faces surface, while the height of the pyramid does not identify the surface of the faces and geometrical length of the faces. For the pyramid the parametric length of the faces is the edges length. Comparing the geometrical lengths of the parallelepiped height and the pyramid edges length we can notice that for pyramid the parametic length is longer. With increase of the length of edges we excite the quadrupolar mode on the edges due to retardation effect, while on the faces we have dipolar mode distribution.

Fig. 5.14b shows the charges distribution for 640 nm excitation. We also see hybrid mode of quadrupolar on the edges and dipolar mode on the face like Fig. 5.14b. Herein, there is a stronger highlighted dipolar distribution not only on the edge, also on the middle of the baselines.

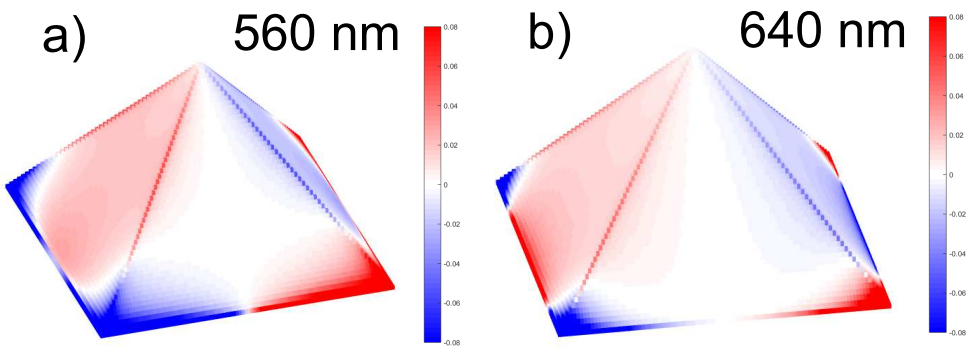

FIGURE 5.14: Charges distribution the pyramid for the excitation at (a) 560 nm and (b) 640 nm.

5.6 Conclusion

We thoroughly studied the effect of the intrinsic plasmonics modes hybridization induced by the changing of the system symmetry for nanoparticles of different shapes. The hybridized modes have different properties and behaviors which can be explained with a help of the hybridization model.

We showed first experimental demonstration of the hybridized quadrupolar mode of a single nanocylinder. Moreover, by simulation we demonstrated an excitation of two quadrupolar modes having different nature such as hybridized and non-hybridized for a silver nanocylinder. Indeed, the hybridized quadrupolar mode is not sensitive to the refractive index changes, how long it is excited.

We demonstrated experimentally and numerically the effect of the touching area between nanospheres and the substrate. The dipolar mode of perfect GNS shows same spectral position when it is placed in air and on the substrate. We showed that directional spectroscopy, like reflection scattering, can scope plasmonic modes, which are not seen with the extinction spectroscopy. Moreover, the simulations showed that scattering spectra are different for different collection geometries due to the unequal contribution of hybridized plasmonic modes for each collection geometry.

Besides the symmetry breaking by a substrate, it is possible to obtain hybridized multipolar modes by breaking the symmetry of the nanostructure itself. We showed an example of the hybridization of a quadrupolar mode of the gold pyramid.

"Solar power is clean, renewable and cost effective, but it also needs time to develop."

J. D. Hayworth

6 Doubly resonant surface enhanced fluorescence

6.1 Introduction

The fluorescence is a light emission process when the fluorescent object absorbs the photon of the incident light and afterwards emits the photon of the same spin state. The fluorescent dye is usually a molecule or a semiconductor nanostructure. Since its exploration the fluorescence finds a wide area of applications in sensing and light emitting devices.

Fluorescence emission is one of the processes relaxing a system after a photon absorption together with the phosphorescence or the non-radiative relaxation. The Jablonski diagram helps to understand the process of fluorescence. The Stokes' law states that the energy of the emitted photon is lower than its excitation energy, due to the fast internal relaxation processes. Then, the emission of a single photon is induced by the absorption of a photon of higher energy. However, simultaneous absorption of the two and more photons if their energy together is higher than fluorescence energy can induce fluorescence. The fluorescence excitation by single and two photons are shown in the Fig. 6.1. Since this non-linear process depends on the simultaneous absorption of two photons, then the probability of two-photon absorption by a fluorescent molecule is a quadratic function of the excitation intensity. It is possible to achieve

two or more photons excitation using an intense laser.

Semiconductor quantum dots are widely used as light sources due to their convenient emitting properties such as size-dependent fluorescence, wide absorption band, high stability and quantum yield. However, QDs have small collection efficiency as they emit to all directions.

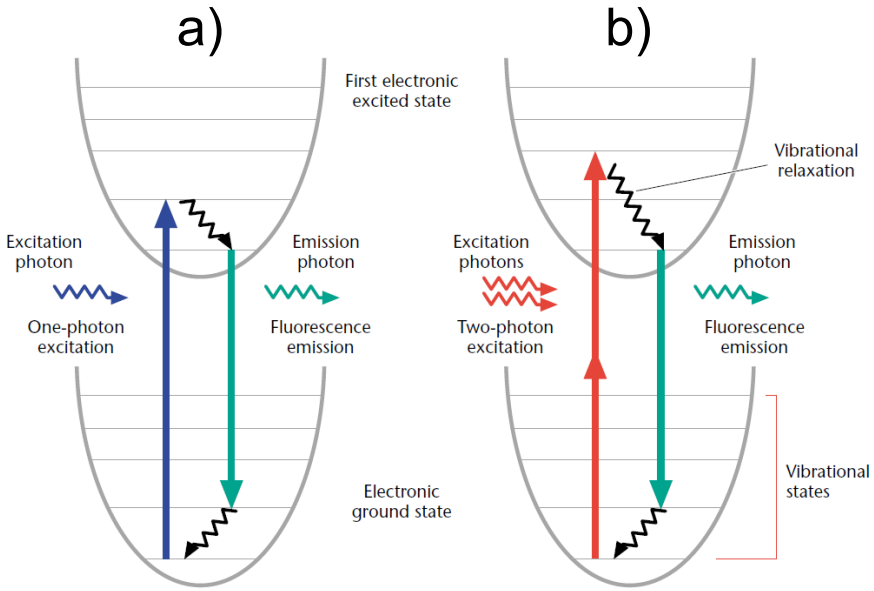

FIGURE 6.1: (a) Jablonski diagram of one-photon (a) and two-photon (b) excitation, which occurs as fluorophores are excited from the ground state to the first electronic states. One-photon excitation occurs through the absorption of a single photon [99]. Two-photon excitation occurs through the absorption of two lower-energy photons. After either excitation process, the fluorophore relaxes to the lowest energy level of the first excited electronic states via vibrational processes. The subsequent fluorescence emission process for both relaxation modes is the same.

A plasmonic structure can be coupled to a fluorescent substance in order to enhance its emission [20, 47, 48, 100–103]. The presence of a plasmonic structure in the vicinity of QDs induce several processes. Three main effects are [104]:

1. A plasmonic structure exhibiting resonant excitation has enhanced electric field at near-field. A QD located in these positions increases its excitation rate.

2. The particle may act as an optical resonator by increasing the relaxation rates in a QD. This may lead to the increased emission rate. Note, this works when the emission wavelength is at the resonant position of plasmonic nanoparticle.

3. A plasmonic nanoparticle may increase the coupling between the far-field and the near-field, giving directionality to emitted light or confine the light at the vicinity

of the plasmonic nanoparticle. This depends on the plasmonic mode nature. When the plasmonic mode is non-radiative the nanoparticle will mostly absorb the light.

The total enhancement of QDs emission depends only on the enhancement of excitation and emission rates. However, from the experimental point of view the detection of the emitted light is very important. The enhancement factor of QD is usually presented as a multiplication of the excitation rate enhancement, emission rate enhancement and the collection efficiency [105, 106].

$$\eta_{tot} = \eta_{exc} \cdot \eta_{em} \cdot \eta_{col} \tag{6.1}$$

where η_{exc} is the excitation rate enhancement, η_{em} is th emission rate enhancement and η_{col} is the collection efficiency.

Liu et al. used two plasmonic modes of gold nanorods in simultaneous excitation and emission enhancements in single photon fluorescence [107]. Particularly the wavelength of the plasmonic mode assisted by an electric field oscillation along short axis matches with the excitation wavelength of the fluorophore and the wavelength of the plasmonic mode excited along long axis matches with emission wavelength of the fluorophore. In this case the electric field confinement of each plasmonic mode are not overlapped, which means that some fluorophores emissions are enhanced at excitation process and some in emission process. Simply, the fluorophore located in the vicinity of the electric field of the dipolar mode of short axis benefit from the excitation rate enhancement, and the fluorophores located in the vicinity of the electric field of the dipolar mode of the long axis benefit from an emission rate enhancement. Later, Liu et al. showed a theoretical calculation of the up-conversion enhanced fluorescence using plasmonic double-resonant gold nanorods, where they considered the dipolar mode of a nanorod for the enhancement of the excitation and the quadrupolar mode for the enhancement of the emission rates of fluorophore [108]. Herein, the calculations showed that these two plasmonic modes have significant spatial overlap which can enhance the same fluorophores in both processes such as excitation and emission. Howerer, it has not been shown experimentally before.

A strong enhancement of QDs emission can be achieved using a multi-resonant system. We showed in Chapter 4 that a nanocylinder can be a multi-resonant system. The idea of this chapter is to couple one plasmonic mode of the nanocylinder with the excitation of QD and another mode with the QD emission

6.2 Experimental method

We produce a GNC array on a glass substrate. The GNC diameter is 170 nm and the height is 50 nm. The inter-particle distance is $1\mu m$. The sample is covered with 8-10 nm silica layer in order to process a surface functionalization. The substrate is incubated into a 3,3-mercaptopropyl trimethoxysilane (Sigma-Aldrich, 95%) in anhydrous toluene at 0.01 % for 12 hours. Hence, the substrate is immersed in a solution of QDs diluted in toluene (0.08 g/L) for 24 hours [109]. We used core-shell CdSe/ZnS quantum dots with an emission peak at 610 nm. Its average diameter is 8 nm. A monolayer of QDs is obtained through the silanization process, as the QDs are bounded covalently to the silica layer. In this manner we have a mono-layer of QDs on the substrate.

The photoluminescence measurements have been performed at the University of Tübingen in the group of Pr. Monika Fleischer and in the group of Dr. Dai Zhang. The single photon photoluminescence (PL) measurements are performed with the help of a commercial microscope (Eclipse Ti2 from Nikon) equipped with a cooled ($-39°C$) spectrograph from Andor Technology. We illustrate the schematic of the experimental setup of PL in Fig. 6.2. We used a pinhole of $50\mu m$ diameter, which corresponds to a disk of collection of 500 nm-diameter.

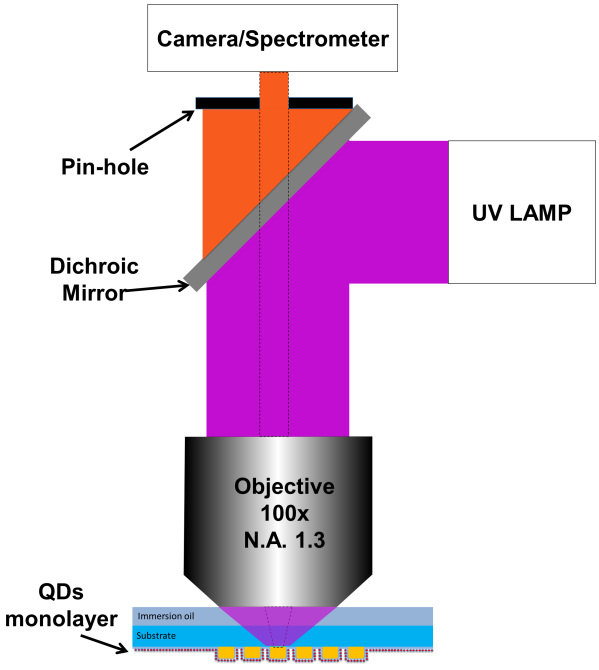

FIGURE 6.2: Scheme of the experimental setup for PL measurements. The UV lamp focused through an oil immersion objective excites the QDs coated on the glass substrate. The same objective is used to collect the PL signal using a Dichroic mirror, which blocks the illumination wavelengths (below 520 nm). A pinhole is used to spatially filter the collection zone.

Two photon fluorescence setup equipped with parabolic mirror is shown on the

Fig. 6.3. The advantage of parabolic mirror is a high collection numerical aperture (N.A=0.996) and a chromatic-free focusing. We use a femtosecond erbium fiber laser (774 nm) beam for the sample excitation either linearly polarized either radially or azimuthally polarized converted by a home-built mode converter. The laser output power was measured as 42mW. We used a neutral density filter with an optical density (O.D.) of 1.5, which corresponds to 3 percent (1.42mW) of total power. Note, this power is decreased at focus because of the multiple lenses and the sample holder. The idea of using this filter is to avoid intrinsic photoluminescence of gold, which needs a strong power to be observed. Furthermore, in this manner we avoid the saturation of QDs. The laser beam was focused on the sample in a reflection mode, and the emitted light from the sample was collected by the parabolic mirror under angles from 28 to 85 degrees. A short pass filter (Semrock FF01-680/SP.) excludes the collection of the excitation wavelength letting pass wavelengths from 350 to 680 nm to the APD for photon counting imaging or to the thermo-electrically cooled charge-coupled device (CCD) camera coupled to a spectrograph. All spectra were obtained using a spectrometer grating with 150 grooves per mm. The sample displacement was carried out by a piezo stage. The images taken by the APD presents a scanned map obtained point by point. In other words, we focus the laser beam on a point on the sample and the collected intensity is recorded in one pixel then draw the image pixel by pixel.

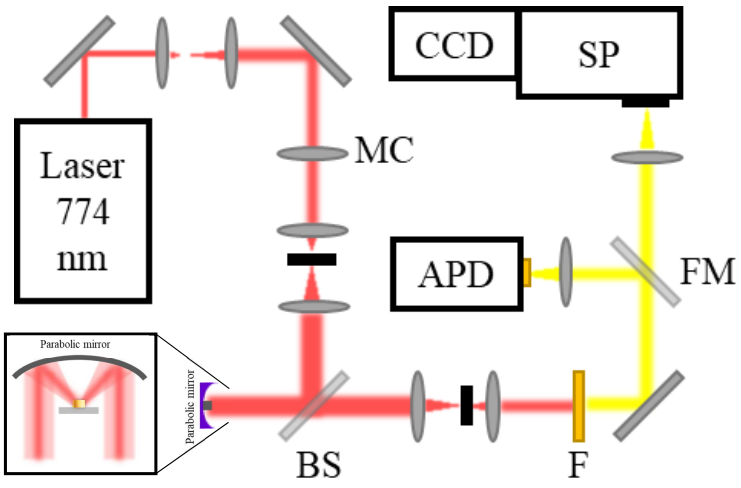

FIGURE 6.3: Schematic setup of the parabolic mirror assisted confocal microscope. The laser beam linearly polarized focused with the parabolic mirror (PM) onto the sample. The signal is collected by the mirror under angles between 28 and 85 degrees. A beam splitter (BS) and a filter (F) separate the signal from the excitation light. Using a flipping mirror (FM) the signal can be directed to either an avalanche photo diode (APD) or a spectrometer (SP) with a cooled CCD-camera. The laser beam polarization can be converted to a radial or azimuthal mode by a liquid crystal mode converter (MC).

6.3 One-photon photoluminescence

Before to study a system of QDs coupled with two resonances of a plasmonic nanostructure, we decided to study a single resonance enhancement process. In this case we want to enhance the emission process of QDs. Our core-shell CdSe/ZnS quantum dots under study have a wide absorption band down to UV and the emission peak at 610 nm. Firstly, we study the one-photon photoluminescence (PL) emission of the QDs monolayer and the intensity enhancement obtained on the plasmonic nanoparticles. The UV lamp effectively excite the QD but does not excite the plasmonic resonance of the gold nanoparticle (for this wavelength the gold is not resonant due to strong inter-band transitions). Then we can state that we have the plasmon-QD interaction connected only with emission of the quantum dots. In this manner we exclude the enhancement on the excitation.

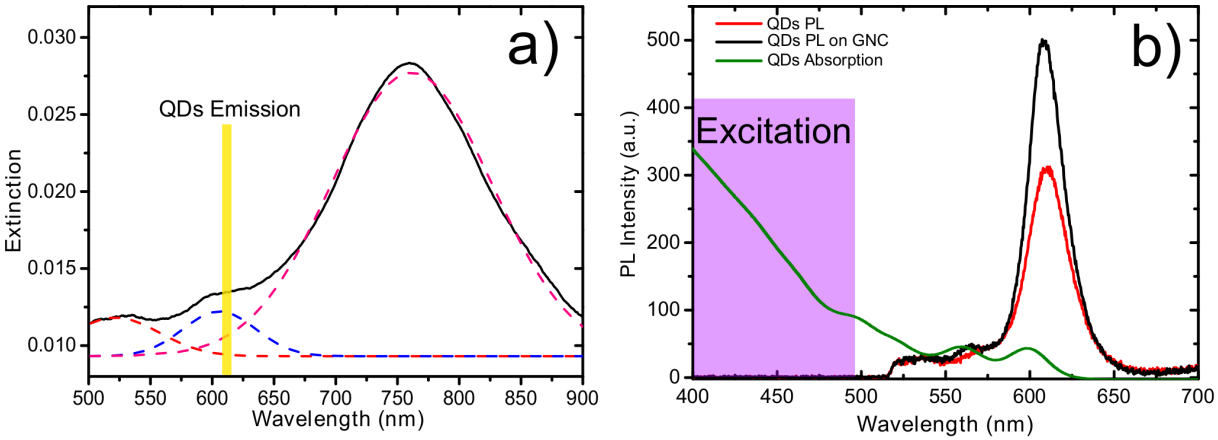

FIGURE 6.4: (a) Extinction spectrum of 170-diameter GNC excited using a tilted (50 degrees) illumination. The Quantum dots emission is matched with quadrupolar mode. (b) Single photon fluorescence of QDs coupled to a single GNC of 170 nm-diameter. The excitation is performed by uv lamp.

The Fig. 6.4a shows the extinction spectrum of GNCs of 170 nm-diameter thoroughly studied in Chapter 4. The chosen structure exhibits a quadrupolar mode peaked at 605 nm (fitted by blue dashed curve), which almost matches with the emission wavelength of the QDs. In fig. 6.4b we present the relative PL of QDs uncoupled and coupled to the 170 nm-diameter GNC. The red curve shows the PL signal of free QDs and the black curve shows the PL signal of QDs linked to the GNC. Also we show the absorption spectrum of the QD. One may note that the Stockes shift (difference of absorption and emission peaks) of the QD is extremely small. We obtain an enhancement factor of 1.6 times. We have shown previously that the quadrupolar mode for the nanocylinder of this size is excited near the 600 nm, then we claim that the QD emission is coupled to the quadrupolar mode of GNC. We should note that in our system the plasmonic nanoparticle is excited only by QDs. We have to assumptions:

1. The near-field of QDs can possibly induce the excitation of the quadrupolar mode of GNC. The quadrupolar mode is usually non-radiative, which may result in quenching of the photoluminescence instead of the enhancement. Previously, we showed the existence of the quadrupole-like mode which is radiative. Therefore, one may assume that it can enhanced the emission of QDs.

2. When QDs excite a plasmonic mode of the GNC, a strong electric field is confined at the vicinity of GNC. We should also underline that this near-field of the GNC may excite QDs by direct transition without vibrational relaxation due to the small Stockes shift [110]. Simply to say, the QDs absorbs at its emission wavelength.

In order to prove the first assumption we did preliminary calculations of the radiative decay rate of a dipole coupled with a GNC. The spectra are normalized by source power, which means the the radiative decay rate shows the enhancement of the radiation of the source by a nanostructure. The spectrum is averaged taking into account the dipole orientation in three directions of space. The normalized radiative decay rate shows the ratio between the emission of emitter coupled with a nanostructure and without.

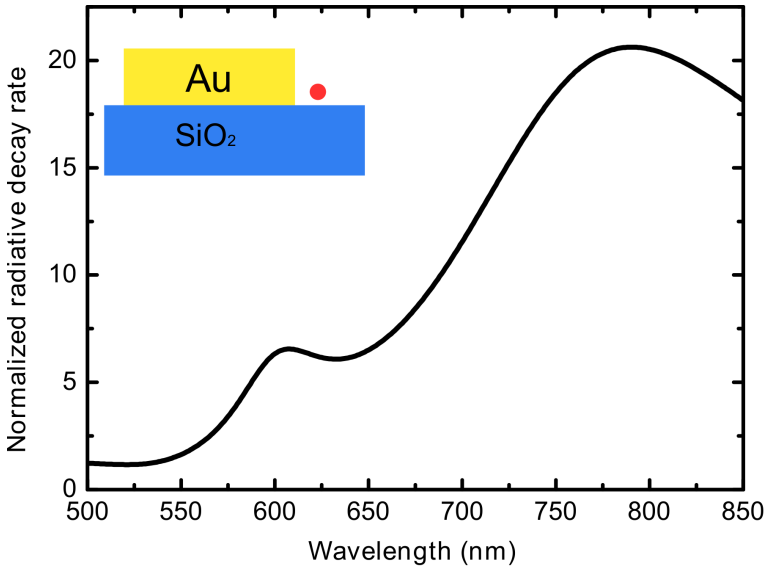

FIGURE 6.5: Calculated normalized and averaged radiative decay rate for 170 nm-diameter and 50 nm-height GNC. In the inset is shown schematic of dipole disposition respected to the particle. The calculation summarize the average of the radiative decay rates for three orientations of the dipole.

Simply, it shows how many times the emission is increased due to the nanostructure. Indeed, the first assumption is true as we clearly see that there is a well pronounced peak around 600 nm. This confirms that the emitter can couple to the nanocylinder resulting in an enhancement of the emission rate due to quadrupolar mode.

6.4 Two-photon photoluminescence

6.4.1 Linear polarization

In this section, we aim to achieve a doubly resonant enhanced TPPL of QDs. As we mentioned previously QD has an emission maximum at 610 nm and we excite the TPPL at 774 nm which corresponds to the plasmon peaks for the GNC. The Fig. 6.6a presents the plasmonic modes (extinction spectrum) of GNCs, where the laser excitation and QDs emission wavelengths are depicted also.

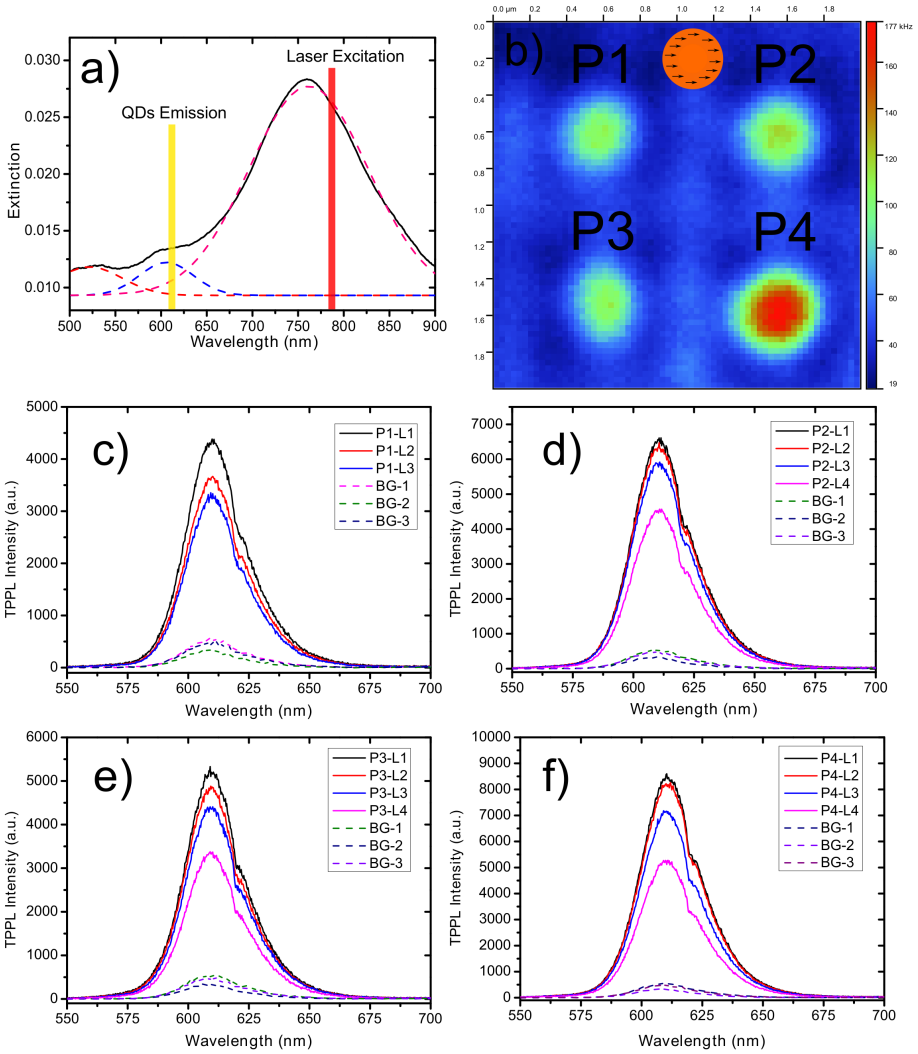

FIGURE 6.6: (a) The excitation and the emission wavelengths are drawn on the extinction spectrum of 170 nm-diameter and 50 nm-height nanocylinders. (b)TPPL scanned map of the array of 170 nm-diameter array. The polarization is linear. (c-f) TPPL spectra for each GNC (P1-P4), the solid curves present the TPPL spectra when the laser focuses from the center to the edge of the GNCs. The dashed line curves shows TPPL spectra out of the array.

The excitation wavelength matches with the dipolar mode and the emission wavelength with the quadrupolar mode. We present the scanned map of TPPL of a section of 2x2 μm^2 on the sample in the Fig. 6.6b. Herein, we observed four nanoparticles labeled as P1 to P4. The highest TPPL signal is P4. From the TPPL map we assume that P4 LSPRs have better match with the excitation/emission wavelengths. Also we do not exclude that this strong TPPL signal from P4 may be due to the accumulation of QDs at the vicinity of the GNC even though that it supposed to be a monolayer.

We think that the difference of TPPL intensities can be due to imperfections of GNC shape and morphology. As a consequence, the P1 and P3 show elliptical elongated form and probably there is a mismatch between the excitation wavelength and the plasmonic mode. The highest intensity of TPPL for each GNC is obtained when the laser beam is focused at the center according to the strong Gaussian beam profile. Indeed, the linear polarization has strong E_x component (polarization direction) at the center of the beam focus [111], which is responsible for the excitation of the horizontal dipolar mode.

In order to compare the enhancement factor of TPPL and PL we take the spectra for each GNC for different positions of the focus. The spectra are shown in Fig. 6.6(c-f). The solid lines show the spectra of the TPPL on GNCs. When the focus is moved from the center to the edge of the GNC, the TPPL signal is decreased because the beam is partly out of the GNC. Furthermore, the excitation at the edge of the GNC can have different excitation efficiency than at the center excitation [70].

We obtain factor of 7.5-25 times enhancement when the laser is focused at the center of GNCs. This enhancement is quite high compared to the single photon PL enhancement that we obtained previously (1.6 times). We attribute this increase to the additional excitation enhancement of the emission in the case of TPPL, as the excitation of TPPL also coincides with the plasmonic mode. Usually, the enhancement factor of photoluminescence strongly depends on the intrinsic quantum yield (QY) of QDs. We think that the intrinsic quantum yield (QY) of QDs may be different for one-photon and two-photon excitations, then enhancement factor will be changed respectively. This can be one of the other possible reason of the additional enhancement that we obtain for TPPL.

Now, the main question is do we have enhancement on the excitation or it is due the QY change?

6.4.2 Radial polarization

We would like to separate the enhancement of the excitation and the emission rates for two-photon excitation. In order to obtain only an enhancement on the emission

of TPPL we need to exclude the enhancement on the excitation process. Indeed, our TPPL setup allows to use a radial polarization, which has strong out-of-plane (vertical) component of electric field and very weak in-plane component in the focus. Then for this kind of excitation, only out-of-plane modes should be active, excluding the main dipolar mode. The peak of the out-of-plane dipolar mode of the 170 nm-diameter and 50 nm-height GNC is around 525 nm and the quadrupolar mode is near 600 nm (Fig. 6.6a), which means that the laser excitation wavelength (774 nm) is not resonant with these modes.

In the same time enhancement in the emission should not depend on the polarization, because it is attributed to the plasmonic modes excitation by the QD emission. Accordingly, the use of the radial polarization should exclude the enhancement of TPPL on the excitation process.

The Fig. 6.7a depicts the scanned TPPL maps of the GNCs (P1-P4) excited by a radially polarized laser beam. The spots have a donut-like shape on the GNCs areas. We record the TPPL spectra for different positions of the focus by moving it from the center of the donut to edge, where the highest signal is obtained (Fig. 6.7a-6.7e).

To understand the results of TPPL map and the spectra recorder at different focus points we need to study the electric field at the focus for a radial polarization. The calculated electric field at the focus, on the substrate, for radial a polarization assisted by parabolic mirror is drawn on Fig. 6.8. When the GNC is placed at the center of the radially focused beam, the GNC (170 nm-diameter) is interacted only with the vertical component of the electric field as it is shown in Fig. 6.8a-6.8c. So, the GNC placed at the center of the focus does not exhibit in-plane dipolar or other in-plane plasmonic modes. Moreover, 774 nm is not resonant for the vertical dipolar mode, which means, the TPPL excitation process is non enhanced due to coupling between QDs excitation and this mode. Thus, if we move the GNC from the center of the focus the GNC faces the in-plane component of the electric field (look Fig. 6.8d-6.8f).

Back to the TPPL map for radial polarization, we can explain, when the focus is at the center of the GNC the enhancement is obtained only for the QDs emission process. While, the GNC placed out of the center of the focus is excited by the in-plane component of the electric field which is resonant for horizontal dipolar mode. In this case we have an enhancement on both processes, i.e., excitation and the emission. For this reason, we have the donut-like shape, when the focus center is out of the GNC the QDs emission and excitation are enhanced, while at the center is enhanced only the emission. Now, if we look the enhancement factor when the radially focused laser beam is focused at the GNC center it varies from 1.7-3 times. Looking back to the PL enhancement which is 1.6 it is in the range of the TPPL enhancement for radially polarized illumination. Of course, the GNC shapes and the collection geometry play a

role in the enhancement factor.

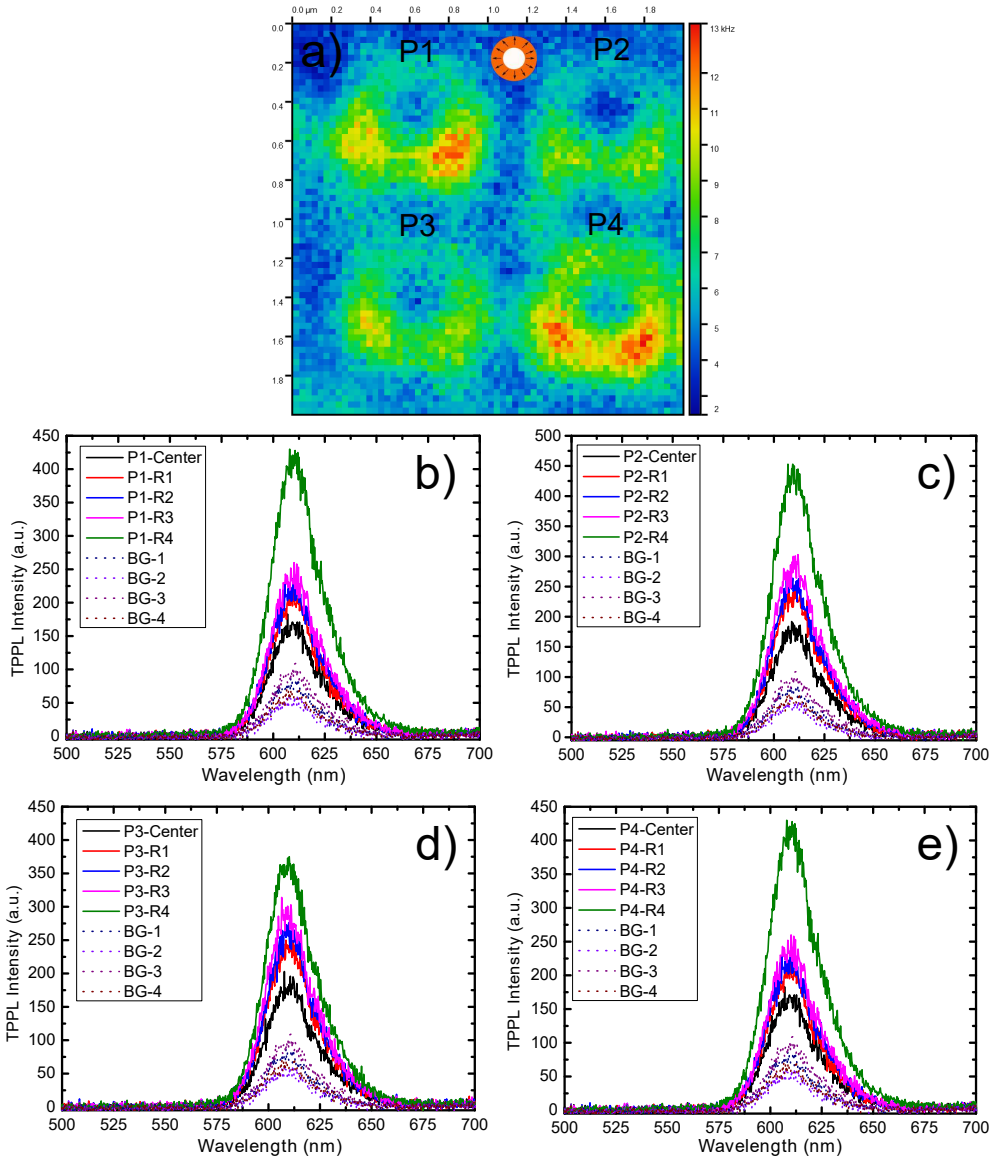

FIGURE 6.7: (a)TPPL scanned map of the array of 170 nm-diameter array. The polarization is radial. (b-e) TPPL spectra for each GNC (P1-P4), the solid curves present the TPPL spectra when the laser focuses from the center to the edge of the GNCs. The dotted line curves shows TPPL spectra out of the array.

Indeed, the TPPL minimal enhancement factor for doubly resonant system was observed 7.5 times while for the single resonant system it was 1.7. And the maximal enhancement factor was observed 25 times for doubly resonant system, while the single resonant system records 3.5 times enhancement factor. But for the doubly coupled systems, the enhancement factor of QDs emission was increased to 4.4-7.5 compared to the single resonant system. However, the main message of this chapter is not estimating the qualitative enhancement factor of TPPL or PL, but demonstrating superiority

of the double resonant system coupled with fluorophore over the single resonant coupling.

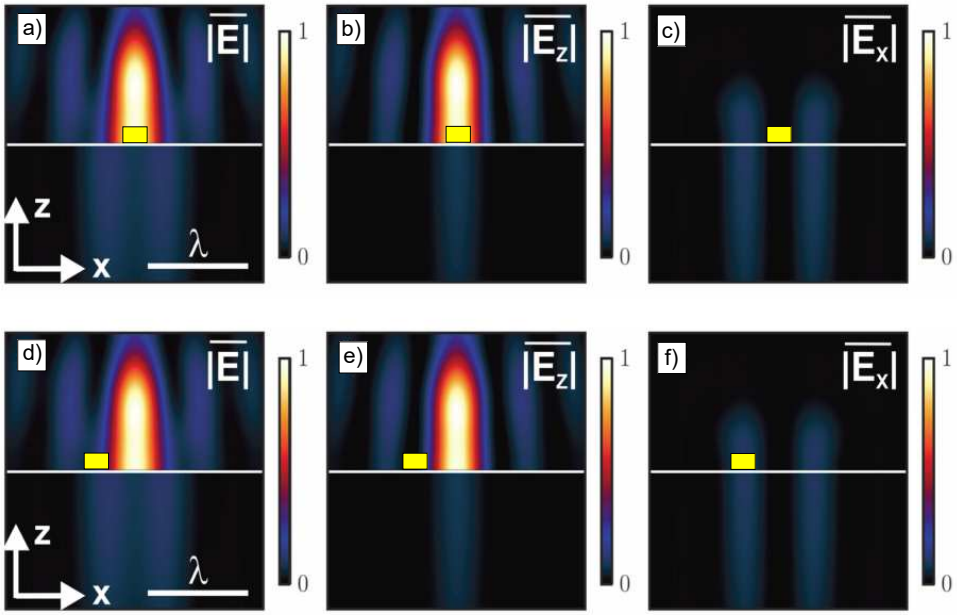

FIGURE 6.8: Calculated electric field distribution of radial polarization at the focus on the substrate achieved by parabolic mirror, (a-c) show the spatial overlap of the electric field magnitude and its components with a GNC place at the center of the focus and (d-f) on the edge. Figures is adopted from Ref. [112]

We show that it is possible effectively to enhance the fluoroscence via coupling with double resonant plasmonic nanoparticle with simple geometry. For better understanding we plan to measure the dimensions of GNC, which may explain better the different intensities on TPPL map shown on Fig. 6.6b. Moreover, we plan to study TPPL of other QDs (emission maximum at 520 nm) which will allow to obtain an emitter coupled with vertical and horizontal dipolar modes.

Conclusion and perspectives

The main goal of the thesis was to explain the principal factors that may influence on the optical spectra/response of plasmonic nanoparticles. The whole thesis investigated and experienced practically all possible reasons affecting on the experimental and numerical spectra. We discussed and explained the impacts of the experimental methods on the spectra and highlighted the importance of the experimental setups components. Furthermore, we proposed two novel approaches to characterize single nano-objects.

Besides the impact of the experimental setups, we studied the influence of the plasmonic system changes itself, such as geometry, shape, refractive index and substrate. The optical spectra change due to symmetry breaking of the system are studied and explained. For example, a substrate may cause hybridization of the modes and changing of their spectral position and spatial disposition of the electric field. Also, we studied the hybridization caused by the nanostructure shape symmetry breaking.

The deep study and the understanding of the optical properties of the gold nanocylinders allows elaborate a doubly resonant system for fluorescence enhancement, on the final step.

In chapter 2 we have shown that asymmetric nanoparticles like nanocylinders, besides dipolar and multipolar modes may sustain out-of-plane (vertical) dipolar mode depending on the illumination conditions. The near field confinement of these two dipolar modes is similar around nanocylinder, while spectrally they are well separated. These two mode can be potentially used in various applications. In contrast to the near field similarities, their far-fields radiation patterns differ dramatically.

We demonstrated the "dark" nature of quadrupolar modes using FDTD simulations. Moreover we showed the importance of the shape on the LSPR control. Finally, we discussed and explained the effect of height-diameter ratios on the LSPR of GNCs. In summary, we showed the ways of tuning of LSPRs and their near-field and far-field natures.

In Chapter 3 we have shown the problematic of DF spectroscopy, both in experiments and in numerical simulations. We analyzed the influence of the correct use of

the lamp spectrum and spatial filtering on the recorded spectra. Considering the sensitivity of LSPRs to the excitation angle and the importance of single nanostructure accurate optical characterization for applications, we have shown a novel approach for the exploration of the single NP extinction spectrum using normal incidence illumination. The extinction measurements of an array of nanoparticles can be used to predict and describe the LSPR of a single nanoparticle in the visible-IR range. The comparison between the optical characterization of a single nanostructure and an ensemble of them showed similar results providing that well chosen grating spacing allow to reduce the grating impact. This analogy proposes a simpler, easier and faster characterization using ensemble measurements. We thus demonstrate the advantages of extinction spectroscopy over the DF spectroscopy for single nano-object optical characterization.

In Chapter 4, we showed that the standard use of dark-field spectroscopy on single metallic nanocylinders is mostly suitable to record the prominent (horizontal) dipolar plasmonic resonance. We used an angle resolved extinction spectroscopy and numerical simulations to investigate the different plasmonic modes of a single GNC of 170 nm-diameter. The calculations of the far-field maps show that hidden modes radiates mostly in directions, which are out of the collection geometry of the objective. We propose a new method to reveal the hidden modes with a standard dark-field microscope by changing easily its collection geometry. Moreover, we showed how to reveal plasmonic modes of gold nanocylinder using simple numerical simulations and how they differ from the simulations for the angle illumination.

Then, we found that the quadrupolar mode is spectrally close to the horizontal dipolar mode. The spectral position of the quadrupolar mode depends on many parameters, while the vertical dipolar mode is strongly correlated with the height of the GNC. The height and diameter control of the GNC can lead to a plasmonic system possessing two easily controllable resonances. These two tunable LSPRs can be used in surface enhanced spectroscopies and bio-sensing. As both modes have different spatial distribution of their electric field, they can also be used in sensing applications based on the sensitivity of the plasmonic resonances to the local refractive index.

In Chapter 5 we thoroughly studied the effect of the intrinsic plasmonic modes hybridization induced by the changing of the system symmetry for nanoparticles of different shapes. The hybridized modes have different properties and behaviors which can be explained with a help of the hybridization model.

We showed first experimental demonstration of the hybridized quadrupolar mode of a single nanocylinder. We proposed an explanation why the hybridized quadrupolar mode is not sensitive to the refractive index changes. Indeed, the hybridized quadrupolar mode presents the difference of the quadrupolar and the dipolar modes. The higher

refractive index change creates almost coherent red-shift of these two modes, therefore the difference stays unchanged.

We demonstrated experimentally and numerically the effect of the touching area between nanospheres and the substrate. The dipolar mode of perfect gold nanosphere shows same spectral position when it is placed in air and on the substrate. We showed that directional spectroscopy, like reflection scattering, can scope plasmonic modes, which are not seen with the extinction spectroscopy. Moreover, the simulations showed that scattering spectra differ for different collection geometries due to the unequal contribution of hybridized plasmonic modes for each collection geometry.

Besides the symmetry breaking by a substrate, it is possible to obtain hybridized multipolar modes by breaking the symmetry of the nanostructure itself. We showed an example of the hybridization of a quadrupolar mode of the gold pyramid.

In the last chapter we proposed an application using the multi-resonant characteristics of nanocylinder, what was revealed in the Chapter 4. We obtained simultaneous excitation and emission enhancements in two photon (up-conversion) photoluminescence of quantum dots (QDs).

The studies of experimental set-up influence on the recorded spectra show that we need be very cautious of the choosing the parts (lenses, fibers and etc.) of experimental set-up for further studies. Every detail of the experimental set-up may change the recorded signal. It should be considered for the future.

Two developed methods of experimental characterization of single nanopartiles, such as angle resolved extinction and dark-field translation scattering techniques, can be effectively used in studies of complex systems for revealing the hidden modes.

We have strong interest to verify experimentally the vertical dipolar mode for GNCs of different heights and diameters, which we studied already via numerical simulations. The tunability of both modes can be used in multiple applications.

Indeed, the silicon-based solar panels do not absorb the infrared part of solar radiation. The up-conversion of IR light to the visible using a fluorophore doubly resonantly coupled with plasmonic nanoparticle can be highly convenient to enhance the absorption of IR. Coupled with a fluorophore the doubly resonant systems with a dipolar mode in infrared and quadupolar/vertical mode in the visible can significantly increase the efficiency of nowadays solar panels.

In the last years there has been a strong interest in double resonant systems for obtaining the enhanced second harmonic generation of metallic nanostructures. The main challenge is to engineer a plasmonic system that exhibits two resonances at ω (frequency) and 2ω due to big spectral difference. Usually, the higher order modes like quadrupolar or octopular are not spectrally far enough that would allow to have resonances at demanded frequencies. Moreover, it is very hard to control the spectral

positions of multipolar modes separately from the dipolar one. We think that the easy control of the vertical and the horizontal dipolar modes allow to engineer a plasmonic system which can exhibit two resonances at ω and 2ω. Moreover, it is motivating to further study the hybridized modes, which also can be one of the ways to obtain a well separated and controlled resonances. Indeed, we already have shown for deformed spheres that the wavelength of one of the hybridized mode can be controlled (shifted) spectrally, while the position of another hybridized mode is not changed significantly.

7 French summary

Introduction

A l'ère numérique, un transport rapide et une grande capacité de stockage de l'information demandent une miniaturisation élevée et une intégration à grande échelle des dispositifs fonctionnels. De nos jours, les dispositifs électroniques ont atteint la dimension critique de 10 nm (bientôt chez Intel Corporation) provenant du fait qu'ils approchent de leur vitesse fondamentale et de la limite de leur bande passante [1, 2]. A la place des électrons, une solution prometteuse est l'usage de la lumière en tant que porteur de l'information, car les composants photoniques peuvent être plus rapides que leurs homologues électroniques [3]. Néanmoins, il existe des difficultés à réduire la technologie en raison de la limite de diffraction (limite de Abbe) à la moitié de la longueur d'onde effective [4–6]. La figure 7.1 montre un graphique liant la vitesse des dispositifs à leurs dimensions critiques, pour différentes technologies. Ici, un compromis entre une haute vitesse de transfert par des composants photoniques et la taille des dispositifs électroniques peut être trouvé dans ce qu'on appelle la plasmonique. La plasmonique est le domaine à l'intersection de la science et de la technologie dans lequel l'interaction de la lumière avec la matière est traduite par une excitation électromagnétique des électrons de conduction du métal qui entrent en résonance à l'interface métal-diélectrique [8, 9]. Derrière l'usage prometteur de la plasmonique pour la technologie de l'information, ce domaine peut également être utilisé avec succès dans

d'autres applications telles que les énergies renouvelables, la détection, etc. [10–16].

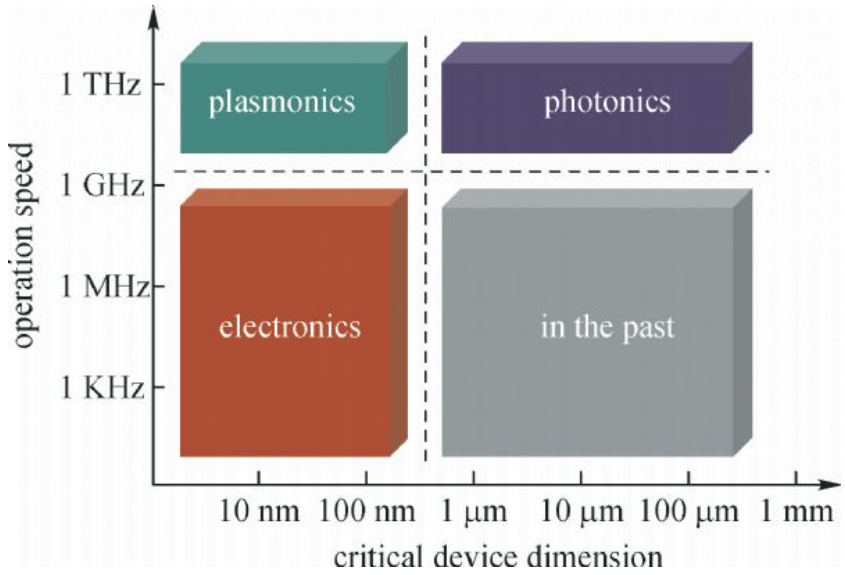

FIGURE 7.1: Vitesse d'opération typique et dimension critique de dispositifs technologiques [7]

Les structures plasmoniques sont le point clef de beaucoup d'applications basées sur leurs propriétés optiques. De nombreuses techniques de caractérisations optiques ont été développées dans le but de déterminer les résonances plasmoniques. De plus, obtenir les mêmes résultats avec les mêmes caractérisations optiques faites par d'autres chercheurs représente un challenge. Par exemple, la figure 7.2 montre la comparaison de la position des résonances de nanocylindres d'or identiques publiées par différents groupes (les valeurs pour une hauteur de 20 nm se trouvent dans le Tableau 1). La question essentielle est « pourquoi il existe un déplacement de la position du pic de résonance »?

TABLE 7.1: Positions des pics de LSPR dans différents articles

Diamètre (nm)	38.5	51	77	140	193	Article
Positions des pics (nm)	546	576	620	760	885	[17]
	578	585	633	735	811	[18]

L'idée principale de ce travail de thèse est de passer en revue les propriétés optiques fondamentales des nano-objets plasmoniques et d'expliquer les différences possibles des résonances plasmoniques provenant de différents facteurs et de répondre à la question précédente. Le manuscrit est séparé en deux parties principales : (i) l'étude des modifications des résonances plasmoniques causées par l'instrumentation (comme le montage expérimental et ses composants) ; (ii) les variations des propriétés optiques

des résonances plasmoniques basées sur les changements du système plasmonique lui-même. Les données expérimentales sont accompagnées par des simulations et par leur analyse complète.

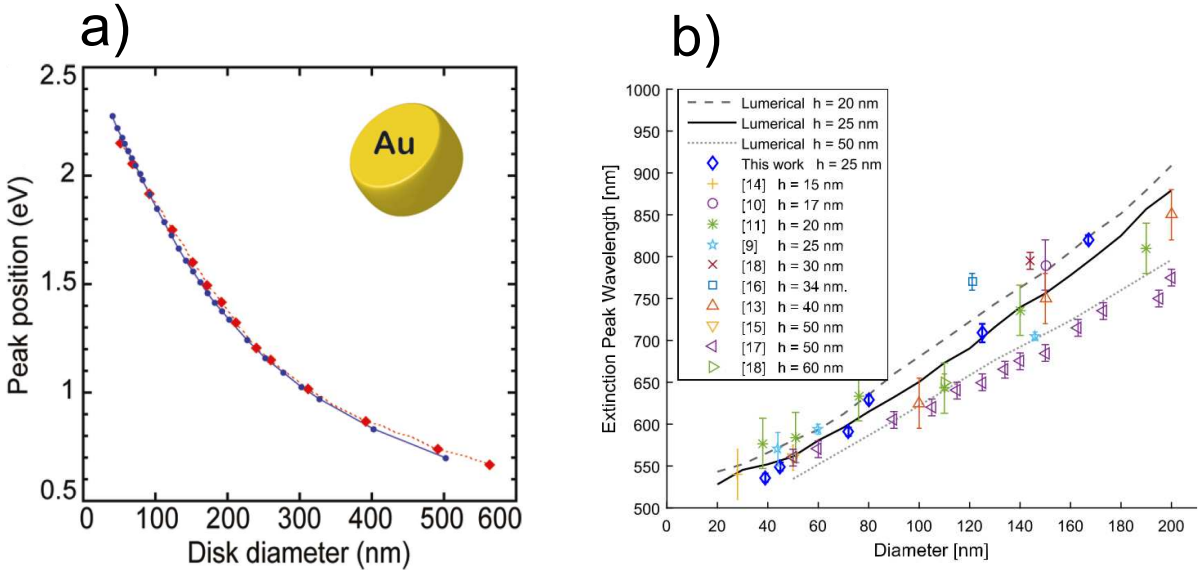

FIGURE 7.2: (a) Positions des pics des spectres d'extinction de nanocylindres d'or en fonction du diamètre. La hauteur des nanocylindres d'or est de 20 nm et le substrat est du verre [17].(b) Positions des pics des spectres d'extinction de nanocylindres d'or déposés sur du verre en fonction du diamètre pour différentes hauteurs [18]. Les lignes montrent les données simulées. h est la hauteur.

Chapitre 1 :Introduction aux plasmons

Les propriétés optiques des métaux dépendent fortement de la fréquence de l'onde électromagnétique. Les métaux sont hautement réfléchissants pour des fréquences jusqu'au visible et l'onde électromagnétique ne peut se propager à travers. A hautes fréquences, la majorité des métaux présentent un caractère diélectrique. Cela dépend de leur structure de bande électronique. Par exemple, les métaux alcalins (Li, Na, K, Rb, Cs, Fr) sont transparents aux UVs alors que les métaux nobles (Au, Ag, Cu) possèdent une forte absorption dans l'UV causée par les transitions interbandes. L'interaction entre une onde électromagnétique externe et la bande de conductions des électrons à l'interface métallique peut mener à des plasmons de surface (SP) [8, 19, 20]. Ils sont usuellement définis comme un quantum d'oscillations du plasma [21], dont la théorie a été proposée par Pines et Bohm [22]. Les plasmons font souvent références aux plasmons polaritons représentant l'état couplé entre un plasmon et un photon.

Les plasmons de surface localisés sont un cas particulier des plasmons polaritons de surface, lorsque le nano-objet métallique est plus petit que le longueur de propagation

du plasmon de surface. La résonance des plasmons de surface localisés (“LSPR” pour “Localized Surface Plasmon Resonance » en anglais) correspond à l’interaction entre la lumière et les nanoparticules conductrices (NPs) ; ces dernières étant plus petites que la longueur d’onde incidente. La principale différence entre les plasmons de surface et les plasmons de surface localisés est le fait que les LSPR se produisent à des fréquences fixées. Ces résonances sont sensibles à plusieurs facteurs comme la taille, la forme, la morphologie, le milieu environnant ou encore le matériel choisi. Par exemple, la Figure 7.3 montre les spectres d’extinction et de diffusion de nanoparticules de formes et de tailles différentes.

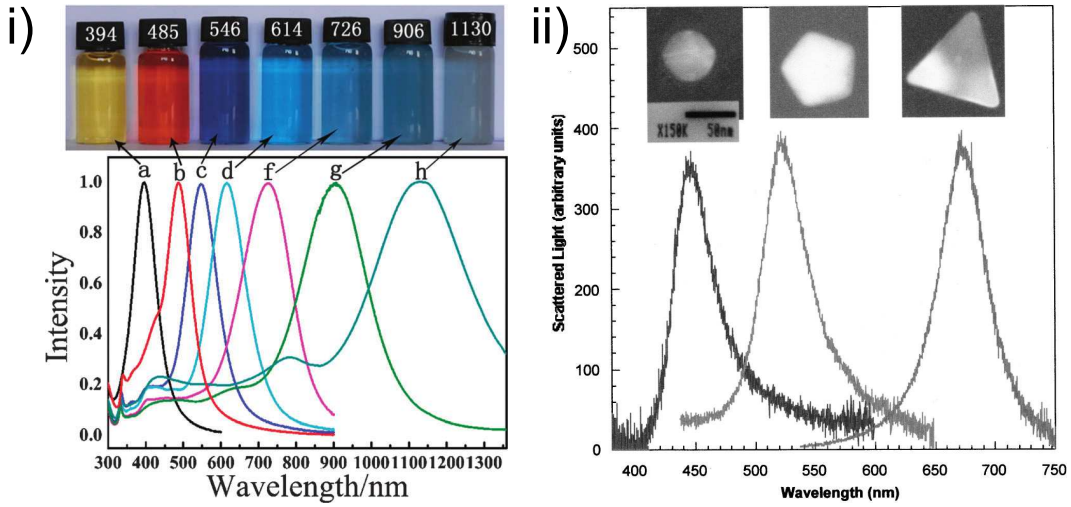

FIGURE 7.3: (i) Images de nanoparticules d’argent (a) et de nanoplaques d’argent (b–h) colloïdales avec différentes couleurs correspondant aux spectres d’extinction de l’UV au proche infrarouge. Les nombres sur les bouchons représentent les longueurs d’ondes des positions des pics de la LSPR [35]. (ii) Spectres de diffusion pour des nanoparticules d’argent uniques [36].

Les propriétés optiques des métaux présentent un grand potentiel pour différentes applications. Ces dernières, basées sur les propriétés plasmoniques, ont un champ d’application très vaste : les spectroscopies exaltées, la détection biologique et chimique, le photovoltaïque, la génération de couleurs ou encore l’imagerie optique subatomique.

Les propriétés plasmoniques des nanoparticules métalliques sont utilisées depuis longtemps pour la création de couleurs à l’échelle mésoscopique. L’exemple le plus Populaire est la coupe Lycurgus produite par l’empire Romain (4ème siècle). Le verre de cette coupe contient de la poudre d’or et d’argent. Quand la coupe est illuminée de l’extérieure (Figure 7.4a), elle apparaît verte à cause de la diffusion de la LSPR dans la gamme du vert. Quand la coupe est illuminée de l’intérieur (Figure 7.4b), elle apparaît rouge à cause de l’absorption dans la gamme du vert causée par la LSPR. Un autre exemple de la génération de couleurs par les propriétés optiques des nanoparticules métalliques est représenté sur la figure 7.4c [38]. Un autre axe du développement et

de l'utilisation des matériaux plasmoniques est l'amélioration de la diffusion Raman et de l'intensité de fluorescence.

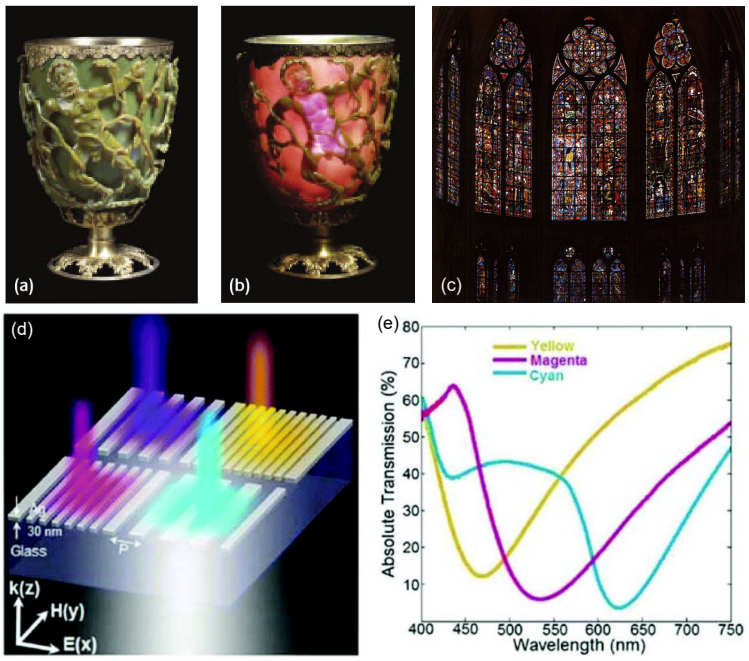

FIGURE 7.4: Coupe romaine Lycurgus (a) en réflexion (b) et en transmission [37]]. (c) Vitraux de la Cathédrale de Troyes. (d) Schéma d'un filtre de couleur d'un reseau d'argent d'épaisseur 30 nm avec différentes périodes. (e) Spectres de transmission mesurés correspondant aux couleurs jaune, magenta et cyan des structures en (d) [38].

Horrer et al. ont montré expérimentalement et numériquement un bel exemple d'un détecteur basé sur les LSPR [40]. Ils ont utilisé un réseau de structures de type MIM (métal-isolant-métal) pour la détection. La figure 7.5a présente le schéma d'un élément unique du réseau. Ils ont démontré que le détecteur est sensible à des modifications de l'indice de réfraction d'un pas de 0,01. La plus haute sensibilité reportée est de 0,003 [41].

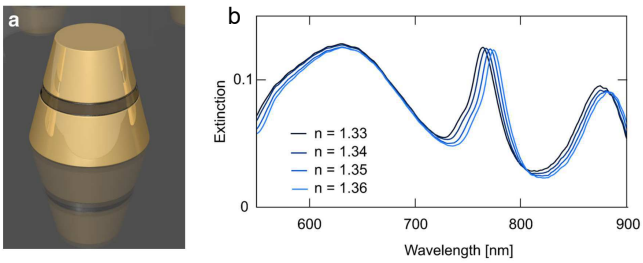

FIGURE 7.5: (a) Schéma d'un dimère vertical or-SiO_2-or. (b) Mesures de la sensibilité dans une solution eau-glycérine à différents ratio pour faire varier l'indice de réfraction [40].

Chapitre 2 :Les modes plasmoniques

Les nanoparticules plasmoniques, outre leur mode dipolaire, peuvent supporter des modes d'ordre supérieur connus comme quadripolaire, hexapolaire, octopolaire, etc. [55–57]. La figure 7.6a montre les spectres d'extinction calculés de nanosphères d'argent dans l'air. Un mode unique est observé pour les nanosphères de diamètre 40 et 60 nm, car la longueur d'onde de l'illumination est relativement grande comparée aux tailles des nanosphères. Les plus grosses nanosphères montrent un second mode plasmonique autour de 355 nm sous la forme d'un épaulement (pour le diamètre 80 nm) ou d'un pic (pour le diamètre 120 nm) sur les spectres d'extinction. En effet, avec l'augmentation de la taille des nanosphères, la réponse du nuage électronique au champ électrique incident est décalée dû à l'effet de retard [58–60]. Il est ainsi possible d'exciter le mode quadripolaire de la sphère, comme montré par la figure 7.6e représentant la distribution de charges surfaciques dans le plan de coupe xz de la sphère.

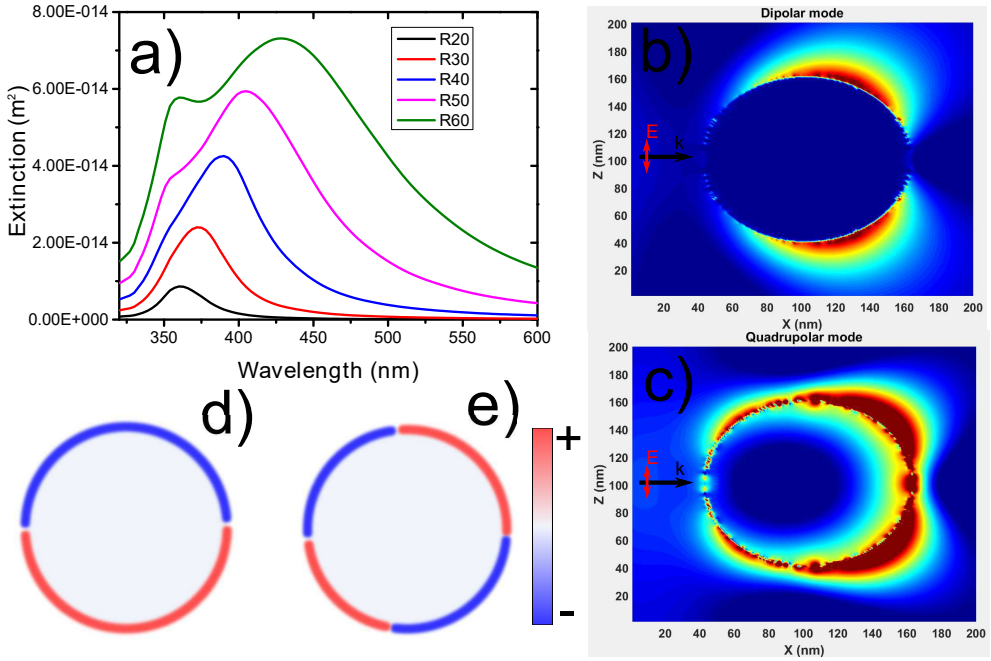

FIGURE 7.6: (a) Spectres d'extinction de nanosphères d'argent calculés grâce à la théorie de Mie dans le vide. Le rayon varie de 20nm à 60 nm. (b) et (c) Cartes de champ électrique pour une excitation à (b) 428 nm et (c) 358 nm. (d) et (e) sont respectivement les distributions de charges calculées.

En raison de la brisure de symétrie due à leur géométrie particulière, les nanocylindres peuvent supporter deux modes dipolaires différents en fonction de leur orientation. L'un est appelé mode dipolaire horizontal (lorsque l'oscillation des charges se fait dans le plan de coupe du cylindre correspondant à un disque) et l'autre est appelé

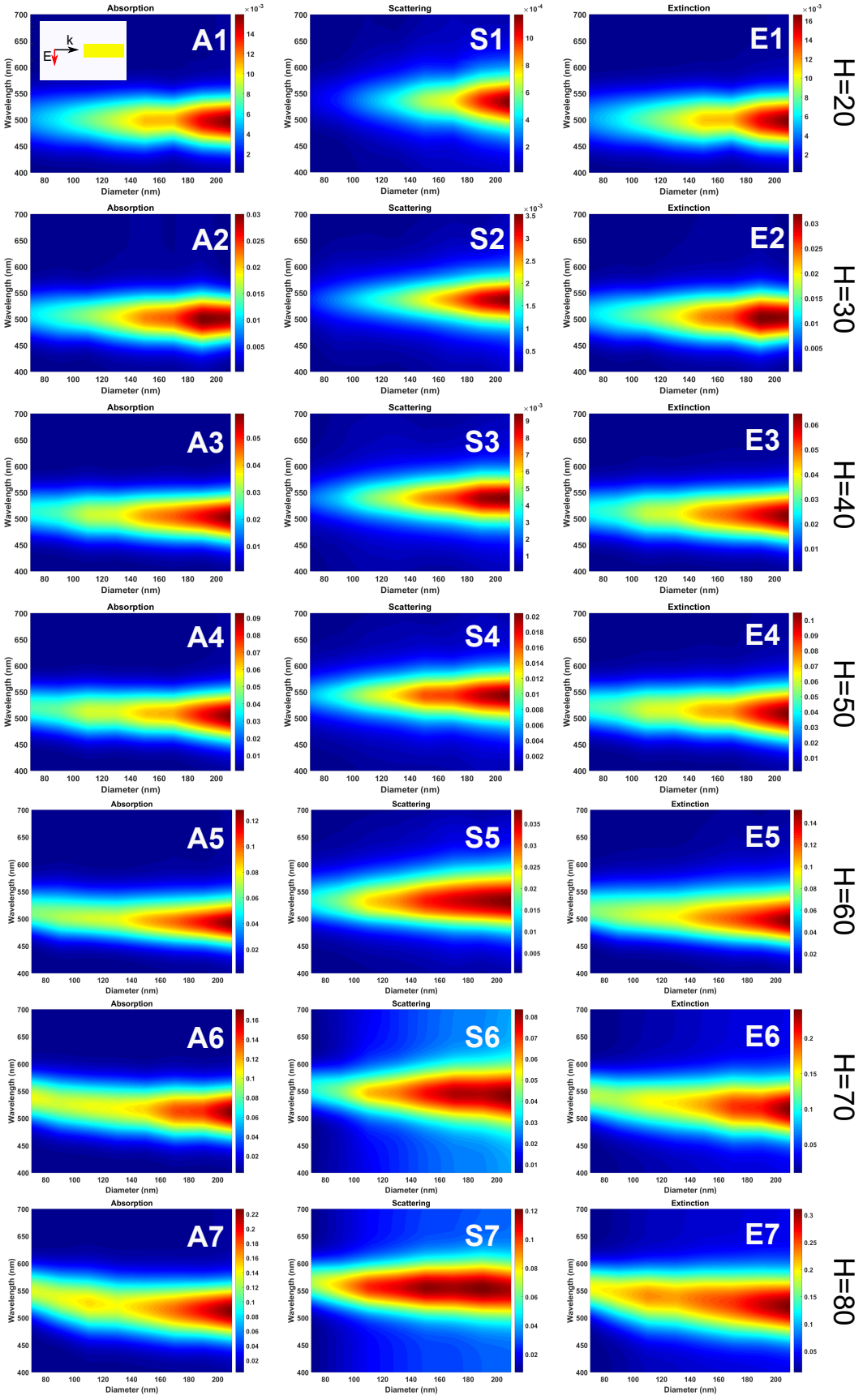

FIGURE 7.7: Cartes de spectres calculés d'extinction, de diffusion et d'absorption pour des GNC de différentes hauteurs dépendant du diamètre. H est la hauteur en nm. L'encart montre le schema d'illumination. Le milieu environnant est l'air.

mode dipolaire vertical (lorsque l'oscillation des charges se fait dans le plan de coupe rectangulaire perpendiculaire au disque). Nous allons étudier séparément l'impact du diamètre des nanocylindres sur la position du pic du mode dipolaire vertical et l'effet de la modification de la hauteur des nanocylindres sur la position du pic du mode dipolaire horizontal. De façon contrintuitive, le mode dipolaire horizontal dépend fortement de la hauteur pour beaucoup de diamètres. La position du pic dépend du ratio entre le diamètre et la hauteur. Quand le ratio augmente, le mode dipolaire horizontal est déplacé [17].

Il existe très peu d'études sur le mode dipolaire vertical. Un des papiers pionniers mentionnant le mode vertical a été publié par Jin et al. en 2001 [64]. Ils ont démontré que le mode dipolaire vertical est faible et étroit, et est à peine discernable. La figure 7.7 montre les cartes de spectres d'absorption, de diffusion et d'extinction de nanocylindres d'or (GNCs) en fonction de leur diamètre et ce, pour différentes hauteurs. L'excitation du nanocylindre est réalisé par une onde plane polarisée verticalement de telle sorte que ces cartes montrent le mode dipolaire vertical. Nous pouvons remarquer que la position du pic du mode dipolaire vertical de GNC fins est relativement stable avec la variation du diamètre. La différence de la position des pics des diamètres 70 nm et 210 nm est de 5 nm (figure 7.7 carte S1). Nous admettons que le principal facteur influençant le mode dipolaire vertical est la hauteur. De plus, avec l'augmentation de la hauteur des GNC, la position des pics du mode vertical commence à dépendre du diamètre. Nous pouvons voir que lorsque le ratio entre le diamètre et la hauteur est plus petit que 1,5, la position du pic subit clairement des changements. Ce fait est important pour comprendre qu'il est possible de contrôler séparément les deux modes dipolaires (horizontal et vertical) en faisant varier la hauteur et le diamètre.

Chapitre 3 : Méthodes et influence du montage expérimental

La nanospectroscopie fait simplement référence à la spectroscopie de structures à l'échelle nanométrique. Suite à l'intérêt grandissant pour les propriétés optiques des nano-objets, plusieurs techniques optiques ont été développées pour la caractérisation de nano-objet unique [73–77]. Zsigmondy et al. ont développé un microscope à immersion en champ sombre pour observer des nano-objets uniques dans un liquide. Dans cette section, nous analysons des facteurs expérimentaux qui peuvent causer une modification de la réponse optique dans la diffusion en champ sombre d'un nanocylindre d'or unique.

Normalisation par le spectre de la lampe

Nous avons besoin de normaliser le spectre enregistré initialement avec le spectre de la lampe dans le but d'obtenir un spectre champ sombre. Nous utilisons un miroir pour enregistrer le spectre de la lampe. Sur la figure 7.8a nous montrons un spectre en champ sombre d'un nanocylindre d'or unique normalisé par le spectre de la lampe pris grâce au miroir. La simulation correspondante est illustrée sur la figure 7.8d, et nous pouvons confirmer une discordance significative entre le spectre expérimental et le spectre calculé. Une autre solution pour enregistrer le spectre de la lampe consiste à utiliser un substrat rugueux de PTFE (polytetrafluoroethylene). En effet, le PTFE possède une réflectance diffuse uniforme dans la gamme visible – proche infrarouge. Ainsi, de cette manière, nous retrouvons le spectre normalisé de la figure 7.8b. Nous pouvons alors voir une bonne concordance entre les spectres expérimental et calculé.

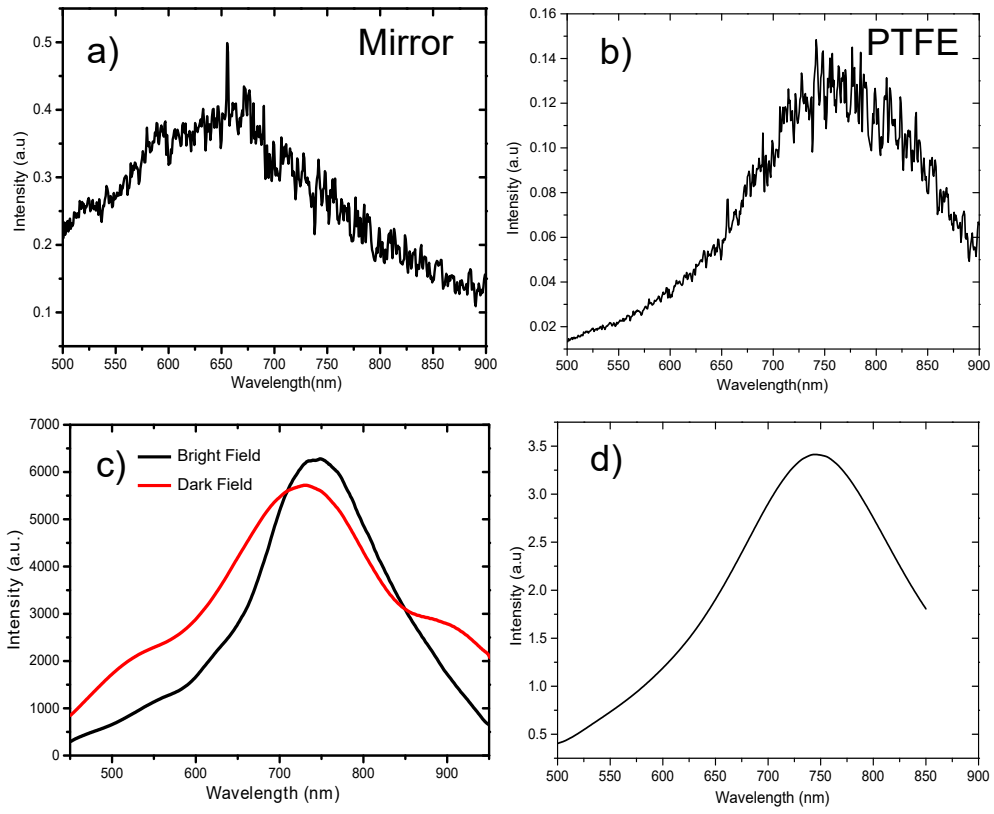

FIGURE 7.8: (a) Spectres de diffusion en réflexion en champ somnre d'un nanocylindre de 170 nm de diamètre. Le spectre en champ sombre est normalisé par le spectre de la lampe enregistré grâce à un miroir. (b) Le spectre en champ sombre est normalise par le spectre de la lampe enregistré grâce à un substrat de PTFE. (c) Le spectre de la lampe est enregistré grâce à un miroir (courbe noire) et grâce à un substrat de PTFE (courbe rouge). (d) Spectre de diffusion simulé numériquement d'un GNC de diamètre 170 nm.

Mesures d'ensemble comme une alternative à la spectroscopie en champ sombre

Les figures 7.9a, 7.9c, 7.9e montrent les spectres d'extinction expérimentaux de réseaux (pas 1 μm) de diamètres 135 nm, 170 nm et 200 nm, respectivement. Les simulations correspondantes sont montrées sur les figures 7.9b, 7.9d et 7.9f.

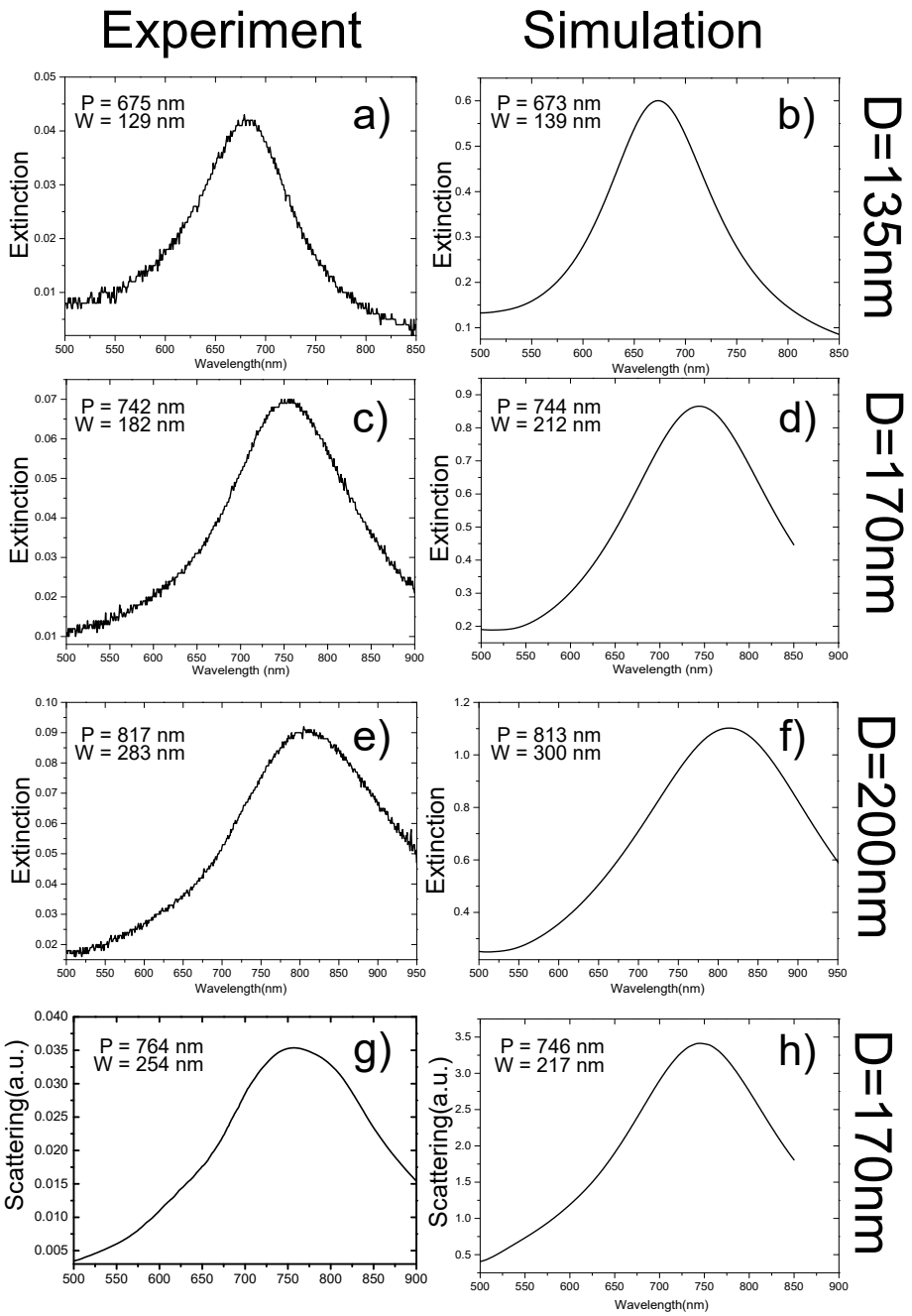

FIGURE 7.9: (a-f)Spectres d'extinction d'un réseau de GNC avec une période de 1 1μm. D est le diamètre des GNC. P est la position du pic du spectre et W est la largeur du spectre. (g,h) Spectres de diffusion en réflexion en champ sombre d'un nanocylindre de 170 nm de diamètre

Dans ce cas, le spectre d'extinction d'un GNC unique sur un substrat de verre a été simulé. Il y a un bon accord entre les résultats expérimentaux et numériques. Un réseau périodique de nanoparticules avec un pas constant de 1 μm supporte plusieurs ordres de diffractions dans le visible et le proche infrarouge. Sur la figure 7.10a, nous montrons un nombre calculé des ordres de réseau de propagation supportés pour une incidence normale et pour des longueurs d'onde comprises entre 500 nm et 850 nm sur du verre, en utilisant la théorie de la diffraction. Nous présentons une carte du champ lointain des ordres diffractés en dehors du plan dans le verre à une longueur d'onde de 502 nm et 850 nm sur les figures 3.137.10 et 3.137.10, respectivement. Considérant la loi de Snell, plusieurs ordres vont être bloqués dans le verre et donc ne seront pas transmis. L'ouverture numérique de 0,42 dans l'air correspond à un angle de 16° dans le verre. Nous pouvons noter en regardant les figures 7.10b et 7.10c que nous collectons seulement l'ordre 0. Nous n'observons pas d'autres ordres en dehors du plan sur les spectres d'extinction expérimentaux.

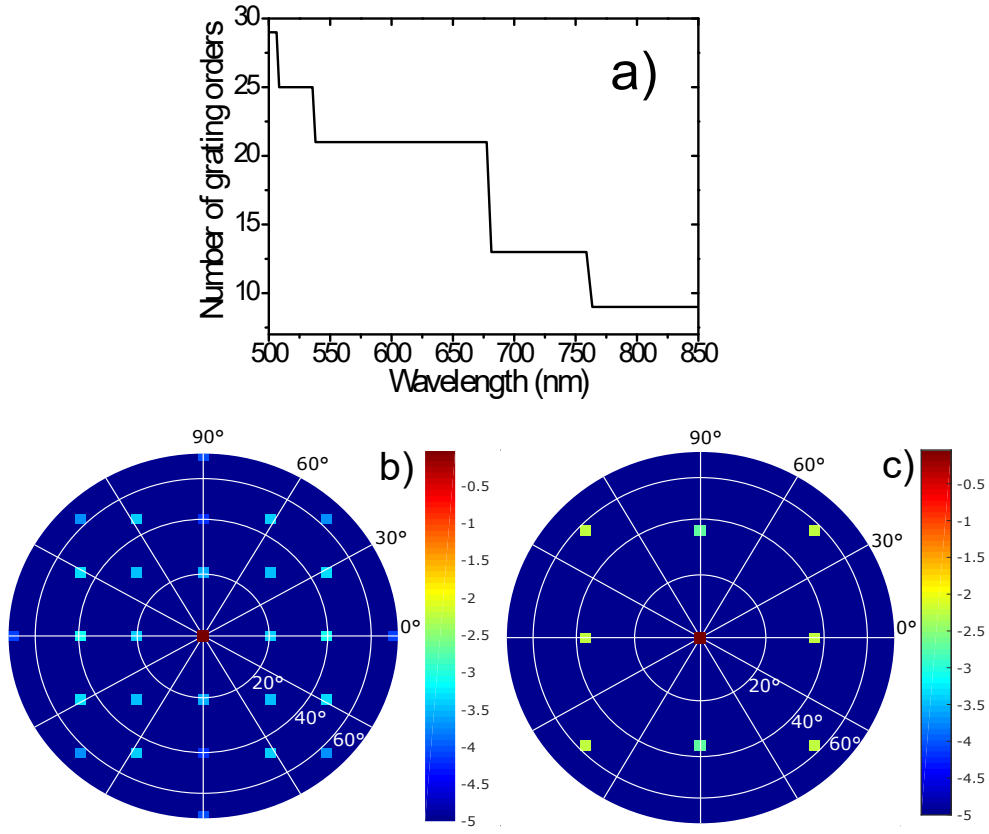

FIGURE 7.10: (a) Ordres de diffractés dans le verre pour un réseau de GNC présentant une période infinie et un pas de 1 μm. (b) Distribution en champ lointain des ordres diffractés dans le verre à une longueur d'onde de 502 nm et (c) 850 nm. L'échelle est logarithmique.

Le couplage le plus fort entre des ordres diffractés et la LSPR a lieu pour les ordres de diffraction (0, ±1) et (±1, ±1) dans le plan [83]. Nous avons calculé que les

longueurs d'onde de ces ordres sont en dehors de la zone de collection. En effet, respectivement, les ordres correspondent à des longueurs d'onde de 1,52 μm et 1,075 μm. Donc nous avons montré qu'enregistrer un spectre d'extinction sur un réseau de GNC présentant un pas de 1 μm revient à étudier le spectre de diffusion d'un GNC unique (Figure 7.9g,7.9h).

Chapitre 4 : Les modes cachés

Il a été montré qu'en utilisant une spectroscopie d'extinction résolue en angle, il est possible d'exciter et d'enregistrer des modes d'ordre supérieurs comme les modes quadripolaire ou octopolaire [57, 82, 84]. Il a également été prouvé que le mode vertical pouvait être excité dans un réseau en utilisant une illumination en angle [84]. De plus, les spectres de réflexion et de transmission en champ sombre ne montrent pas ces modes. Dans la suite, nous allons essayer de comprendre pourquoi les modes d'ordre supérieur et le mode vertical ne sont pas visibles sur les spectres en champ sombre et allons proposer une méthode pour les révéler. Nous avons prouvé dans la section précédente que sous certaines conditions l'influence du réseau sur la LSPR peut être négligeable. Pour les expérimentations, nous utilisons un réseau de GNCs de diamètre 170 nm et de hauteur 50 nm, avec un pas de $1\mu m$. Ces paramètres permettent de mesurer un spectre d'extinction du réseau qui correspond au spectre d'un GNC unique. Nous réalisons les mesures pour des illuminations polarisées P et S quand l'échantillon est incliné de 50° relativement à l'axe optique de l'objectif. Sur la figure 7.11a est illustré le spectre d'extinction d'un réseau de GNC (polarisation P). Le pic (i) à 761 nm est bien prononcé, et nous pouvons également voir l'apparition de deux nouveaux pics, autour de 600 nm (ii) et autour de 525 nm (iii).

Sur la figure 7.11c, nous montrons les spectres d'extinction expérimentaux pour une illumination polarisée S. Il apparaît deux modes plasmoniques à 738 nm (mode 1) et à 600 nm (mode 2). Nous attribuons le pic proéminent pour les deux spectres (Figure 7.11a et 7.11c) à l'excitation du mode dipolaire.

Pour identifier les modes plasmoniques excités, nous faisons des calculs de distributions de charges surfaciques (SChD). Le mode (i) montre une excitation du mode dipolaire défini, où les charges négatives et positives sont placées sur les côtés et créer un moment dipolaire effectif. Le mode (ii) se révèle être un mode diagonal quadripolaire. Le mode (iii) est associé au mode dipolaire vertical. Ce mode est seulement visible pour une illumination polarisée P car il requiert que la composante du champ électrique en dehors du plan (E_z) soit non nulle. Pour comprendre pourquoi nous n'observons pas expérimentalement des modes d'ordre supérieur sur les spectres en

champ sombre, nous faisons des calculs de diffusion pour deux géométries de collection (réflexion et transmission) et pour deux polarisations dans l'air (Figure 4.3).

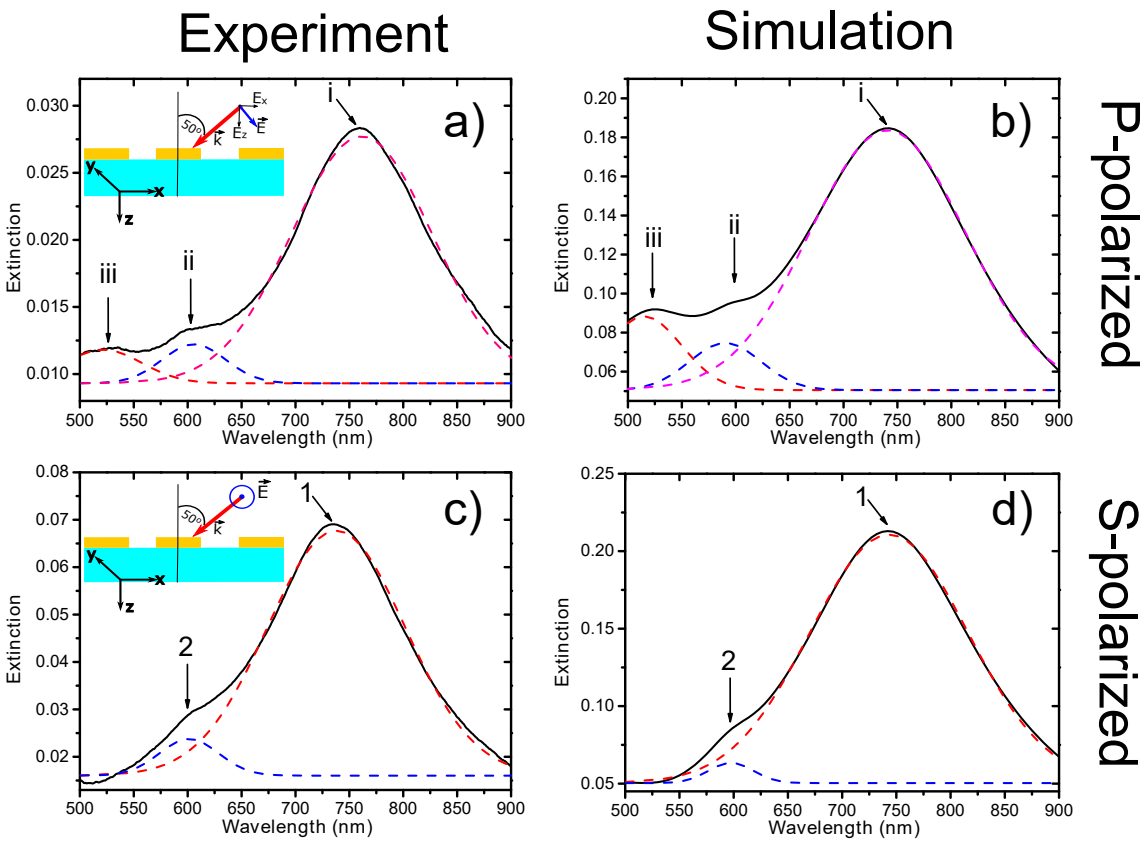

FIGURE 7.11: (a) Spectre d'extinction résolu en angle polarisé P d'un GNC de diamètre 170 nm (b) Simulations numériques correspondantes. (c) Spectre d'extinction résolu en angle polarisé S, (d) Simulations numériques correspondantes.

Outres le mode dipolaire principal, il apparaît plusieurs modes sous la forme de deux lobes dans différentes directions (indiquées par les flèches blanches sur les figures). Bien que ces lobes pour les deux géométries de collections montrent une nature radiative, nous ne voyons pas clairement ces modes sur les spectres de diffusion (Figure 7.9g). Le spectre de diffusion expérimental est collecté par un objectif d'ouverture numérique de 0,8 représenté par les lignes pointillées horizontales sur les figures 7.12c et 7.12e. Ainsi, la puissance radiative des lobes n'est pas totalement collectée comme leur radiation est en dehors de la zone de collection. C'est pourquoi nous n'observons pas clairement expérimentalement ces nouveaux modes sur les spectres de diffusion en champ sombre.

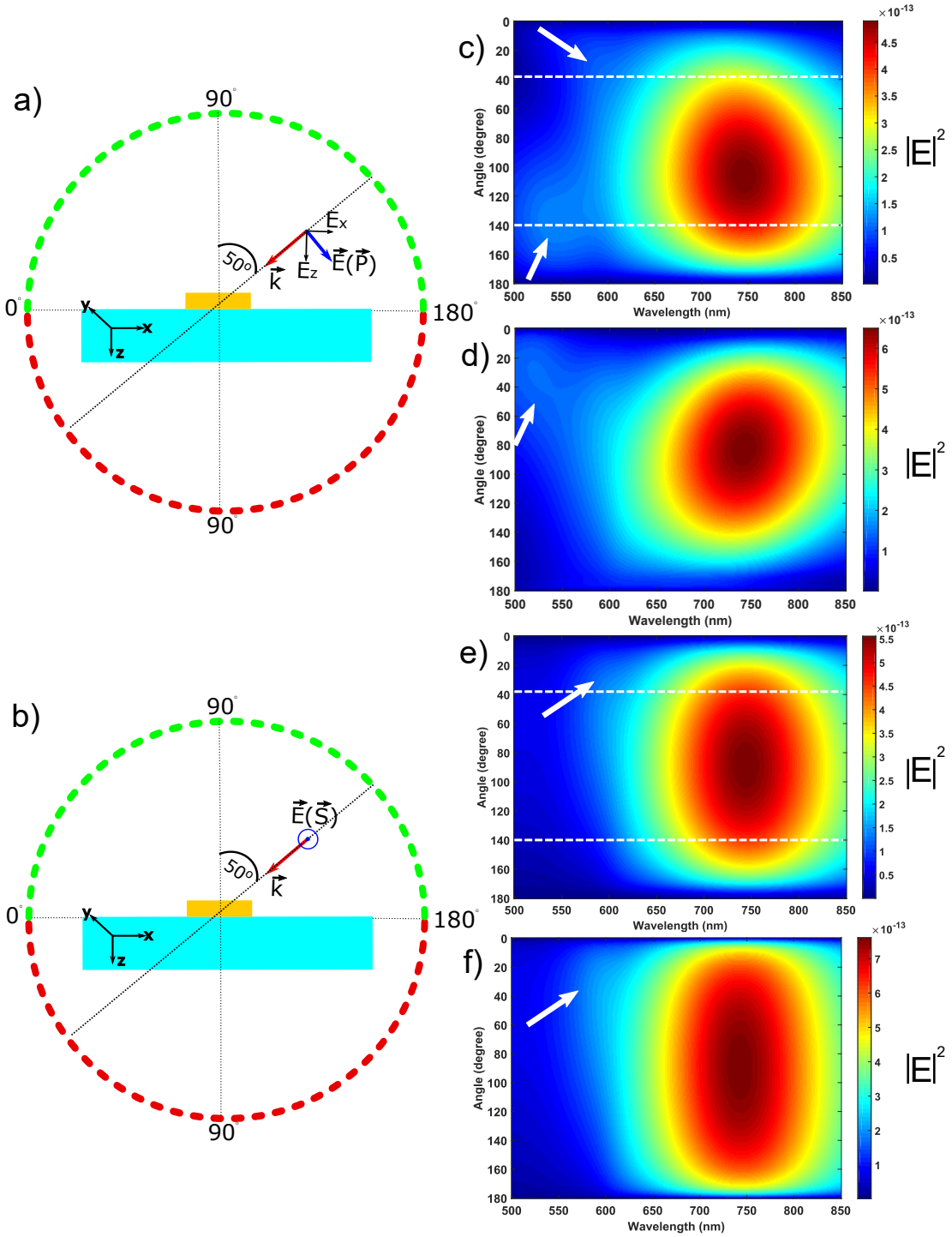

FIGURE 7.12: (a) et (b), Schémas des excitations polarisée P et S avec un angle de 50°. Les géométries de collection en réflexion et en transmission sont données par les demi-cercles verts et rouges, respectivement. Le vecteur d'onde représente k, E le champ électrique, S et P les polarisations, E_x et E_z les composantes du champ électrique. (c) et (d), Carte de la collection en champ lointain dépendant de l'angle pour les géométries en réflexion et en transmission pour la polarisation P. (e) et (f), Carte de la collection en champ lointain dépendant de l'angle pour les géométries en réflexion et en transmission pour la polarisation P. Les lignes pointillées blanches montrent les limites de collection pour une ouverture numérique de 0,8, quand la collection est centrée à 90°.

Révéler les modes cachés en utilisant la microscopie en champ sombre

Nous avons vu les propriétés radiatives des différents modes et compris pourquoi la technique de diffusion en champ sombre ne permet d'enregistrer que le mode dipolaire horizontal. Considérant les spécifications des différents modes radiés, nous proposons une méthode qui permet de révéler ces modes cachés avec la technique en champ sombre. La figure 7.13a montre un spectre de diffusion en champ sombre pour un GNC. Dans ce cas, le GNC est centré comparé à la zone de collection comme montré par la

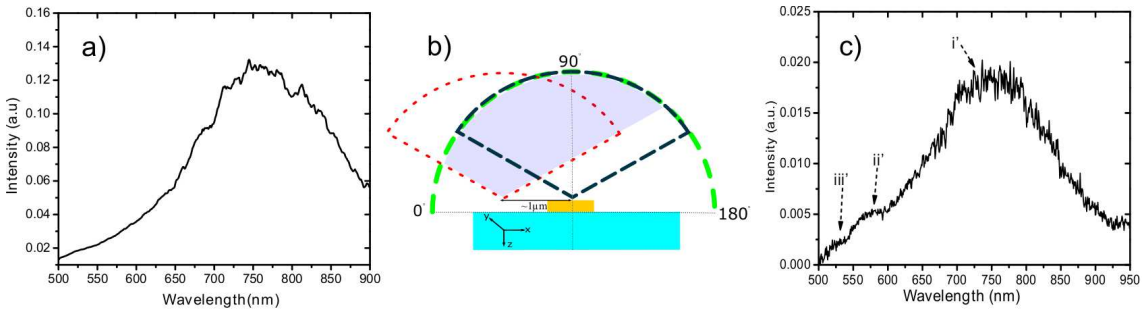

FIGURE 7.13: (a) Spectre de diffusion en champ sombre d'un GNC quand la collection est centrée sur ce dernier. (b) Illustration de la zone de collection quand la collection est centrée sir le GNC (courbe pointillée bleue) et quand la collection est déplacée (courbe pointillée rouge). (c) Spectre de diffusion en champ sombre quand la collection est déplacée du centre du GNC.

ligne pointillée bleue foncée sur la figure 7.13b. Si nous bougeons l'échantillon approximativement de 1 μm, le point de collection est déplacé de la même distance. La ligne pointillée rouge sur la figure 7.13b (zone colorée grise) correspond à la nouvelle zone de collection. De cette manière, nous changeons la géométrie de collection et filtrons certaines radiations provenant du mode dipolaire. Dans ce cas, le ratio entre les radiations collectées provenant du mode dipolaire et des autres modes est changé. En effet, le spectre expérimental de diffusion en champ sombre enregistré avec cette nouvelle géométrie de collection (figure 7.13c) confirme la détection de nouveaux pics (mode (iii') et mode (ii')). Le mode (i') est le mode dipolaire proéminent, tandis que le mode (iii') est le mode dipolaire vertical et le mode (ii') correspond spectralement avec le mode quadripolaire.

Chapitre 5 : Hybridation des modes multipolaires

Dans la section précédente, nous avons discuté le nombre de facteurs affectant la résonance plasmonique d'un nano-objet métallique unique. Un des mécanismes pour révéler les modes sombre est d'étudier leur couplage avec les modes claires. Ce couplage survient avec une brisure de la symétrie du système. Par exemple, un milieu anisotropique peut causer un couplage entre les modes sombres et claires. Pour

comprendre le comportement des modes plasmoniques dans un régime de couplage, Prodan et al. ont proposé un modèle d'hybridation [91]. Nous proposons une étude expérimentale de modes plasmoniques hybrides de réseaux désordonnés de nanocylindres d'argent sur un substrat.

Hybridation des modes de nanocylindres d'argent

Cette section est inspirée par deux papiers, où Sherry et al. [92] et Zhang et al. [90] étudient l'hybridation de deux modes plasmoniques d'une structure simple. L'effet du substrat sur les modes des cylindres a été prédit par des simulations antérieures [93]. De plus, le mécanisme n'a pas été expliqué sur la base de la théorie d'hybridation. Dans cette section, nous explorons en profondeur les changements de la réponse optique de nanocylindres d'argent en s'approchant du substrat et confirmons les résultats simulés avec des expérimentations. Sur la figure 7.14a, nous montrons le spectre calculé de la transmittance d'un nanocylindre d'argent unique (SNC for Silver Nano Cylinder) dans l'air et placé à différentes distances du substrat de verre. Les spectres de transmittance pour les SNC dans l'air montrent un unique pic noté (i) et un épaulement autour de 347 nm (iii). En s'approchant du substrat, le pic proéminent (i) se déplace vers le rouge et un nouveau pic apparaît (ii). Contrairement au mode (i) qui se déplace en s'approchant du substrat, le mode (iii) reste à la même position spectrale pour différentes distances SNC-substrat. Pour comprendre les origines du mode (iii), nous calculons la carte du champ électrique et des distributions de charges pour une excitation à 345 nm sur la figure 7.14b. Ce mode a été décrit précédemment comme une sorte de combinaison du mode dipolaire et d'un mode radial dans le plan appelé « breathing mode » [57, 94, 95]. La carte du champ électrique du mode (ii) est illustrée sur la figure 7.14c. Le principal confinement du champ électrique est remarqué sur les bords du plan supérieur du SNC. La distribution des charges surfaciques correspondante est montrée sur la figure 7.14e. Il existe une sorte de distribution du mode dipolaire avec les charges principalement localisées sur les coins du plan supérieur du SNC. Le mode (i) montre une caractéristique du mode dipolaire avec un champ fortement confiné localisé sur les bords du plan inférieur (Figure 7.14d,7.14d).

La figure 7.15a montre les spectres de transmittance obtenus expérimentalement sur des SNCs distribués aléatoirement sur un substrat de verre. Premièrement, nous identifions deux pics contrairement aux trois pics qui étaient présents dans les simulations (Figure 7.14a). De plus, nous observons clairement un pic non-symétrique localisé à 485 nm. Nous réalisons des simulations plus exactes des expérimentations en prenant en compte les particularités de nanocylindres d'argent (la forme des nanoparticules et la présence d'une couche d'adhésion) (Figure 7.15b). Nous pouvons noter

qu'un épaulement de 420 nm à 450 nm apparaît sur les spectres. En se basant sur les cartes de champ électrique (Figure 7.15e), nous admettons que c'est le mode de cavité de la couche d'oxyde de titane servant de couche d'adhésion. La modification de la forme change la position spectrale des modes. Quand nous réduisons le diamètre de la face supérieure et que nous changeons la courbure, le mode (ii) se déplace vers le bleu et chevauche spectralement le mode (iii).

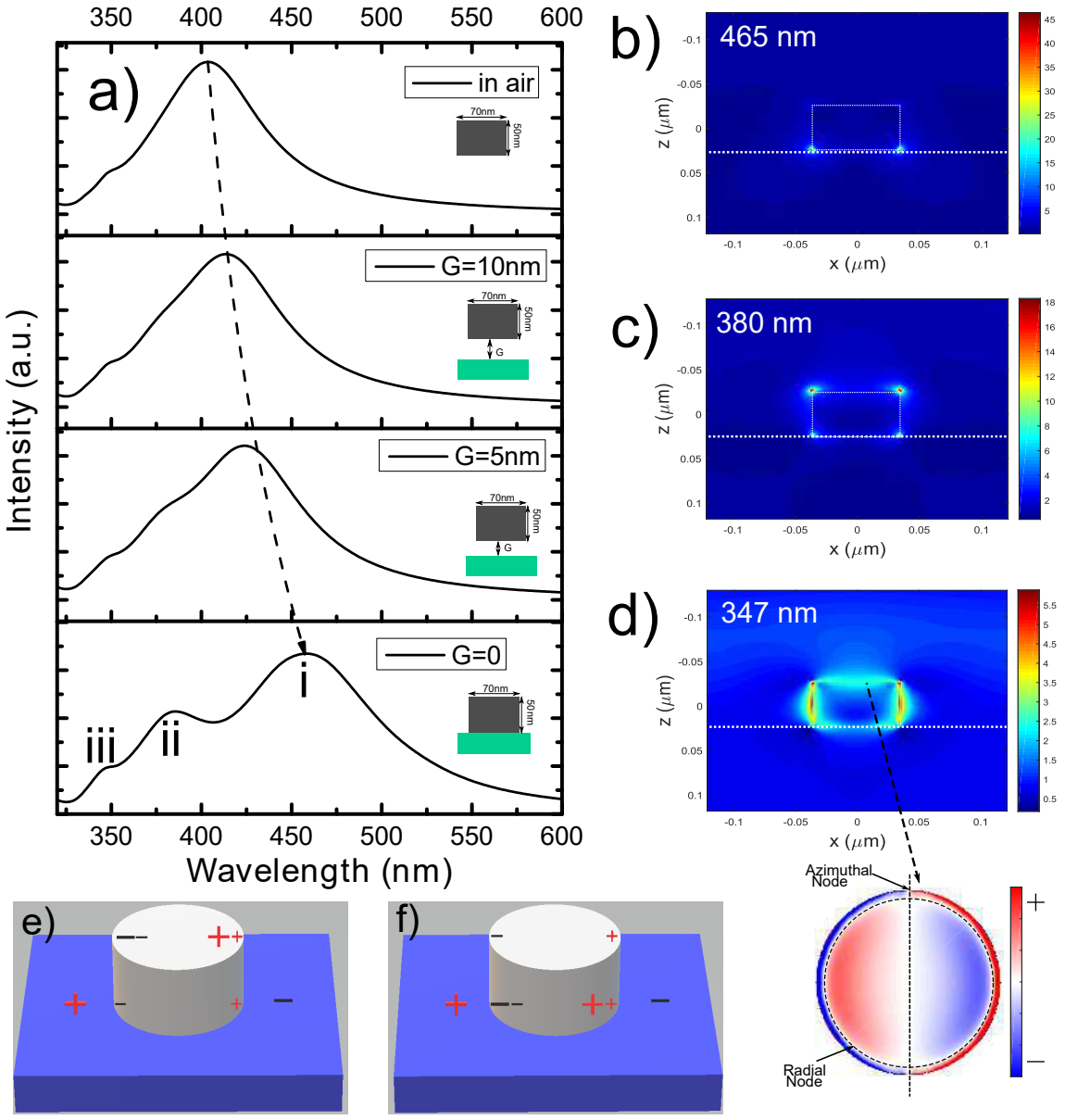

FIGURE 7.14: (a) Spectres de transmittance calculés d'un nanocylindre d'argent dans l'air et à différentes distances du substrat, le diameter est 70 nm et la hauteur 50 nm. (b) Cartes de champ électrique : profil de coupe XZ au centre du nanocylindre. La ligne pointillée blanche montre la surface du substrat pour une excitation à 465nm (Mode i) (c) 380nm (Mode ii), (d) 347nm (Mode iii). Distribution de charges pour (e) Mode ii et (f) Mode i.

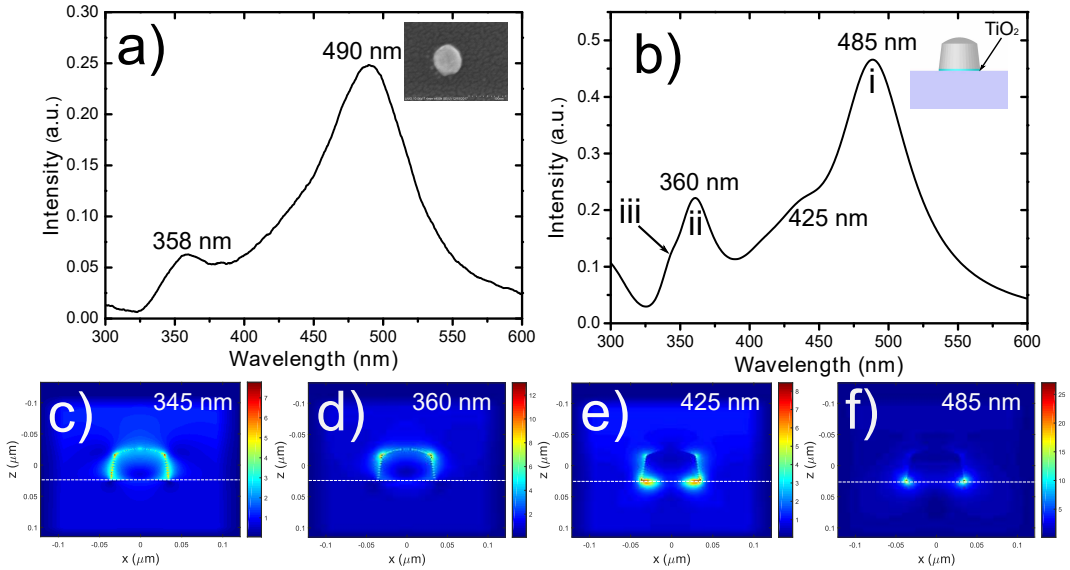

FIGURE 7.15: (a) Spectre de transmittance experimental d'un SNC, le diameter est de 70 nm et la hauteur 50 nm, (b) Simulations numériques correspondantes. (c) Cartes de champ électrique: profil de coupe XZ au centre du nanocylindre. L'illumination est seulement l'axe z et polarisée selon l'axe x. La ligne pointillée noire montre la surface du substrat pour une excitation à 345 nm (Mode iii), (d) 360 nm (Mode ii), (d) 425 nm (mode magnétique), (f) 485 nm (mode i).

Influence de la zone de contact entre le cylindre et le substrat : comparaison cylindre/sphère

Les propriétés optiques de nanosphères colloïdales d'or sont utilisées pour les spectroscopies d'exaltation en raison de leurs caractéristiques plasmoniques et de leur processus de fabrication abordable. Les modes des nanosphères dans un milieu homogène ont d'abord été discutés par Mie. Nous décidons de vérifier si le substrat a une influence sur ces modes. Les simulations numériques aident à comparer les LSPR des nanosphères placées dans l'air et sur un substrat. Les nanosphères d'or pour les expérimentations ont été préparées par le docteur Sylvie Marguet (Université Paris-Saclay) et ont été déposées sur des substrats d'ITO. Leur diamètre varie de 125 nm à 220 nm. La figure 7.16 présente les spectres calculés d'extinction et de diffusion des nanosphères d'or (GNS) dans l'air et sur un substrat d'ITO. Nous admettons que le GNS déposé sur le substrat possède un unique point de contact. L'indice de réfraction local impacte la position de la LSPR mais en comparant les spectres d'extinction sur les figures 7.16a et 7.16b, nous pouvons remarquer un déplacement mineur du mode principal en présence du substrat d'ITO. Puisque le GNS n'a qu'un seul point de contact, nous ne voyons pas de déplacement vers le rouge évident du mode dipolaire. Le principal changement vient de l'épaulement du pic vers 540 nm sur la figure 7.16b, qui pourrait annoncer un nouveau mode.

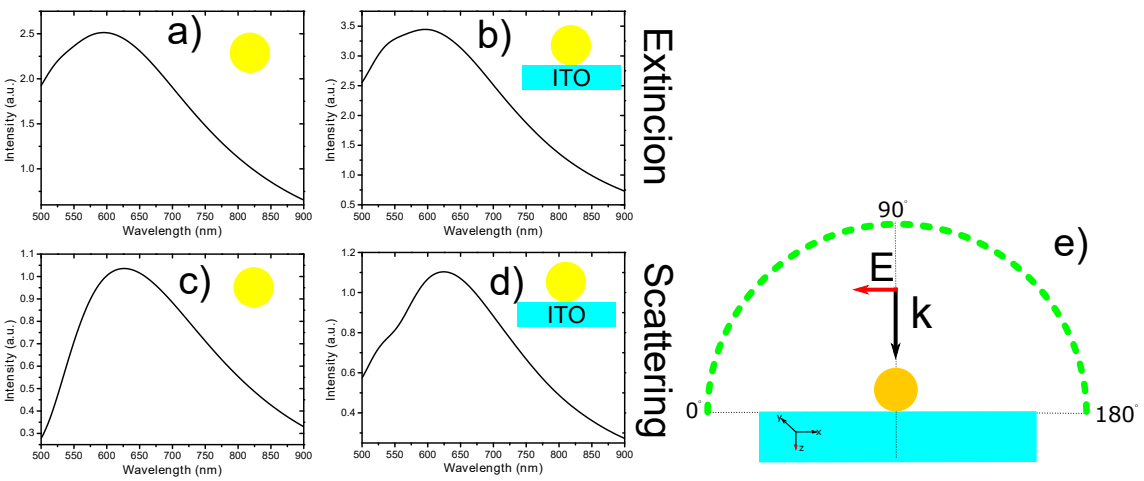

FIGURE 7.16: a) Spectre d'extinction simulé d'un GNS de diamètre 199 nm placé dans l'air. b) Spectre d'extinction simulé d'un GNS de diamètre 199 nm placé sur un substrat d'ITO. (c) Spectre de diffusion simulé (géométrie en réflexion) d'un GNS de diamètre de 199 nm placé dans l'air. (d) Spectre de diffusion simulé (géométrie en réflexion) d'un GNS de diamètre de 199 nm placé sur un substrat d'ITO. (e) Schéma d'illumination et de la collection (ligne pointillée verte)

Les figures 7.16c et 7.16d montre des spectres de diffusion calculés des GNS respectivement dans l'air et sur un substrat d'ITO. Le calcul des spectres de diffusion pour une nanosphère unique placée dans l'air montre un unique pic étroit (Figure 7.16c). Lorsque le substrat est présent, un épaulement apparaît à 540 nm. Le substrat casse la symétrie du système et peut causer un couplage entre les modes dipolaire et quadripolaire s'ils se chevauchent spectralement. En raison de l'hybridation, les modes plasmoniques changent leur position spectrale.

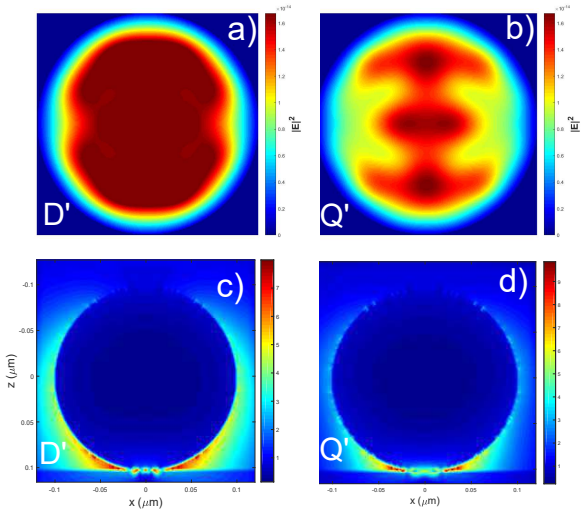

FIGURE 7.17: ((a) Carte calculée en champ lointain pour une excitation à 625 nm pour un GNS de diamètre 199 nm et pour (b) une excitation à 545 nm. (c) Carte de champ électrique calculée en champ proche pour une excitation à 625nm et (d) pour une excitation à 545 nm.

Pour comprendre la nature des modes hybrides (D' et Q'), nous réalisons des cartes en champ lointain dans l'espace de Fourier (espace k) pour une géométrie de réflexion. Les figures 7.17a et sphere-far-field1b montrent les images de l'espace des vecteurs d'onde k respectivement pour les modes D' et Q'. Le mode D' montre un caractère dipolaire, car le rayonnement est similaire au diagramme de rayonnement dipolaire lorsqu'il a la forme d'un donut. Le mode Q' a un caractère quadripolaire, car il possède deux lobes sur les côtés du diagramme de rayonnement.

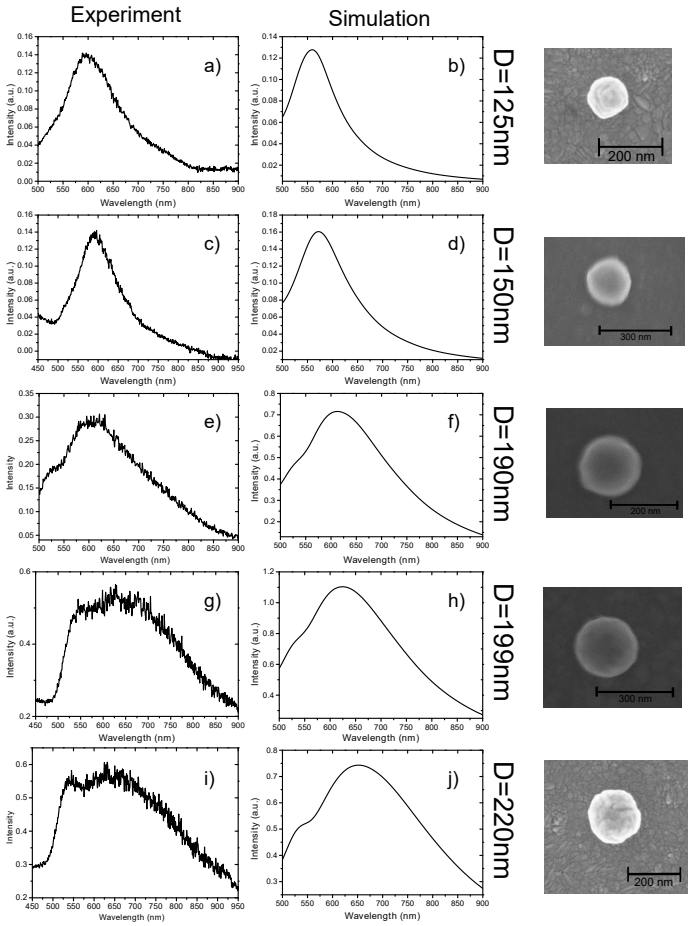

FIGURE 7.18: (a-j) Experiments and simulations of a single GNS with different diameter (D).

La figure 7.18 présente les spectres expérimentaux de diffusion pour différentes tailles de GNS. Nous pouvons observer que certains des spectres expérimentaux coïncident avec les spectres simulés (comme pour les spectres de diamètre 190 nm et 150 nm). Nous admettons que dans les autres cas, l'aire de contact entre le substrat et le GNS n'est pas un point.

Chapitre 6 : Fluorescence exaltée par résonance double

La fluorescence est un processus d'émission de lumière qui a lieu lorsqu'un objet fluorescent absorbe un photon d'une lumière incidente et réémet ce photon avec un spin de même nature. C'est un cas particulier de la luminescence. Depuis sa découverte, la fluorescence est utilisée principalement dans des dispositifs de détection et d'émission de lumière. Une structure plasmonique peut exalter l'émission d'une substance fluorescente [20, 47, 48, 100–103]. Le facteur d'exaltation de boîtes quantiques (QD pour « Quantum Dots » en anglais) est habituellement défini comme la multiplication de l'efficacité de collection, de l'exaltation de l'excitation et l'exaltation de l'émission [105, 106]. Nous fabriquons un réseau de GNC sur un substrat de verre. Le diamètre des GNC est de 170 nm et la hauteur de 50 nm. La distance entre les particules est de 1 μm. Une couche de silice de 5 nm vient recouvrir les GNC. Une monocouche homogène de QD (λ_{em}=610 nm) est obtenue après un processus de silanisation de la couche de silice permettant aux QDs d'être liés à cette couche de façon covalente. Les mesures de photoluminescence ont été réalisées à l'Université de Tübingen dans le groupe du professeur Monika Fleischer et dans le groupe du docteur Dai Zhang.

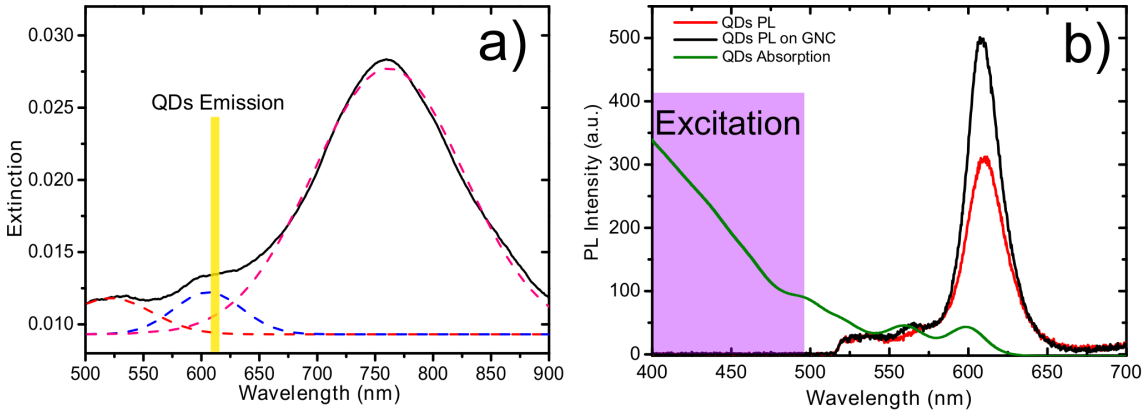

FIGURE 7.19: (a) Spectre d'extinction d'un réseau de GNC de 170 nm de diamètre, illuminé à un angle de 50°. Les différents pics sont révélés par les courbes pointillées. L'émission des QD coïncide avec le mode quadripolaire. (b) Fluorescence à un photon d'une monocouche de QDs couplé à un GNC unique de diamètre 170 nm. Le spectre d'absorption des QDs est superposé (courbe verte).

Premièrement, nous étudions l'émission de photoluminescence (PL) à un photon de la monocouche et l'exaltation près des nanoparticules plasmoniques. La figure 7.19a montre que l'émission des QDs coïncide avec le mode quadripolaire supporté par le GNC. De plus, l'illumination UV (inférieure à 500 nm) excite les QDs mais n'excite pas de résonance plasmonique au sein de la nanoparticule d'or. Nous pouvons ainsi statuer que l'interaction plasmon-QD est seulement liée à l'émission des QDs, via le mode plasmonique quadripolaire.

La figure 7.19b montre la PL relative des QDs non couplées et couplées à un GNC unique de diamètre 170 nm. Nous obtenons un facteur d'exaltation de 1,6 qui peut s'expliquer par le couplage de l'émission des QDs au mode quadripolaire du GNC. Un mode quadripolaire étant normalement non-radiatif, il y a alors deux possibilités : (1) le mode quadripolaire en question est un mode hybride radiatif dû à la brisure de symétrie entrainée par le substrat, (2) le champ proche du mode quadripolaire exalte l'absorption des QD au premier pic excitonique (visible autour de 600 nm sur la courbe verte de la figure 7.19b).

Photoluminescence à deux photons

Dans cette partie, nous espérons exciter les QDs grâce à la photoluminescence à deux photons (TPPL). En effet, l'excitation laser est effectuée à 774 nm, c'est-à-dire en dehors du spectre d'absorption des QDs. L'excitation directe à un photon est donc prescrite. L'excitation à deux photons est réalisée grâce à un laser intense. De plus, la longueur d'onde d'excitation coïncide ici avec la résonance plasmonique dipolaire dans le plan du cylindre (Fig. 6.5a). Pour comparer les facteurs d'exaltation de la TPPL et de la PL, nous prenons le spectre de chaque GNC pour différentes positions du focus laser par rapport au GNC. La polarisation incidente est ici azimuthale, comme montré par le schéma du spot laser en haut de la figure 6.5b. Les spectres sont présentés sur la figure 6.5(c-f). Les lignes solides montrent les spectres de la TPPL directement au-dessus des GNCs. Quand le point focal du laser est déplacée du centre vers le bord du GNC (lignes pointillées), le signal de TPPL est diminué car le faisceau est en partie en dehors du GNC.

Nous obtenons ici un facteur d'exaltation variant de 7,5 à 25. Nous attribuons cette augmentation à une double exaltation plasmonique : à l'excitation et à l'émission.

La figure 7.21a illustre les cartes de TPPL des GNCs (P1-P4) excités par un faisceau laser polarisé radialement. Les spots ont une forme de donut sur les zones où il y a des GNCs. Nous enregistrons les spectres de TPPL pour différentes positions du focus allant du centre du donut vers le bord où le signal est le plus fort (Figure 7.21a-7.21e).

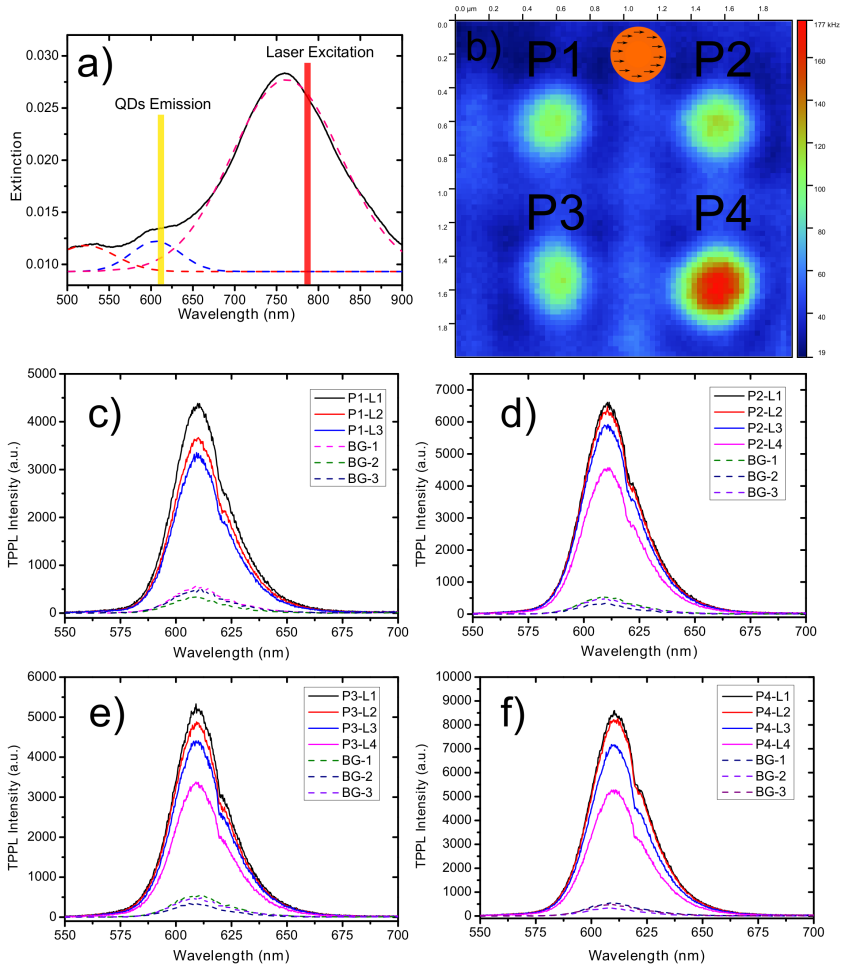

FIGURE 7.20: (a) Carte scannée de TPPL d'un réseau de 170 nm de diamètre. La polarisation est linéaire. (b-e) Spectres TPPL pour chaque GNC (P1-P4), les courbes solides présentent les spectres TPPL quand la mise au point du laser se déplace du centre au côté des GNCs. Les courbes pointillées montrent les spectres TPPL en dehors de la zone

Quand le GNC est placé au centre du faisceau, il interagit seulement avec la composante verticale du champ électrique. Ainsi, le GNC placé au centre du focus ne présente donc pas de mode plasmonique dipolaire dans le plan. De plus, la longueur d'onde 774 nm n'est pas résonante avec le mode dipolaire vertical, ce qui laisse penser que la TPPL n'est pas exaltée par le couplage entre l'excitation des QDs et un mode plasmonique du GNC. Dans ce cas, le facteur d'exaltation mesuré au centre du GNC est d'environ 1.7, ce qui correspond approximativement au facteur d'exaltation mesuré dans le cas des mesures de PL à 1 photon (1.6). Nous avons donc montré une augmentation du facteur d'exaltation d'un facteur 5 environ (de 1.6 à 7.5) lorsqu'on utilise un système plasmonique doublement résonant, à l'excitation et à l'émission des QDs.

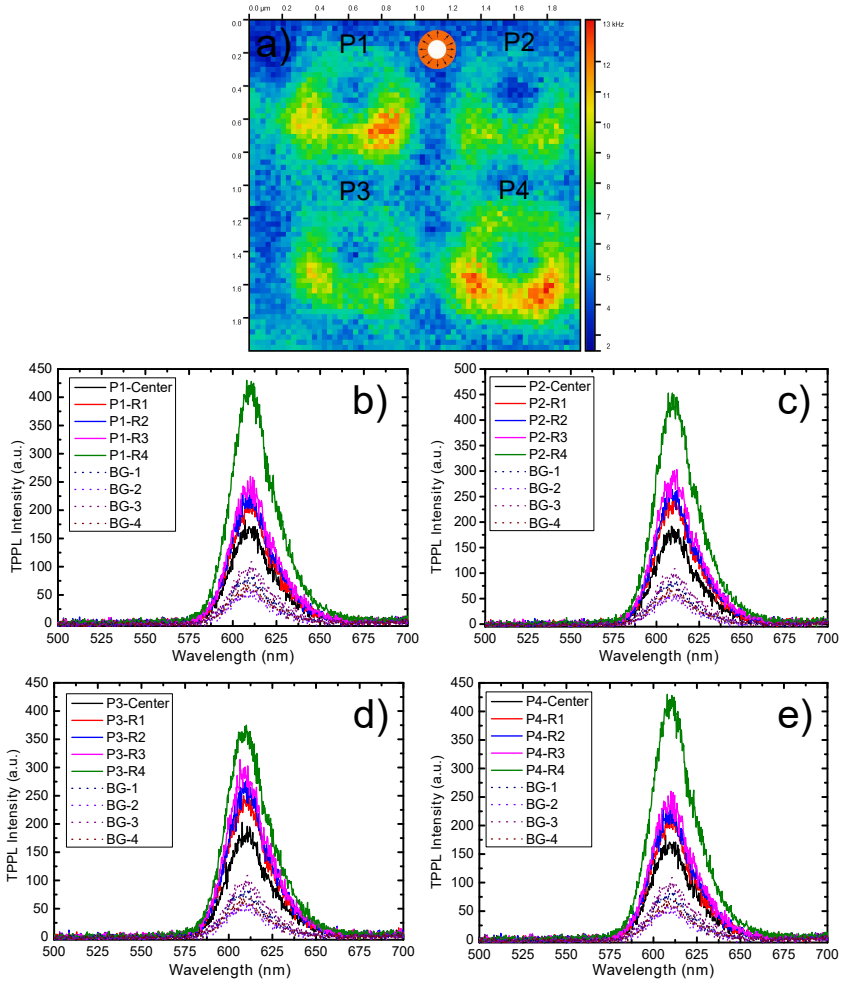

FIGURE 7.21: (a)TPPL scanned map of the array of 170 nm-diameter array. The polarization is radial. (b-e) TPPL spectra for each GNC (P1-P4), the solid curves present the TPPL spectra when the laser focuses from the center to the edge of the GNCs. The dotted line curves shows TPPL spectra out of the array.

Conclusion

Le but principal de cette thèse était d'expliquer les facteurs majeurs qui pouvaient influencer la réponse optique des nanoparticules plasmoniques. La thèse étudie et expérimente pratiquement toutes les raisons possibles affectant les spectres expérimentaux et numériques. Nous avons discuté et expliqué les impacts des méthodes expérimentales sur les spectres et mis en lumière l'importance des composantes du montage expérimental. De plus, nous avons proposé deux nouvelles approches pour caractériser des nano-objets uniques. Nous avons également étudié les changements intrinsèques du système plasmonique, comme la géométrie, la forme, l'indice de réfraction et la présence d'un substrat. Par exemple, le substrat peut causer une hybridation des

modes et changer leur position spectrale et la disposition spatiale de leur champ électrique. Ainsi, nous avons étudié l'hybridation causée par la brisure de symétrie de la forme de la nanostructure. L'étude et la compréhension des propriétés optiques des nanocylindres d'or nous a permis d'élaborer un système doublement résonant pour l'exaltation de fluorescence, comme étape finale.

Bibliography

[1] J. Hinken. *Superconductor Electronics: Fundamentals and Microwave Applications*. 2012.

[2] Simon M. Sze and Kwok K. Ng. *Physics of Semiconductor Devices*. 2006.

[3] R. G.H. Van Uden, R. Amezcua Correa, E. Antonio Lopez, F. M. Huijskens, C. Xia, G. Li, A. Schülzgen, H. De Waardt, A. M.J. Koonen, and C. M. Okonkwo. Ultra-high-density spatial division multiplexing with a few-mode multicore fibre. *Nature Photonics*, 8(11):865–870, 2014.

[4] Daniel Minoli. *Nanotechnology Applications to Telecommunications and Networking*. 2005.

[5] Bahaa E A Saleh and Malvin Carl Teich. Fundamentals of Photonics , 2nd Edition, 2007.

[6] David a. B. Miller. The Fundamental Limit to Optical Components. *Optics and Photonics News*, 18(12):27, 2007.

[7] Jian Wang. A review of recent progress in plasmon-assisted nanophotonic devices, 2014.

[8] Alexei A. Maradudin. Introduction: Plasmonics and its building blocks. *Handbook of Surface Science*, 4:1–36, 2014.

[9] S. A. Maier, M. L. Brongersma, P. G. Kik, S. Meltzer, A. A G Requicha, and H. A. Atwater. Plasmonics-a route to nanoscale optical devices. *Advanced Materials*, 13(19):1501–1505, 2001.

[10] Tao Xie, Chao Jing, and Yi-Tao Long. Single plasmonic nanoparticles as ultrasensitive sensors. *The Analyst*, 142(3):409–420, 2017.

[11] Ming Li, Scott K. Cushing, and Nianqiang Wu. Plasmon-enhanced optical sensors: a review. *The Analyst*, 140(2):386–406, 2015.

[12] Adam B. Taylor and Peter Zijlstra. Single-Molecule Plasmon Sensing: Current Status and Future Prospects, 2017.

[13] Christophe Caucheteur, Tuan Guo, Fu Liu, Bai Ou Guan, and Jacques Albert. Ultrasensitive plasmonic sensing in air using optical fibre spectral combs. *Nature Communications*, 7, 2016.

[14] Scott K. Cushing and Nianqiang Wu. Progress and Perspectives of Plasmon-Enhanced Solar Energy Conversion. *The Journal of Physical Chemistry Letters*, 7(4):666–675, 2016.

[15] Xiuzhen Zheng and Liwu Zhang. Photonic nanostructures for solar energy conversion. *Energy Environ. Sci.*, 9(8):2511–2532, 2016.

[16] Jeremy G. Smith, Jacob A. Faucheaux, and Prashant K. Jain. Plasmon resonances for solar energy harvesting: A mechanistic outlook, 2015.

[17] Igor Zorić, Michael Zäch, Bengt Kasemo, and Christoph Langhammer. Gold, platinum, and aluminum nanodisk plasmons: Material independence, subradiance, and damping mechanisms. *ACS Nano*, 5(4):2535–2546, 2011.

[18] Ranveig Flatabø, Vårin R. A. Holm, Håkon Eidsvåg, Bodil Holst, and Martin M. Greve. Light absorption and scattering of 40–170 nm gold nanoparticles on glass substrates. *Journal of Vacuum Science & Technology B, Nanotechnology and Microelectronics: Materials, Processing, Measurement, and Phenomena*, 35(6):06G403, 2017.

[19] Stefan A. Maier. *Plasmonics: Fundamentals and applications*. Springer, New York, 2007.

[20] Lukas Novotny and Bert Hecht. *Principles of nano-optics*. Cambridge University Press, Cambridge, 2009.

[21] S. Raimes. The theory of plasma oscillations in metals. *Reports on Progress in Physics*, 20(1):1–37, 1957.

[22] David Pines and David Bohm. A collective description of electron interactions: II. Collective vs individual particle aspects of the interactions. *Physical Review*, 85(2):338–353, 1952.

[23] R.W. Wood. XLII. On a remarkable case of uneven distribution of light in a diffraction grating spectrum. *Philosophical Magazine Series 6*, 4(21):396–402, 1902.

[24] R H Ritchie. Plasma Losses by Fast Electrons in Thin Metal Films. *Physical Review*, 106(5):874–881, 1957.

[25] C. J. Powell and J. B. Swan. Origin of the characteristic electron energy losses in magnesium. *Physical Review*, 116(1):81–83, 1959.

[26] C. J. Powell. The origin of the characteristic electron energy losses in aluminium and magnesium. *Journal of Nuclear Energy. Part C, Plasma Physics, Accelerators, Thermonuclear Research*, 2(1):57–64, 1961.

[27] Anatoly V. Zayats, Igor I. Smolyaninov, and Alexei A. Maradudin. Nano-optics of surface plasmon polaritons. *Phys. Rep.*, 408(3-4):131–314, 2005.

[28] Mario Bertolotti. *Masers and lasers: an historical approach*. Crc Press, 2015.

[29] Mario Bertolotti, Concita Sibilia, and Angela M Guzman. *Evanescent Waves in Optics: An Introduction to Plasmonics*, volume 206. Springer, 2017.

[30] Mingxia Song, Jean Dellinger, Olivier Demichel, Mickaël Buret, Gérard Colas Des Francs, Douguo Zhang, Erik Dujardin, and Alexandre Bouhelier. Selective excitation of surface plasmon modes propagating in Ag nanowires. *Optics Express*, 25(8):9138, 2017.

[31] Palash Bharadwaj, Alexandre Bouhelier, and Lukas Novotny. Electrical excitation of surface plasmons. *Physical Review Letters*, 106(22):1–4, 2011.

[32] P. B. Johnson and R. W. Christy. Optical constants of the noble metals. *Physical Review B*, 6(12):4370–4379, 1972.

[33] C F Bohren and D R Huffman. *Absorption and scattering of light by small particles*, volume 1. 1983.

[34] Johan Grand, Pierre Michel Adam, Anne Sophie Grimault, Alexandre Vial, Marc Lamy De La Chapelle, Jean Louis Bijeon, Sergei Kostcheev, and Pascal Royer. Optical extinction spectroscopy of oblate, prolate and ellipsoid shaped gold nanoparticles: Experiments and theory. *Plasmonics*, 1(2-4):135–140, 2006.

[35] Taixing Tan, Chungui Tian, Zhiyu Ren, Jun Yang, Yajie Chen, Li Sun, Zhongtao Li, Aiping Wu, Jie Yin, and Honggang Fu. LSPR-dependent SERS performance of silver nanoplates with highly stable and broad tunable LSPRs prepared through an improved seed-mediated strategy. *Physical Chemistry Chemical Physics*, 15(48):21034, 2013.

[36] J. J. Mock, M. Barbic, D. R. Smith, D. A. Schultz, and S. Schultz. Shape effects in plasmon resonance of individual colloidal silver nanoparticles. *Journal of Chemical Physics*, 116(15):6755–6759, 2002.

[37] Ian Freestone, Nigel Meeks, Margaret Sax, and Catherine Higgitt. The Lycurgus Cup - A Roman nanotechnology. *Gold Bulletin*, 40(4):270–277, 2008.

[38] Yinghong Gu, Lei Zhang, Joel K. W. Yang, Swee Ping Yeo, and Cheng-Wei Qiu. Color generation via subwavelength plasmonic nanostructures. *Nanoscale*, 7(15):6409–6419, 2015.

[39] Matthew A. Cooper. Optical biosensors in drug discovery. *Nature Reviews Drug Discovery*, 1(7):515–528, 2002.

[40] Andreas Horrer, Katrin Krieg, Kathrin Freudenberger, Sabrina Rau, Lothar Leidner, Günter Gauglitz, Dieter P. Kern, and Monika Fleischer. Plasmonic vertical dimer arrays as elements for biosensing. *Anal. Bioanal. Chem.*, 407(27):8225–8231, 2015.

[41] Kathryn M. Mayer, Jason H. Hafner, and Antibody À Antigen. Localized surface plasmon resonance sensors. *Chemical Reviews*, 111(6):3828–3857, 2011.

[42] Suzanna Akil-Jradi, Safi Jradi, Jérôme Plain, Pierre-Michel Adam, Jean-Louis Bijeon, Pascal Royer, and Renaud Bachelot. Micro/nanoporous polymer chips as templates for highly sensitive SERS sensors. *RSC Adv.*, 2(20):7837, 2012.

[43] Bruno Pettinger, Bin Ren, Gennaro Picardi, Rolf Schuster, and Gerhard Ertl. Nanoscale probing of adsorbed species by tip-enhanced Raman spectroscopy. *Phys. Rev. Lett.*, 92(9):8–11, 2004.

[44] Mark S. Anderson. Locally enhanced Raman spectroscopy with an atomic force microscope. *Applied Physics Letters*, 76(21):3130–3132, 2000.

[45] Norihiko Hayazawa, Hiroyuki Watanabe, Yuika Saito, and Satoshi Kawata. Towards atomic site-selective sensitivity in tip-enhanced Raman spectroscopy. *Journal of Chemical Physics*, 125(24), 2006.

[46] Bin Ren, Gennaro Picardi, and Bruno Pettinger. Preparation of gold tips suitable for tip-enhanced Raman spectroscopy and light emission by electrochemical etching. *Review of Scientific Instruments*, 75(4):837–841, 2004.

[47] Olga Kulakovich, Natalya Strekal, Alexandr Yaroshevich, Sergey Maskevich, Sergey Gaponenko, Igor Nabiev, Ulrike Woggon, and Mikhail Artemyev. Enhanced Luminescence of CdSe Quantum Dots on Gold Colloids, 2002.

[48] Dmitry V Guzatov, Svetlana V Vaschenko, Vyacheslav V Stankevich, Anatoly Ya Lunevich, Yuri F Glukhov, and Sergey V Gaponenko. Plasmonic Enhancement of Molecular Fluorescence near Silver Nanoparticles : Theory , Modeling , and Experiment. *Journal of Physical Chemistry C*, 116(19):10723–10733, 2012.

[49] Mark H Harpster, Hao Zhang, Ajaya K Sankara-warrier, Bryan H Ray, Timothy R Ward, J Pablo Kollmar, Keith T Carron, James O Mecham, Robert C Corcoran, William C Wilson, and Patrick A Johnson. SERS detection of indirect viral DNA capture using colloidal gold and methylene blue as a Raman label. *Biosensors and Bioelectronics*, 25(4):674–681, 2009.

[50] R Griffith Freeman, Katherine C Grabar, Keith J Allison, Robin M Bright, Jennifer A Davis, Andrea P Guthrie, Michael B Hommer, Michael A Jackson, Patrick C Smith, Daniel G Walter, and Michael J Natan. Self-Assembled Metal Colloid Monolayers: An Approach to SERS Substrates. *Science*, 267(5204):1629–1632., 1995.

[51] K A M R A N Badizadegan, Noriko Yoshizawa, Charles Boone, and M Ichael S Feld. Surface-Enhanced Raman Spectroscopy in Single Living Cells Using Gold Nanoparticles. *Applied Spectroscopy*, 56(2):150–154, 2002.

[52] Katrin Kneipp, Yang Wang, Harald Kneipp, Lev T Perelman, Irving Itzkan, Ramachandra R Dasari, and Michael S Feld. Single Molecule Detection Using Surface-Enhanced Raman Scattering (SERS). *Physical review letters*, 78(9):1667–1670, 1997.

[53] N Guillot, H Shen, B Frémaux, O Péron, E Rinnert, and T Toury. Surface enhanced Raman scattering optimization of gold nanocylinder arrays : Influence of the localized surface plasmon resonance and excitation wavelength. *Applied Physics Letters*, 97(2):023113, 2010.

[54] Simon P Hastings, Pattanawit Swanglap, Zhaoxia Qian, Ying Fang, So-Jung Park, Stephan Link, Nader Engheta, and Zahra Fakhraai. Quadrupole-Enhanced Raman Scattering. *ACS Nano*, 8(9):9025–9034, 2014.

[55] Andrey B. Evlyukhin, Carsten Reinhardt, Urs Zywietz, and Boris N. Chichkov. Collective resonances in metal nanoparticle arrays with dipole-quadrupole interactions. *Phys. Rev. B*, 85(24), 2012.

[56] Feng Hao, Elin M. Larsson, Tamer A. Ali, Duncan S. Sutherland, and Peter Nordlander. Shedding light on dark plasmons in gold nanorings. *Chem. Phys. Lett.*, 458(4-6):262–266, 2008.

[57] Markus K. Krug, Michael Reisecker, Andreas Hohenau, Harald Ditlbacher, Andreas Trügler, Ulrich Hohenester, and Joachim R. Krenn. Probing plasmonic breathing modes optically. *Appl. Phys. Lett.*, 105(17):10–13, 2014.

[58] Yu Huang, Emilie Ringe, Mengjing Hou, Lingwei Ma, and Zhengjun Zhang. Near-field mapping of three-dimensional surface charge poles for hybridized plasmon modes. *AIP Advances*, 5(10), 2015.

[59] Christopher P. Burrows and William L. Barnes. Large spectral extinction due to overlap of dipolar and quadrupolar plasmonic modes of metallic nanoparticles in arrays. *Optics Express*, 18(3):3187–3198, 2010.

[60] Michael B. Ross and George C. Schatz. Radiative effects in plasmonic aluminum and silver nanospheres and nanorods. *Journal of Physics D: Applied Physics*, 48(18):184004, 2015.

[61] Ankun Yang, Alexander J. Hryn, Marc R. Bourgeois, Won-Kyu Lee, Jingtian Hu, George C. Schatz, and Teri W. Odom. Programmable and reversible plasmon mode engineering. *Proceedings of the National Academy of Sciences*, 113(50):14201–14206, 2016.

[62] Kane S. Yee. Numerical Solution of Initial Boundary Value Problems Involving Maxwell's Equations in Isotropic Media. *IEEE Transactions on Antennas and Propagation*, 14(3):302–307, 1966.

[63] Allen Taflove and Susan C. Hagness. *Computational Electrodynamics: The Finite-Difference Time-Domain Method, Third Edition*. 2005.

[64] R. Jin, Y. Cao, C. A. Mirkin, K. L. Kelly, G. C. Schatz, and J. G. Zheng. Photoinduced conversion of silver nanospheres to nanoprisms. *Science*, 294(5548):1901–1903, 2001.

[65] Wei Zhou and Teri W. Odom. Tunable subradiant lattice plasmons by out-of-plane dipolar interactions. *Nature Nanotechnology*, 6(7):423–427, 2011.

[66] a Brioude and M P Pileni. Silver nanodisks: optical properties study using the discrete dipole approximation method. *The journal of physical chemistry. B*, 109(49):23371–23377, 2005.

[67] E. Stefan Kooij and Bene Poelsema. Shape and size effects in the optical properties of metallic nanorods. *Phys. Chem. Chem. Phys.*, 8(28):3349–3357, 2006.

[68] S. Link and M. A. El-Sayed. Simulation of the Optical Absorption Spectra of Gold Nanorods as a Function of Their Aspect Ratio and the Effect of the Medium Dielectric Constant. *The Journal of Physical Chemistry B*, 109(20):10531–10532, 2005.

[69] S. F. Yu, Y. Liu, E. S. M. Goh, Z. H. Cen, S. Zhu, T. P. Chen, and Y. C. Liu. Split of surface plasmon resonance of gold nanoparticles on silicon substrate: a study of dielectric functions. *Optics Express*, 18(21):21926, 2010.

[70] Toon Coenen, Felipe Bernal Arango, A. Femius Koenderink, and Albert Polman. Directional emission from a single plasmonic scatterer. *Nature Communications*, 5, 2014.

[71] Emilie Ringe, Mark R. Langille, Kwonnam Sohn, Jian Zhang, Jiaxing Huang, Chad A. Mirkin, Richard P. Van Duyne, and Laurence D. Marks. Plasmon length: A universal parameter to describe size effects in gold nanoparticles. *Journal of Physical Chemistry Letters*, 3(11):1479–1483, 2012.

[72] Richard Zsigmondy. *Colloids and the ultramicroscope: a manual of colloid chemistry and ultramicroscopy*. J. wiley and sons edition, 1909.

[73] Min Hu, Carolina Novo, Alison Funston, Haining Wang, Hristina Staleva, Shengli Zou, Paul Mulvaney, Younan Xia, and Gregory V. Hartland. Dark-field microscopy studies of single metal nanoparticles: understanding the factors that influence the linewidth of the localized surface plasmon resonance. *Journal of Material Chemistry*, 18(17):1949–1960, 2008.

[74] C. Sönnichsen, S. Geier, N. E. Hecker, G. von Plessen, J. Feldmann, H. Ditlbacher, B. Lamprecht, J. R. Krenn, F. R. Aussenegg, V. Z-H. Chan, J. P. Spatz, and M. Möller. Spectroscopy of single metallic nanoparticles using total internal reflection microscopy. *Applied Physics Letters*, 77(19):2949, 2000.

[75] J. J. Mock, M. Barbic, D. R. Smith, D. A. Schultz, and S. Schultz. Shape effects in plasmon resonance of individual colloidal silver nanoparticles. *J. Chem. Phys.*, 116(15):6755–6759, 2002.

[76] Yuan Hsing Fu, Arseniy I. Kuznetsov, Andrey E. Miroshnichenko, Ye Feng Yu, and Boris Luk'yanchuk. Directional visible light scattering by silicon nanoparticles. *Nature Communications*, 4:1–6, 2013.

[77] Dang Yuan Lei, Antonio I. Fernández-Domínguez, Yannick Sonnefraud, Kannatassen Appavoo, Richard F. Haglund, John B. Pendry, and Stefan A. Maier. Revealing plasmonic Gap modes in particle-on-film systems using dark-field spectroscopy. *ACS Nano*, 6(2):1380–1386, 2012.

[78] S Schultz, D R Smith, J J Mock, and D a Schultz. Single-target molecule detection with nonbleaching multicolor optical immunolabels. *Proceedings of the National Academy of Sciences of the United States of America*, 97(3):996–1001, 2000.

[79] Jonathan A. Fan, Kui Bao, J. Britt Lassiter, Jiming Bao, Naomi J. Halas, Peter Nordlander, and Federico Capasso. Near-normal incidence dark-field microscopy: Applications to nanoplasmonic spectroscopy. *Nano Lett.*, 12(6):2817–2821, 2012.

[80] M W Knight, J Fan, F Capasso, and N J Halas. Influence of excitation and collection geometry on the dark field spectra of individual plasmonic nanostructures. *Opt. Express*, 18(3):2579–2587, 2010.

[81] Victor R. Weidner and Jack J. Hsia. Reflection properties of pressed polytetrafluoroethylene powder. *Journal of the Optical Society of America*, 71(7):856, 1981.

[82] Nabil Mahi, Gaëtan Lévêque, Ophélie Saison, Joseph Marae-Djouda, Roberto Caputo, Arthur Gontier, Thomas Maurer, Pierre Michel Adam, Benemar Bouhafs, and Abdellatif Akjouj. In Depth Investigation of Lattice Plasmon Modes in Substrate-Supported Gratings of Metal Monomers and Dimers. *J. Chem. Phys. C*, 121(4):2388–2401, 2017.

[83] Dmitry Khlopin, Frédéric Laux, William P. Wardley, Jérôme Martin, Gregory A. Wurtz, Jérôme Plain, Nicolas Bonod, Anatoly V. Zayats, Wayne Dickson, and Davy Gérard. Lattice modes and plasmonic linewidth engineering in gold and aluminum nanoparticle arrays. *Journal of the Optical Society of America B*, 34(3):691, 2017.

[84] Joseph Marae-Djouda, Roberto Caputo, Nabil Mahi, Gaëtan Lévêque, Abdellatif Akjouj, Pierre Michel Adam, and Thomas Maurer. Angular plasmon response of gold nanoparticles arrays: Approaching the Rayleigh limit. *Nanophotonics*, 6(1):279–288, 2017.

[85] Hailong Hu, Huigao Duan, Joel K W Yang, and Ze Xiang Shen. Plasmon-modulated photoluminescence of individual gold nanostructures. *ACS Nano*, 6(11):10147–10155, 2012.

[86] Yiqin Chen, Zhiqin Li, Quan Xiang, Yasi Wang, Zhiqiang Zhang, and Huigao Duan. Reliable fabrication of plasmonic nanostructures without an adhesion layer using dry lift-off. *Nanotechnology*, 26(40), 2015.

[87] Peter Zijlstra, James W. M. Chon, and Min Gu. White light scattering spectroscopy and electron microscopy of laser induced melting in single gold nanorods. *Phys. Chem. Chem. Phys.*, 11(28):5915, 2009.

[88] Hsiang An Chen, Cheng Lun Hsin, Yu Ting Huang, Ming Lee Tang, Scott Dhuey, Stefano Cabrini, Wen Wei Wu, and Stephen R. Leone. Measurement of interlayer screening length of layered graphene by plasmonic nanostructure resonances. *J. Chem. Phys. C*, 117(43):22211–22217, 2013.

[89] Kai Qiang Lin, Jun Yi, Shu Hu, Bi Ju Liu, Jun Yang Liu, Xiang Wang, and Bin Ren. Size Effect on SERS of Gold Nanorods Demonstrated via Single Nanoparticle Spectroscopy. *J. Chem. Phys. C*, 120(37):20806–20813, 2016.

[90] Shunping Zhang, Kui Bao, Naomi J. Halas, Hongxing Xu, and Peter Nordlander. Substrate-induced Fano resonances of a plasmonic nanocube: A route to increased-sensitivity localized surface plasmon resonance sensors revealed. *Nano Lett.*, 11(4):1657–1663, 2011.

[91] E. Prodan, C. Radloff, N. J. Halas, and P. Nordlander. A Hybridization Model for the Plasmon Response of Complex Nanostructures. *Science*, 302(5644):419–422, 2003.

[92] Leif J. Sherry, Shih Hui Chang, George C. Schatz, Richard P. Van Duyne, Benjamin J. Wiley, and Younan Xia. Localized surface plasmon resonance spectroscopy of single silver nanocubes. *Nano Lett.*, 5(10):2034–2038, 2005.

[93] P Spinelli, C van Lare, E Verhagen, and A Polman. Controlling Fano lineshapes in plasmon-mediated light coupling into a substrate. *Opt. Express*, 19(S3):A303–A311, 2011.

[94] Franz Philipp Schmidt, Harald Ditlbacher, Ulrich Hohenester, Andreas Hohenau, Ferdinand Hofer, and Joachim R. Krenn. Dark plasmonic breathing modes in silver nanodisks. *Nano Lett.*, 12(11):5780–5783, 2012.

[95] Ayan Chakrabarty, Feng Wang, Fred Minkowski, Kai Sun, and Qi-Huo Wei. Cavity modes and their excitations in elliptical plasmonic patch nanoantennas. *Optics express*, 20(11):11615–24, 2012.

[96] A. C. Nwanya, P. E. Ugwuoke, B. A. Ezekoye, R. U. Osuji, and F. I. Ezema. Structural and optical properties of chemical bath deposited silver oxide thin films: Role of deposition time. *Advances in Materials Science and Engineering*, 2013, 2013.

[97] Ullash Kumar Barik, S. Srinivasan, C. L. Nagendra, and A. Subrahmanyam. Electrical and optical properties of reactive DC magnetron sputtered silver oxide thin films: Role of oxygen. *Thin Solid Films*, 429(1-2):129–134, 2003.

[98] Artur Movsesyan, Anne-Laure Baudrion, and Pierre-Michel Adam. Extinction measurements of metallic nanoparticles arrays as a way to explore the single nanoparticle plasmon resonances. *Opt. Express*, 26(5):6439–6445, 2018.

[99] Peter TC So. Two-photon Fluorescence Light Microscopy. *eLS*, pages 1–5, 2001.

[100] Julie Goffard, Davy Gérard, Patrice Miska, Anne-Laure Baudrion, Régis Deturche, and Jérôme Plain. Plasmonic engineering of spontaneous emission from silicon nanocrystals. *Scientific Reports*, 3(1):2672, 2013.

[101] Pierre Viste, Jérome Plain, Rodolphe Jaffiol, Alexandre Vial, Pierre Michel Adam, and Pascal Royer. Enhancement and quenching regimes in metal-semiconductor hybrid optical nanosources. *ACS Nano*, 4(2):759–764, 2010.

[102] Martin Bauch, Koji Toma, Mana Toma, Qingwen Zhang, and Jakub Dostalek. Plasmon-Enhanced Fluorescence Biosensors: A Review. *Plasmonics*, 9(4):781–799, 2014.

[103] Guowei Lu, Tianyue Zhang, Wenqiang Li, Lei Hou, Jie Liu, and Qihuang Gong. Single-molecule spontaneous emission in the vicinity of an individual gold nanorod. *Journal of Physical Chemistry C*, 115(32):15822–15828, 2011.

[104] Jérôme Wenger, Davy Gérard, José Dintinger, Oussama Mahboub, Nicolas Bonod, Evgeny Popov, Thomas W. Ebbesen, and Hervé Rigneault. Emission and excitation contributions to enhanced single molecule fluorescence by gold nanometric apertures. *Optics Express*, 16(5):3008, 2008.

[105] Jérôme Wenger. Fluorescence Enhancement Factors on Optical Antennas : Enlarging the Experimental Values without Changing the Antenna Design. *International Journal of Optics*, 2012, 2012.

[106] Frédéric Laux, Nicolas Bonod, and Davy Gérard. Single Emitter Fluorescence Enhancement with Surface Lattice Resonances. *Journal of Physical Chemistry C*, 121(24):13280–13289, 2017.

[107] Si-yun Liu, Lu Huang, Jia-fang Li, Chen Wang, Qiang Li, Hong-xing Xu, Honglian Guo, Zi-ming Meng, Zhe Shi, and Zhi-yuan Li. Simultaneous Excitation and Emission Enhancement of Fluorescence Assisted by Double Plasmon Modes of Gold Nanorods. *Journal of Physical Chemistry C*, 117(20):10636–10642., 2013.

[108] Xin Liu and Dang Yuan Lei. Simultaneous excitation and emission enhancements in upconversion luminescence using plasmonic double-resonant gold nanorods. *Scientific Reports*, (October):1–13, 2015.

[109] L. Riachy, C. Vézy, and R. Jaffiol. Non-radiative excitation fluorescence microscopy. In *Proceedings of SPIE*, volume 9721, 2016.

[110] Kotni Santhosh, Ora Bitton, Lev Chuntonov, and Gilad Haran. Vacuum Rabi splitting in a plasmonic cavity at the single quantum emitter limit. *Nature Communications*, 7(May):1–5, 2016.

[111] C. Debus, M. A. Lieb, A. Drechsler, and A. J. Meixner. Probing highly confined optical fields in the focal region of a high NA parabolic mirror with subwavelength spatial resolution. *Journal of Microscopy*, 210(3):203–208, 2003.

[112] Philipp Reichenbach, Anke Horneber, Dominik A. Gollmer, Andreas Hille, Josip Mihaljevic, Christian Schäfer, Dieter P. Kern, Alfred J. Meixner, Dai Zhang, Monika Fleischer, and Lukas M. Eng. Nonlinear optical point light sources through field enhancement at metallic nanocones. *Optics Express*, 22(13):15484, 2014.

Artur MOVSESYAN

Doctorat : Matériaux, Mécanique, Optique, Nanotechnologie

Année 2018

Propriétés plasmoniques des nanoparticules métalliques : au-delà de la résonance dipolaire

Ces dernières années, l'intérêt pour les nanoparticules métalliques a grandement augmenté du fait de la spécificité de leurs propriétés optiques. Ces propriétés se réfèrent aux résonances de plasmon de surface localisées pour les nanoparticules métalliques dont la taille est plus petite que la longueur d'onde d'illumination. Ces résonances sont directement liées à l'oscillation des électrons de conduction du métal et mènent à un champ proche électromagnétique fort localisé à la surface de la nanoparticule. Les nanoparticules métalliques sont utilisées dans des applications variées, telles que la détection biochimique, les lasers, la génération de couleurs, la spectroscopie exaltée de surface, la thérapie photo thermique du cancer, etc. Le plus souvent, les applications sont basées sur des facteurs externes. Dans cette thèse, nous étudions en profondeur les facteurs qui peuvent affecter la position spectrale de ces modes. De plus, nous parlerons de l'influence du montage expérimental sur les spectres optiques enregistrés. Outre le mode dipolaire, une nanostructure plasmonique peut montrer plusieurs autres modes qui peuvent être potentiellement utilisés pour des applications. Nous étudierons l'excitation et les mécanismes révélant les modes plasmoniques « cachés ». Dans la dernière étape de cette étude, nous utiliserons les propriétés multi-résonantes d'un nanocylindre d'or pour démontrer l'exaltation de fluorescence de boîtes quantiques par un effet plasmonique résonant double. Cette approche possède un grand potentiel pour être utilisée dans des applications d'énergie solaire.

Mots clés : résonance plasmonique de surface – nanophotonique – spectroscopie à haute résolution – différences finies – photoluminescence.

Plasmonic Properties of Metallic Nanoparticles: Beyond the Dipolar Resonance

Last decades the interest in metallic nanoparticles increased enormously due to their optical tremendous properties. These properties refer to the localized surface plasmon resonances, which are characteristic for metallic nanoparticles of smaller sizes than the illumination wavelength. These resonances are directly linked to the oscillation of the conduction electrons of the metal and lead to a strong electromagnetic near-field localized at the nanoparticle surface. The plasmonic nanoparticles are successfully used in various application such as biochemical sensing, lasing, color generation, surface enhanced spectroscopies, photo-thermal therapy of cancer and etc.. Mostly, the applications are based on a single plasmonic resonance (mode) called dipolar. These modes are sensitive to many internal and external factors. In this thesis, we deeply study the factors, which may act on the spectral position of these modes. Moreover, we introduce the experimental set-ups influence on the recorded optical spectra. Besides the dipolar mode, a plasmonic nanostructure may exhibit many other modes which can be potentially used in applications. We investigate the excitation and the revealing mechanisms of so-called "hidden" plasmonic modes. In the final stage of the study we used the multi-resonant properties of a gold nanocylinder to demonstrate the enhancement of the quantum dots fluorescence by a doubly resonant plasmonic effect. This approach has a strong potential to be used in the solar energy applications.

Keywords: surface plasmon resonance – nanophotonics – high resolution spectroscopy – finite differences – photoluminescence.